Understanding Antarctic ice-stream flow using ice-flow models and geophysical observations

David A Lilien

A dissertation

submitted in partial fulfillment of the

requirements for the degree of

Doctor of Philosophy

University of Washington

2019

Reading Committee:

Ian Joughin, Chair

Knut Christianson

Benjamin Smith

Program Authorized to Offer Degree:

Department of Earth and Space Sciences

©Copyright 2019
David A Lilien

University of Washington

Abstract

Understanding Antarctic ice-stream flow using ice-flow models and geophysical observations

David A Lilien

Chair of the supervisory committee:

Dr. Ian R Joughin

Department of Earth and Space Sciences

Ice streams are the primary pathway by which Antarctic ice is evacuated to the ocean. Because the Antarctic ice sheets lose mass primarily through oceanic melt and calving, ice-stream dynamics exert a primary control on the mass balance of the ice sheets. Thus, changes in melt rates at the ice-sheet margins, or in accumulation in the ice-sheet interiors, affect ice-sheet mass balance on timescales modulated by the response time of the ice streams. Even abrupt changes in melt at the margins can cause ice-stream speedup and resultant thinning lasting millennia, so understanding the upstream propagation of marginally forced changes across timescales is key for understanding the ice sheets' ongoing contribution to sea-level rise. This dissertation is

comprised of three studies that use observations and models to understand changes to Antarctic ice-stream dynamics on timescales from decades to millennia.

The first chapter synthesizes remotely sensed observations of Smith, Pope, and Kohler glaciers in West Antarctica to investigate the causes and extent of their retreat. These glaciers have displayed some of the largest measured grounding-line retreat, most rapid thinning, and largest speedup amongst Antarctic ice streams. This retreat has drawn interest in their stability both in its own right and as a harbinger of future changes to larger neighboring ice streams. In this study, recent melt rates were determined using flux divergence estimates derived from observations of ice thickness and surface velocity. Out-of-balance melt at the beginning of the study period indicates that the imbalance of this system predates the beginning of satellite velocity observations in 1996. Throughout much of 1996-2010, there was both greater melt over the ice shelves than flux across the grounding line, implying loss of floating ice and elevated melt forcing, and greater grounding-line flux than accumulation, implying adjustment of the grounded ice in response to the ongoing imbalance. The grounding line position of Kohler glacier, and a large melt channel that is unlikely to be a steady-state feature, suggest that the perturbation to this system began on Kohler glacier sometime around the 1970s. Viscosity of the ice shelves, inferred using a numerical model, indicates that weakening of the Crosson ice shelf was necessary to allow the observed speedup, though it is unable to determine whether the weakening was a cause or effect of the ongoing retreat.

The second chapter uses a suite of numerical model simulations to determine the dominant drivers of the recent retreat of Smith, Pope, and Kohler glaciers, and extends those simulations that best match observations to evaluate likely future retreat. Similar to the findings of previous studies, the distribution of sub-shelf melt is found to be the primary control on the rate of

grounding-line retreat, while the shelf-averaged melt rate exerts a secondary control. The model simulations indicate that, despite ongoing imbalance, the grounding-line position in 1996 was not inherently unstable, but rather elevated melt at the grounding line was required to cause the observed retreat. A weakening of the ice-shelf margins was found to hasten the onset of grounding-line retreat and led to greater speedup. However, without increases in melt beyond 1996 levels, marginal weakening was insufficient to initiate grounding-line retreat. All simulations that capture the observed retreat continue to lose mass until at least 2100, suggesting that ice in this basin may contribute over 8 mm to global mean sea level by 2100. The magnitude of thinning deep in the catchment suggests that the retreat of Kohler and Smith glacier may hasten the destabilization of the neighboring Thwaites glacier catchment.

The third chapter uses the timescale of the recently drilled South Pole Ice Core (SPICEcore) and nearby geophysical observations to infer the history of ice flow near the South Pole during the last 10,000 years. The South Pole is located 180 km from the nearest ice divide and drains from the East Antarctic plateau through Academy glacier/Foundation ice stream. As a result, ice flow near the South Pole is potentially affected by the dynamics of these ice streams, and so the history of ice flow in this region has the potential to inform understanding of how marginally forced changes affect the ice-sheet interior. Because the South Pole is far from an ice divide, the accumulation record in SPICEcore incorporates both spatial variations in accumulation upstream and temporal variations in regional accumulation. Comparison between the SPICEcore accumulation record, derived by correcting measured layer thicknesses for thinning, with an accumulation record derived from new GPS and radar measurements upstream, yields insight into past ice flow and accumulation. When ice speeds are modeled as increasing by 15% since 10 ka, the upstream accumulation explains 77% of the variance in the SPICEcore-derived

accumulation (vs. 22% without speedup). This correlation is only expected if the ice-flow direction and spatial pattern of accumulation were stable throughout the Holocene. The 15% speedup in turn suggests a slight (3-4%) steepening or thickening of the ice-sheet interior and provides a new constraint on the evolution of the East Antarctic Ice Sheet following the glacial termination.

Table of Contents

List of Figures

List of Tables

Acknowledgements

My time at the University of Washington has been productive and enjoyable due to support from a broad community here. First and foremost, I could not have asked for a better dissertation committee. I want to thank my advisor, Ian Joughin, for being a role model in dedication to efficiently solving problems and taking a broad, big-picture view to understanding the natural world. Ben Smith has always had an open door and has always been available for a thoughtful answer. Michelle Koutnik created an opportunity for me to go to the field and has always been available for scientific or personal advice. Knut Christianson brought unexpected diversity as the only member of my committee not to have earned his PhD at the University of Washington, and in addition to providing advice on the science has been an important mentor and source of guidance as I finish my degree.

A number of other faculty have been instrumental to my continuing success. Twit Conway took me to Antarctica three times, and these experiences have broadened my perceptions of glaciology and taught me new skills unique to polar environments. T.J. Fudge was a graduate student when I arrived at UW, but after becoming faculty during the last year he has become an important mentor provided an enormous amount of guidance and support both in working on the fourth chapter of this thesis and my searching for subsequent employment. Ed Waddington and Steve Warren taught many courses in which I learned about ice and I am indebted to them for whatever breadth of glaciological knowledge I have.

I also wish to acknowledge the incredibly supportive graduate student community in Earth and Space Sciences. My officemates through the years, particularly Max Stevens, Laura Kehrl, David Shean, and Dan Kluskiewicz, have been there as friends outside the office and distractions while

inside. Many other graduate students have also made my time here more enjoyable—Shelley Chestler, Todd Anderson, and Adam Campbell to name a few. I also would not have as prepared to come back to work each day if not for the support of my myriad housemates, particularly Andrew, Shari, Todd, Anabelle, Hannah, and Ben.

Thanks to Julia for encouraging me through the last few years, for always listening, and for still being here on the other side.

Finally, I want to thank my family for their unconditional support through all of my education and, perhaps someday, beyond.

Chapter 1 Introduction

1.1 Motivation

The Antarctic ice sheets gains mass through accumulation of snowfall, and this mass is primarily evacuated through fast-flowing pathways termed ice streams. Ice streams generally reach the ocean and go afloat in an area referred to as the grounding line/zone, forming floating extensions called ice shelves. Due to cold temperatures inhibiting surface melt, the ice sheets' mass is lost through an approximately equal combination of oceanic melting beneath these ice shelves and iceberg calving from their fronts (Depoorter et al., 2013; Eric Rignot et al., 2013). Recent work indicates that West Antarctica in particular is losing mass, potentially at an accelerating rate, contributing 7.6 ± 3.9 mm to sea level rise between 1992 and 2017 (Pritchard et al., 2009; A. Shepherd et al., 2018). If melted or otherwise evacuated into the ocean, the Antarctic ice sheets would contribute ~58 m to global mean sea level (Fretwell et al., 2012), though actual contribution to sea level during past interglacials was likely <10 m higher than present (Kopp et al., 2009). In 2007, the Intergovernmental Panel on Climate Change (IPCC) concluded that "The state of understanding [of ice sheet dynamics] prevents a best estimate [of 21st-century sea level rise] from being made" (IPCC, 2007). While significant progress has been made, the 2013 IPCC report still argued that "The Antarctic ice sheet represents the largest potential source of future SLR" (Ciais et al., 2013). The difference in impacts upon coastal populations from the lower and upper bounds of this uncertainty is profound; more than twice as many Americans are projected to be displaced under the highest rather than lowest sea-lever rise scenarios (Dahl et al., 2017). Figure 1-1 shows projected 21st-century sea level rise and population displaced in the coastal United States under a likely scenario, though the effects of sea-level rise are global, and tens of millions of people would be displaced in other countries under such a scenario.

1.2 Changes to the Antarctic ice sheets

The most notable recent change to the Antarctic ice sheets is marginal thinning, generally localized to the outermost 200 km (e.g., Pritchard et al., 2009), largely thought to be instigated by ocean-forced sub-shelf melting (Jacobs et al., 2012; Rintoul et al., 2016). However, ice-sheet dynamics create long responses to forcing, so observed changes are a superposed response to past and present forcings (e.g., Jenkins et al., 2018). Moreover, the future evolution of the ice sheets will depend not only on future forcing but also on the continuing adjustment necessitated by the disequilibrium of their present state. This superposition of responses suggests that it is useful to disentangle the drivers of present-day change. For example, if observed retreat is predominantly due to contemporaneous forcing, we might conclude that further forcing is required for continued retreat. Conversely, if much of the response can be attributed to internal dynamics, we might argue that changes would continue regardless of forcing until something about the system changed (e.g. the grounding line retreated to a stable, prograde slope).

The rate at which marginal changes will affect the thick, grounded ice-sheet interiors is arguably the glaciological question of most societal interest; only ice that sits above floatation contributes to sea level, and cold surface temperatures in the Antarctic imply that interior ice is unlikely to melt in-situ. For the marine-based West Antarctic Ice Sheet (WAIS), grounding-line retreat can reduce the distance that ice needs to be transported to reach the ocean. However, for the land-based East Antarctic Ice Sheet (EAIS), the extent of grounding-line retreat is inherently limited by the location where the bed exceeds sea level. Thus, loss of the EAIS ice presently above floatation requires transportation to lower elevation and/or latitude where melt or calving is possible, and changes to EAIS volume can only occur as rapidly as ice can be evacuated to the ocean. A change in flow that could cause such evacuation is unlikely to be initiated in the interior of the ice sheet

where changes to accumulation or temperature would take thousands of years to affect flow, but instead rapid (order decades to centuries) loss is only expected to result from an upstream propagation of marginal imbalance.

While rapid contribution of the Antarctic ice sheets to sea-level rise requires thinning and speedup of presently slow flowing, interior regions, knowledge of past changes to interior ice flow is limited. Geologic evidence indicates that ice was hundreds of meters thicker near the margins of the EAIS during last glacial maximum (LGM; see review in Mackintosh et al., 2014). Ice-core evidence and associated modeling indicate that the EAIS interior was ~100-150 m thinner due to diminished snowfall at LGM temperatures (e.g., Lorius et al., 1984; Parrenin et al., 2007). By contrast, geologic evidence suggests that the WAIS was ~125 m thicker during the LGM (Ackert et al., 2007). However, collapse of the WAIS during past warm periods is indicated by geologic evidence (Scherer et al., 1998), sea-level records (Dutton et al., 2015), and ecological evidence (Barnes & Hillenbrand, 2010). Nevertheless, the available data are spatially and temporally sparse, and inferences of past ice thickness are much more common than estimates of past flow. As a result, the speed with which marginal changes have propagated upstream in the past, as well as how current changes may influence interior catchments, remains largely unconstrained by data.

In the absence of direct evidence, results from numerical models are perhaps the most important indicator of how quickly marginal changes can spread inland. Recent modeling studies find that changes to ice flow might rapidly propagate into the deep interior and cause significant thinning of the East Antarctic ice sheet (e.g., DeConto & Pollard, 2016; Mengel & Levermann, 2014). For the WAIS, modeling studies indicate that present marginal changes will propagate inland unabated regardless of forcing (Favier et al., 2014; I. R. Joughin et al., 2014). However, these studies remain limited in scope; while some large, likely vulnerable drainages have been studied in detail, most

have only been modeled in coarse, continental-scale models (Golledge et al., 2012; Pollard et al., 2015). However, there are severe limitations to assessing future ice-sheet stability with these large-scale models; the large domains prevent detailed assessment of individual catchments, bedrock protuberances that could afford stability may be averaged out over the coarse grid scales, use of simplified physics is necessitated by the large domains, and the models are often run from initial conditions that fail to accurately capture modern ice-sheet geometry. Given these limitations, smaller-scale models with problem-specific quality control of data, fine resolution in areas of interest, appropriate physics, and initial conditions appropriate to the problem, when targeted towards those ice streams thought to be most crucial for overall ice-sheet stability, are a key tool to understanding future contributions to sea level rise.

In this dissertation, I use a combination of observations and numerical models to understand past, present, and likely future changes to the Antarctic ice sheets. I focus on two study areas (Figure 1-2), investigating modern changes in melt, ice-flow speed, grounding-line position, and ice thickness in the Amundsen Sea Embayment region of the WAIS and at millennial-scale changes in accumulation and ice velocity in the EAIS interior. These changes in velocity in the EAIS interior likely result in part from gradual changes to interior accumulation, but upstream propagation of marginal effects also likely played a role in causing the observed change in speed, linking this work on long-term changes to that on recent changes to the WAIS margin.

1.3 Organization

Chapter 2 synthesizes existing remote sensing observations to understand the recent retreat of Smith glacier and Crosson and Dotson ice shelves in West Antarctica. These results were published in *The Cryosphere* as **Changes in flow of Crosson and Dotson Ice Shelves, West Antarctica in response to elevated melt** (Lilien, Joughin, et al., 2018). This manuscript uses flux divergence to

calculate melt rates through time over these ice shelves, identifying significant ongoing imbalance. Using inverse methods, it identifies areas of shelf weakening that were likely important for the speedup of these glaciers. Finally, using the melt patterns, grounding line position, and ice-shelf topography we speculate on the timing of the perturbation that initiated the imbalance of these glaciers.

Chapter 3 uses a suite of prognostic ice-flow models to determine the importance of different processes affecting the ongoing retreat of Smith, Pope, and Kohler glaciers. These results will soon be submitted as a manuscript entitled **Melt at grounding line controls observed and future retreat of Smith, Pope, and Kohler glaciers** to *The Cryosphere*. The goals of this study are twofold: attempt to replicate recent observed changes to Smith glacier using ice-flow models and assess the likely future evolution of this system. The results indicate that sustained, elevated melt near Smith Glacier's grounding line was necessary to cause the observed retreat. A number of the simulations successfully replicated the observed retreat of Smith glacier's grounding line, the pattern of thinning, and some of the observed speedup. Those simulations that matched observations all indicate that continuing retreat is likely over the next century.

Chapter 4 combines geophysical and ice-core measurements to constrain the accumulation and ice-flow history near the South Pole during the last 10,000 years. This work was published in *Geophysical Research Letters* as **Holocene ice-flow speedup in the vicinity of South Pole** (Lilien, Fudge, et al., 2018). Using GPS and radar measurements, we construct an estimate of present-day accumulation upstream of the South Pole Ice Core and determine what the modern accumulation rate is at a given travel time to the core. We compare this accumulation record to the accumulation inferred directly from the core's depth-age relationship. This comparison reveals

that the accumulation pattern and flow direction have been approximately constant for 10,000 years while ice-flow speeds have increased by ~15% during that time.

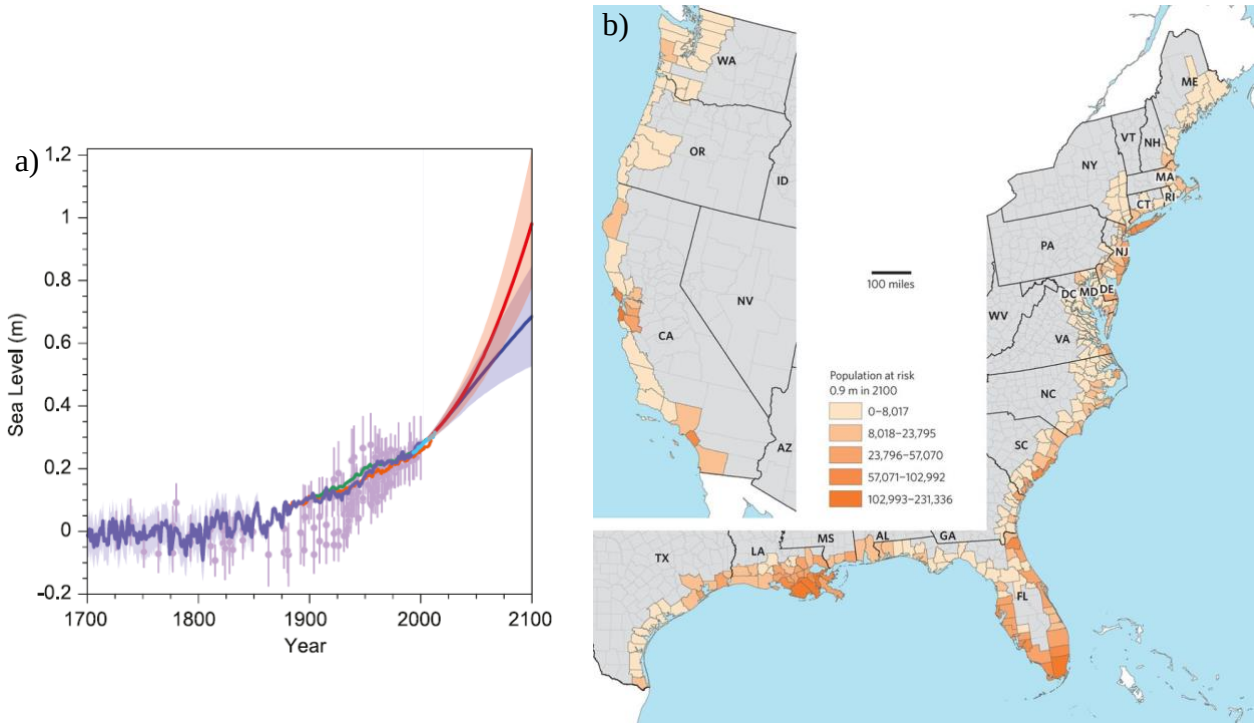

Figure 1-1: Likely 21st-century sea-level rise and its effects upon the coastal United States.

a. Observed and projected sea level rise from the IPCC fifth assessment report (Ciais et al., 2013). **b.** Effects of 0.9 m (3 ft) of sea level rise on the coastal united states (Hauer et al., 2016). Colors show population affected in a given county; gray counties are excluded from the analysis. Projection includes expected population growth. Under this scenario, 4.2 million people would have their homes inundated.

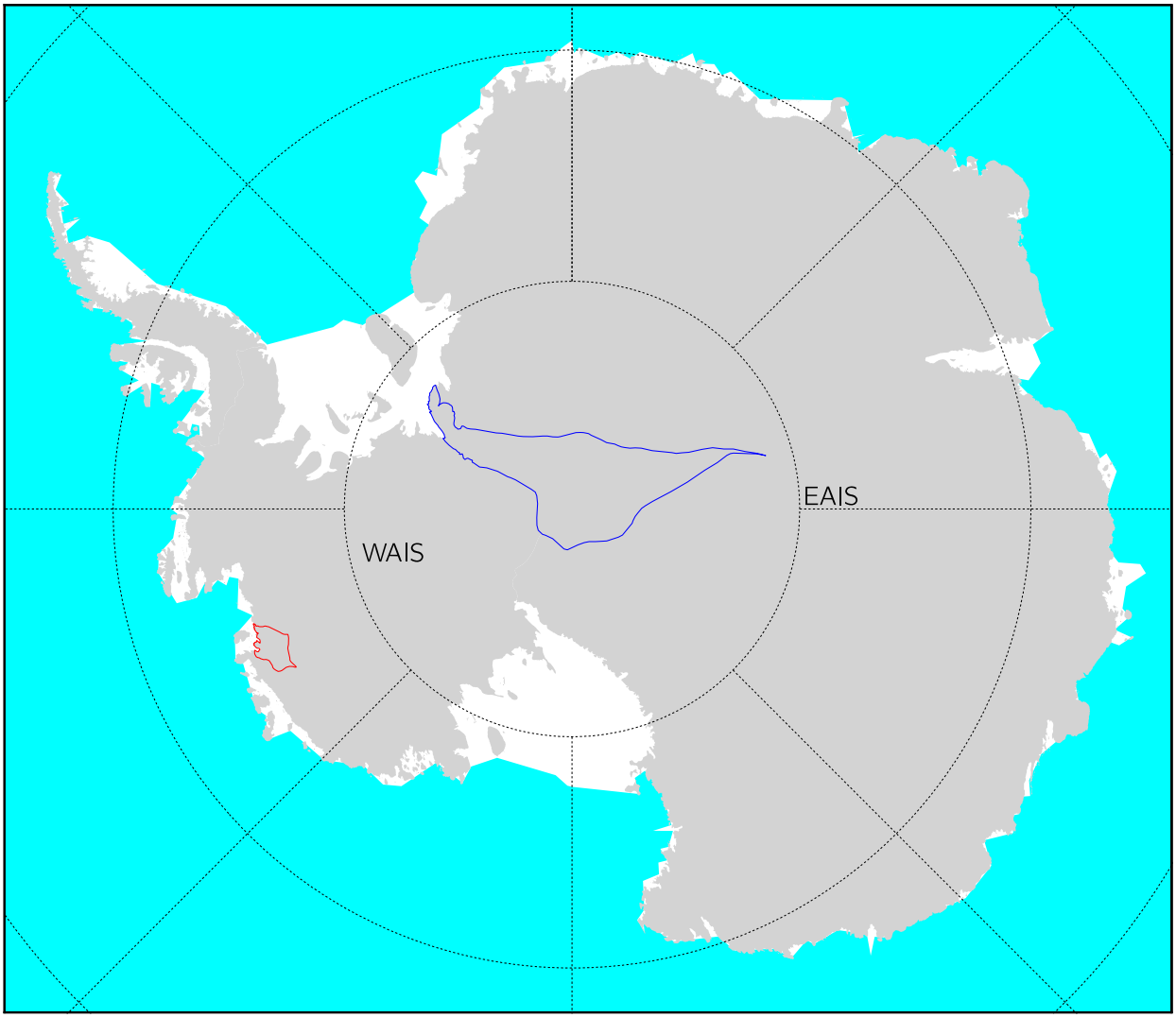

Figure 1-2: Locations of areas studied in this thesis.

Red outline shows drainage area of Smith, Pope, and Kohler glaciers, and shaded red region shows location of figures in Chapter 2 and Chapter 3. Blue outline shows the drainage area of Academy glacier, with shaded blue area showing location of figures in Chapter 4.

Chapter 2 Changes in flow of Crosson and Dotson Ice Shelves, West Antarctica in response to elevated melt

Abstract. Crosson and Dotson Ice Shelves are two of the most rapidly changing outlets in West Antarctica, displaying both significant thinning and grounding-line retreat in recent decades. We used remotely sensed measurements of velocity and ice geometry to investigate the processes controlling their changes in speed and grounding-line position over the past 20 years. We combined these observations with inverse modeling of the viscosity of the ice shelves to understand how weakening of the shelves affected this speedup. These ice shelves have lost mass continuously since the 1990s, and we find that this loss results from increasing melt beneath both shelves and the increasing speed of Crosson. High melt rates persisted over the period covered by our observations (1996-2014), with the highest rates beneath areas that ungrounded during this time. Grounding-line flux exceeded basinwide accumulation by about a factor of two throughout the study period, consistent with earlier studies, resulting in significant loss of grounded as well as floating ice. The near doubling of Crosson's speed in some areas during this time likely is the result of weakening of its margins and retreat of its grounding line. This speedup contrasts with Dotson, which has maintained its speed despite high, increasing melt rates near its grounding line, likely a result of the sustained competency of the shelf. Our results indicate that changes to melt rates began before 1996 and suggest that observed increases in melt in the 2000s compounded an ongoing retreat of this system. Advection of a channel along Dotson, as well as the grounding-line position of Kohler Glacier, suggest that Dotson experienced a change in flow around the 1970s, which may be the initial cause of its continuing retreat.

2.1 Introduction

Glaciers in the Amundsen Sea Embayment are susceptible to internal instability triggered by increased ocean melting of buttressing ice shelves and are currently the dominant source of sea level rise from Antarctica (A. P. Shepherd et al., 2012). Observations (E. Rignot et al., 2014) and modeling (Favier et al., 2014; I. Joughin et al., 2010; I. R. Joughin et al., 2014) suggest that collapse is potentially underway on Pine Island and Thwaites Glaciers, the largest in the region. The neighboring Smith, Pope, and Kohler Glaciers thinned at 9 ma^{-1} just upstream of their grounding lines from 2003-2008, outpacing the mass loss of those larger catchments in relative terms (Pritchard et al., 2009). The lower reaches of these glaciers, which discharge to Crosson and Dotson Ice Shelves (for brevity, we hereafter refer to these ice shelves simply as Crosson and Dotson), doubled their speeds, as their respective grounding lines retreated by as much as 35 km in places from 1996 to 2011 (E. Rignot et al., 2014). During this same period, portions of Crosson sped up at a rate comparable to the grounded areas upstream, while Dotson remained at near-constant velocity (J. Mouginot et al., 2014). Thus, this pair of ice shelves with differing speedup but similar incoming fluxes and neighboring catchments provides an ideal area in which to study the processes controlling ice-shelf stability.

Ice shelves affect upstream dynamics by exerting stresses at the grounding line. For ice masses, the driving stress, τ_d, is resisted by basal drag, τ_b, longitudinal stress gradients, τ_L, and lateral stress gradients, τ_W. To maintain force balance, any reduction in resistance must be compensated by increases in other forces. This adjustment generally causes the glacier to speed up to increase strain-rate dependent stresses (τ_L and τ_W) within the ice. Reduction in ice-shelf resistance (also called buttressing) can be caused by thinning (e.g. from increased basal melt) or changes in extent (e.g. from shelf breakup or increased calving). Weakening of ice-shelf margins, due to heating,

fabric formation, or crevassing or rifting (through-propagating crevasses) also effectively reduces the lateral stress gradients and reduces buttressing (C. Borstad et al., 2016; Macgregor et al., 2012). Despite either mechanical or rheological "weakening", marginal ice can still exert a greater resistance to flow as a glacier speeds up due to the dependence of stress on strain rate.

Areas of compression and tension in ice shelves have been identified as key to shelf stability (Doake et al., 1998; Sanderson, 1979). There is generally a region of tensile stress near the calving front, while upstream of this region, some components of the stress tensor are in a compressive regime; the boundary between the two is often arcuate, and thus is referred to as a "compressive arch." Changes seaward of the arch have little effect on upstream dynamics since the shelf is essentially freely spreading in this region. Changes at or upstream of the arch, such as rifting, or other weakening, can cause widespread speedup because compression, and thus resistance to upstream flow, is reduced.

The dynamics and stability of ice shelf/ice stream systems are also strongly controlled by grounding-line position. Retreat of the grounding line along a landward-sloping (retrograde) bed causes imbalanced flux due to the nonlinear dependence of ice flux across the grounding line on ice thickness there in what is termed the marine ice-sheet instability (Weertman, 1974). Theoretical work has shown that, once perturbed, a grounding line on a retrograde bed will retreat until it reaches a prograde slope (Christian Schoof, 2007). Additionally, ungrounding increases the sensitivity to melt by exposing more ice to the ocean (Jenkins et al., 2016). In the case of a retrograde bed, the deepening of the grounding line caused by ungrounding also increases melt because the melting point decreases with depth. For glaciers along the Amundsen Sea, this effect can be intensified because warm, dense circumpolar deep water generally intrudes at depth and results in elevated melt at deeper grounding lines (Jenkins et al., 2016; Thoma et al., 2008). Retreat

of the grounding line thus causes both imbalanced flux at the grounding line and allows elevated melt rates beneath floating ice. Theoretical arguments provide some insight into the importance of rifting, ungrounding, and loss of buttressing in idealized conditions, but their role in controlling flow during complex evolution of real ice streams is not fully known. Here we investigate the role of these processes in recently observed speed and thickness changes of Crosson, Dotson and their tributary glaciers.

2.1.1 Study Area

Pope Glacier and the eastern branch of Smith Glacier together feed Crosson, while the western branch of Smith Glacier and Kohler Glacier feed Dotson (Figure 2-1). The terminology for these tributaries has varied in the literature, and we adopt the names used in Scheuchl et al. (2016) for consistency and clarity. The largest grounding line retreat (>2 km a^{-1}) occurred in the area where the branches of Smith Glacier flow together before splitting into their respective shelves (Figure 2-2). The grounding-line position of Smith Glacier was relatively stable from 1992 to 1996, but it then retreated substantially in the 18 years following (E. Rignot et al., 2014; Scheuchl et al., 2016). By contrast, the grounding line of Kohler experienced limited retreat (~0.2 km a^{-1}) from 1996 to 2011 and subsequently re-advanced to near its 1996 position by 2014 (Scheuchl et al., 2016). Though data are unavailable for intermediate dates, Pope Glacier's grounding line retreated by 11.5 km (0.64 km a^{-1}) from 1996 to 2014 (Scheuchl et al., 2016). The ice generally thinned most strongly over the areas that ungrounded and up to ~15km upstream (contours in Figure 2-2). This correspondence between thinning and retreat is spatially coincident with speedup, which was strongest over grounded portions of Smith Glacier. Ice speeds in the strongly thinned, grounded area and downstream on Crosson peaked in 2009 and 2010 then declined slightly by 2014. There were also significant changes in the extent of ice at the margins of Crosson (~250 km^2 of ice extent

lost) and thus in the amount of contact with its sidewalls and with the tongue of Haynes Glacier (Figure 2-1b) through this period. Digitized shelf-front positions throughout the ASE indicate extensive rifting of Crosson, resulting in detachment from both of its margins, as well as breakup of the Haynes Glacier tongue from 1984 to 2004 (Macgregor et al., 2012), which could have reduced the ability of the shelf to transmit resistive stresses. No similar changes in extent were observed over Dotson.

The extensive and synchronous changes in the ASE have mainly been attributed to changes in basal melt (e.g. I. R. Joughin et al., 2012 and references therein) caused by warming ocean water or increased intrusion of warm, salty circumpolar deep water (Jenkins et al., 2010; Pritchard et al., 2012; Thoma et al., 2008). Recent work has used radio echo sounding (RES) data to infer thinning rates of 70 m a^{-1} (Khazendar et al., 2016), but the extent of these estimates is limited in space and time, and converting to a melt rate requires assumptions about the magnitude of dynamic thinning in the area, and about the steady-state melt rates. Gourmelen et al. (2017) used thinning rates from Cryosat-2 to obtain a more spatially complete record of melt rates under Dotson, particularly focusing on melt rates in a channel beneath the shelf (Figure 2-1), and found that melt rates in the channel are much higher than the surrounding ice (though lower than at the grounding lines of Smith and Kohler). Observations of ocean temperature in front of Crosson are sparse due to persistent sea ice and ice mélange, though there are observations elsewhere in nearby Pine Island Bay (Jacobs et al., 2012; Wåhlin et al., 2013). Recently, the front of Dotson has been better instrumented, and observations show inflow at the eastern margin of the shelf and outflow at the western margin (Ha et al., 2014; Miles et al., 2015), indicating clockwise circulation beneath the shelf. The inflow is persistently warm at depth while the outflow is cooler and fresher, indicating the presence of meltwater. Available data suggest that in 2006, water in Pine Island Bay, which

may access Crosson, was about 0.7°C warmer, and less variable in temperature, than the inflow to Dotson (Jacobs et al., 2012; Walker et al., 2007). However, attempting to infer melt rates beneath the shelves from these few measurements is challenging. Furthermore, sub-ice-shelf bathymetry has only recently become available (Millan et al., 2017), limiting model-based analyses of ocean circulation beneath these shelves.

Previous ice-flow modeling, which excluded the floating ice, suggested that these glaciers will continue to retreat even in the absence of a change in forcing (D. N. Goldberg et al., 2015). Since changes in the ASE are thought to be ocean-forced, however, understanding of processes over the floating ice and at the grounding line are key to explaining recent behavior and to any prediction of future behavior. Here we use remote-sensing observations of ice velocities, surface elevations, and ice-bottom elevations of these ice shelves through time to determine the partitioning of their mass loss and to constrain snapshot inversions of their viscosity. We use the history of melt, terminus position, and shelf viscosity to understand the causes of changes to these shelves' mass balance and speed.

2.2 Data

Before describing the calculations of mass loss and modeling, we first summarize the data used in this study.

2.2.1 Velocity

Surface velocities were obtained from both synthetic aperture radar (SAR) and optical satellites. The SAR velocities come from the European Remote-sensing Satellites (ERS-1 and -2) for 1996 and the Advanced Land Observation Satellite for 2006-2010. These SAR data were processed using a combination of interferometry and speckle tracking (I. R. Joughin, 2002). We used feature

tracking of Landsat-8 imagery to obtain velocities for the 2014-2015 austral summer. Velocity data for 2006 and 2011 are part of the NASA Making Earth System Data Records for Use in Research Environments (MEaSUREs) data set (J. Mouginot et al., 2014). Errors range from a few meters per year over slower grounded ice to >100 m a^{-1} over Dotson in 1996 due to the short satellite repeat period and errors introduced by tidal displacement.

2.2.2 Surface elevations

To estimate past surface elevations, we began with elevations from a high-quality digital elevation model (DEM) with elevations relative to the EGM2008 geoid. This reference surface is a mosaic DEMs created through processing of stereo imagery from the DigitalGlobe WorldView/GeoEye satellites (D. E. Shean et al., 2016), using imagery spanning 2010-2015. Most of the stereo pairs used to create this mosaic come from the 2010-11, 2012-13, and 2013-14 austral summers, so we assign the mosaic an approximate timestamp of January 1, 2013. This surface elevation product is posted at 32m, and we estimate the error to be ±1.0 m. To find surface elevations in different years, we added the observed thinning rates, as discussed below, to this reference surface. Because there are published estimates of thinning rates over the ice shelves (Fernando S. Paolo et al., 2015; A. Shepherd et al., 2004), we used these rates for floating ice and addressed grounded ice separately.

Over grounded ice, we used thinning rates derived from a combination of points from ICESat-1 and the Airborne Topographic Mapper (ATM) as well as DEMs produced from stereo pairs of Worldview imagery; details of how this time series was produced can be found in Appendix A of Goldberg et al. (2015). These observations of surface elevation span 2003-2015, necessitating extrapolation to determine elevations at the beginning of our study period. To extend to 1996, we fit a quadratic function to each pixel of the 2003-2014 elevation change record; the use of a

quadratic description of the thinning follows previous work (Wingham et al., 2009). We then used these thinning functions to calculate surface elevations over these glaciers during 1996-2002. To assess relative to previous methods, we calculated estimated surface elevations for 2003-2008 using this quadratic function to test its ability to match the available ICESat-1 data. Residuals are smaller than those resulting from using a quadratic fit to the elevation and thinning rate from 2004 alone, as was done in Mouginot et al. (2014). While we are unable to formally calculate the uncertainty of the surface elevations produced by this extrapolation, we estimate it as ~50% of the change from the earliest measurement (in 2003).

Over floating ice, we used 1994-2012 thinning rates derived from satellite radar altimetry data by Paolo et al. (2015). The results from Paolo et al. (2015) show little spatial variability over these particular shelves, and so we used the thinning rates for the middle of each shelf where low surface slopes should lead to the smallest errors. These values were 3.1 m a^{-1} for Crosson and 2.6 m a^{-1} for Dotson. Because of relatively high surface slopes and the 30-km resolution of these estimates, the thinning rates are not accurate fully to the margins of the shelves, and there are ~5 m a^{-1} differences in our thinning function upstream and downstream of the grounding line. The thinning rates on the grounded ice are more accurate because the entirety of any change to thickness is manifest in the surface elevation while over floating ice ~90% of the thickness change is accommodated through raising the ice bottom due to hydrostatic balance. Thus, we smoothed the thinning over the shelves for 10 km downstream of the grounding line to preserve continuity and reasonable surface slopes.

2.2.3 Ice-bottom Elevations

We use a 1-km bed elevation dataset generated from all available airborne RES data with an anisotropic interpolation routine that weights measurements along flow more heavily than those

across flow; details can be found in Medley et al. (2014) and the supplementary materials to Joughin et al. (2014). This method reduces many of the artifacts that can occur when interpolating sparse ice thickness measurements, while avoiding making any assumptions about the present state of balance (e.g. assumptions for mass conservation methods (Morlighem et al., 2011)), though like other methods used to interpolate radar data it still has high uncertainty due to the sparseness of the underlying radar profiles. We assume bed elevation errors of ~50 m for the study area.

Over floating ice, we used the surface elevation for a given year and an assumption of hydrostatic equilibrium to calculate the elevation of the lower ice surface. In doing so, we first determined the firn-air content by choosing the value that minimizes the misfit in ice thickness between coincident surface elevation (converted to ice thickness by subtracting the air content and assuming floatation) and ice thickness measurements; elevation and thickness measurements were taken from the ATM and Multichannel Coherent Radar Depth Sounder (MCoRDS) flown on NASA's Operation IceBridge. The ice thickness measurements from the MCoRDS radar are calculated from the two-way travel time of the radar using a wave speed for pure ice, but the air content in the firn changes the radar wavespeed. In our minimization, we convert the thickness to a travel time, reversing the MCoRDS processing methods, then convert the travel time back to thickness using a wavespeed that accounts for the air content of the firn. This approach provides point measurements of firn-air content along tracks separated by several kilometers, which we then gridded and subtracted from the surface elevation, resampled to 400-m posting, before applying the assumption of hydrostatic equilibrium to compute the ice bottom elevation. We find the firn-air content to range between 12-18 m across most of the ice shelves (Figure A-2); a firn model forced with output from RACMO2.3 shows greater firn-air content than we observe, generally between ~20-25 m over these shelves (Ligtenberg et al., 2011). Residuals between the ice

thickness obtained using firn-air content estimates and direct measurements of ice thickness from MCoRDS have an RMS of 22 m. This error is larger than the ~10-m crossover precision in the MCoRDS data in this area, but comparable to the absolute accuracy of those measurements, which include error from uncertainty from the dielectric constant, limited sampling rate, and uncertainty in picking the reflector.

2.2.4 Ice-front positions

We digitized the shelf-front positions of Crosson and Dotson from 2012 to 2016, extending the earlier 1972-2012 record (Macgregor et al., 2012). The shelf-front positions were traced on Landsat-8 imagery, using the panchromatic data (band 8). Shadowing and brightening of steep areas cause an approximately four-pixel (±60m) nominal uncertainty in the front position, though actual error is ~500m on Crosson due to ambiguity in discriminating between ice front and persistent mélange.

2.3 Methods

We derived annual flux, melt, and calving rates through time using the observed velocity and ice thickness. We compared these values to flux at the grounding line and accumulation on the shelves to determine changes in the ice-shelf mass balance. Since stresses in the ice cannot be measured remotely, we performed snapshot inversions for viscosity using a numerical model to quantify how changes in velocity and geometry affected the stress balance and strength of Crosson and Dotson.

2.3.1 Flux and melt calculation

Following earlier work (J. Mouginot et al., 2014), we used the average of five closely spaced gates to calculate inflow and outflow fluxes along the shelf boundaries. For grounding-line flux, gates were drawn at 2-km intervals beginning just upstream of the 2014 grounding line. Onto each gate

profile, we interpolated surface and bed elevations and the component of velocity orthogonal to the gate. We filled gaps < 3km wide via 2-D linear interpolation of surrounding velocities and filled larger gaps by 1-D linear interpolation between the velocities at that point the two closest years with sufficient coverage. Where we have velocity data, we take the error to be the formal value, and where we have interpolated we estimate it to be the difference between the interpolated value and the values at neighboring years.

We calculated melt rates over different portions of the shelves to understand the spatial distribution of melt. Basal melt is effectively a downward flux of ice out of the shelf bottom, so to calculate melt we divided the shelves into polygons (Figure 2-3a), calculated the incoming and outgoing flux for each polygon, then used mass conservation to determine the melt rate. We used the average flux through five parallel gates on each side of the polygons to reduce errors in the horizontal fluxes. Where possible, we located the upstream sides of the polygons over ice that was grounded in 1996 to reduce errors in the velocity caused by tidal variation over the short repeat cycle employed by ERS during this period. We estimate the error in the margins of floating ice, which propagates to error in the area, to be 5%; this error does not affect our calculation of melt for individual polygons but does affect our estimate of total melt on each shelf. To relate the flux into and out of a polygon to the melt rate, we integrated the mass change of the polygon and applied divergence theorem:

$$\int_{\Omega} \dot{m}_b \, d\boldsymbol{A} = \int_{\Omega} \left(-\nabla \cdot \boldsymbol{Q} + \dot{m}_s + \frac{\partial H}{\partial t} \right) d\boldsymbol{A} = -\oint_{d\Omega} \boldsymbol{Q} \cdot \hat{\mathbf{n}} d\boldsymbol{s} + \int_{\Omega} \left(\dot{m}_s + \frac{\partial H}{\partial t} \right) d\boldsymbol{A} \quad (1)$$

where $\dot{m}_b$ is the basal melt rate, $\boldsymbol{Q}$ the depth-integrated flux, $\dot{m}_s$ the surface mass balance (SMB, water equivalent), $\frac{\partial H}{\partial t}$ the thickness change, Ω a polygon with boundary $d\Omega$, $\hat{\mathbf{n}}$ the unit normal to

the boundary, **A** the area of the polygon, and **s** the distance along the boundary. To determine melt rates from the flux balance of each polygon, we used the rate of thickness change from Paolo et al. (2015) and SMB from RACMO2.3 (Van Wessem et al., 2014). For the SMB, we use the annual mean for 1979-2013, which has an uncertainty of ±20% (Van Wessem et al., 2014). The assumption of a spatially uniform thinning rate for each shelf introduces additional error that is difficult to quantify, but without more measurements of surface change this difficulty is unavoidable. We computed mass loss rates for both ice shelves and catchments. The former is useful because the ablation on the shelves is greater than the grounding line flux, causing them to lose significant mass annually, while the latter gives an indication of the system's contribution to global sea level rise and is useful for comparison to other studies.

2.3.2 Modeling

We used a diagnostic model implemented in Elmer/Ice (Olivier Gagliardini et al., 2013; Zwinger et al., 2007) to infer ice-shelf viscosity. Elmer/Ice is an open-source, finite element software package capable of solving the full Stokes equations in three dimensions, or lower-order approximations to ice flow such as the shallow-shelf equations (Olivier Gagliardini et al., 2013; MacAyeal, 1989). We used a three-dimensional, full-Stokes model with separate domains for grounded and floating ice. While the assumptions of the shallow-shelf equations are likely applicable at least to the floating portion of our domain, we implemented the Full-Stokes model to accurately capture the effects of ~10 pinning points beneath these shelves and avoid approximations to the stress state.

We performed multiple diagnostic runs in which we varied the model geometry to reflect different years, which allowed us to infer properties through time as a series of snapshot inversions. The upstream margins of the model domain were located at the divides in ice flow, determined from

InSAR velocity measurements. We found the downstream margin using the digitized shelf-front positions described above. The grounding-line positions from (E. Rignot et al., 2014; Scheuchl et al., 2016) were used to determine the boundary between the grounded and floating domains for each year. We used these horizontal extents, in conjunction with the different surface and bed DEMs described above, to create a suite of three-dimensional model meshes using the software GMSH (Geuzaine & Remacle, 2009). These horizontally unstructured meshes have a resolution of ~300-m over floating ice. The meshes have eleven vertical layers, with six of these in the bottom third to capture the zone of maximum internal deformation; there is little internal deformation over most of the floating domain, but this concentration of layers is useful for capturing temperature gradients in the ice column and dynamics around pinning points.

To obtain an initial estimate of viscosity for the enhancement factor inversions, we first determined a temperature profile in the ice. This initial estimate was made using a steady-state thermo-mechanical model in Elmer/Ice. The model solves the Stokes equations to determine advection, with ice viscosity as a function of temperature, and solves an advection-diffusion equation for heat using limiters to prevent ice from going above the pressure-melting point (Zwinger et al., 2007). Strain heating and frictional heating at the bed were both included in this temperature model. For boundary conditions, we used surface temperatures from RACMO2.3 (Van Wessem et al., 2014) and geothermal heat flux estimates from geomagnetics (Maule et al., 2005). We first ran the temperature model over grounded ice; the downstream temperatures from the grounded ice were then used as the upstream boundary condition for a similar model of the floating ice.

After obtaining an initial viscosity from the temperature model, we used inverse methods to infer the enhancement factor that produced modeled velocities that best match observations. The enhancement factor alters the viscosity of the ice relative to that predicted solely by modeled

temperature. It would be possible to use the model to find a depth-variable enhancement factor, but, to have the number of degrees of freedom in the inversion match the number of observables, we instead determined a single depth-independent value. We began with a profile of viscosity with depth from the temperature model, and used adjoint methods (MacAyeal, 1993; Morlighem et al., 2010) to infer an enhancement factor that results in the best fit to observations for each column of ice. Because we were inferring variations along shear margins with sharp transitions in velocity, temperature, and rheology, we did not apply regularization to the inversion for the enhancement factor, and simply minimized the areally integrated misfit between observed and modeled velocity. The lack of regularization may have concentrated the weakening or strengthening into smaller areas than would have been found with regularization, but any solution, regularized or not, likely would have to introduce weakening into these same areas in order to reproduce the velocity field. Thus, the lack of regularization likely did not affect the general spatial pattern of weakening.

For boundary conditions, we used observed surface velocity for all depths over lateral margins (including shear margins, calving front, and grounding line). For the basal boundary, we used zero basal shear stress over floating ice and basal shear stress equal to half the driving stress over the pinning points observed from SAR grounding lines.

2.3.3 Stress Changes

The location of changes in rheology relative to the compressive arch is an important factor in determining whether those rheological changes affect the broader flow patterns of the shelf. To determine the location of the compressive arch on Crosson and Dotson, we used the modeled stress field to calculate the stress associated with shelf spreading, $\tau_L = 2\bar{\tau}_{xx} + \bar{\tau}_{yy}$ where $\bar{\tau}_{xx}$ and $\bar{\tau}_{yy}$ are the depth averaged deviatoric stresses along and across flow. We chose this criterion because

where it is compressive it shows resistance to spreading upstream and where it is tensile it indicates a spreading shelf not resisting flow. This approach differs from previous literature, which used the second principal stress to identify compressive arches; other studies choose that criterion in part because the first principal stress is consistently tensile (Doake et al., 1998), which is not the case on Crosson and Dotson, and so ignoring the first principal stress misses an important aspect of the stress balance here.

2.4 Results

2.4.1 Flux and Melt

Figure 2-3 shows the components of the flux balance of Crosson and Dotson throughout the study period. The three columns for each year show the outgoing flux, incoming flux, and loss, respectively. The outgoing flux is partitioned into the melt on different portions of the shelves and the calving flux. The outgoing flux from some polygons is equal to the incoming flux of others; when adding all the melt together the flux across these internal boundaries cancels, leaving the total melt on the shelf. The incoming flux consists of ice-shelf surface accumulation and the flux across the grounding line; we partition the grounding-line flux into a steady-state amount (i.e. the accumulation in the catchment upstream) and any additional amount (in excess of steady state) entering the shelves in each year. The difference between the incoming and outgoing fluxes for the shelves provides an estimate of net mass loss from the shelves, while the difference between upstream accumulation and grounding-line flux yields net loss from grounded ice.

The grounding-line fluxes into Crosson and Dotson both exceeded their upstream accumulation in 1996. By 2014, the fluxes across the grounding lines increased by 30% and 60%, respectively. Increases in outgoing flux (calving and melt) outpaced increases in grounding-line flux for both Crosson and Dotson, leading to loss of shelf volume. Due to Crosson's speedup, its calving-front

fluxes increased from 1996 to 2010 then declined slightly to 2014, while the calving-front flux from Dotson declined due to both thinning and slight slowdown. Total melt beneath each shelf also increased from 1996 to 2010 and declined slightly to 2014. The melt beneath Dotson (27.7 Gt a^{-1}) in 1996 was higher than beneath Crosson (10.9 Gt a^{-1}). This difference is due in part to the much greater area of the shelf (~5200 km^2 vs ~2400 km^2), but also due to high melt rates near the grounding lines of Kohler and western Smith Glaciers, which feed Dotson. Notably, sub-shelf melt rates on Dotson are greater than the grounding-line flux for each of the years surveyed, resulting in loss of shelf volume irrespective of its calving rate.

Figure 2-3 also shows melt for different regions of each shelf. The greatest increase in melt occurred on western Smith Glacier (SW1 in Figure 2-3), but the most intense melt (~23 m a^{-1}) in 1996 was within 10 km of Kohler's grounding line (K1 in Figure 2-3) and rates there remained high through our study period. Melt rates ~10km farther downstream from Kohler (K2) were lower (~7 m a^{-1}) but doubled during the study period. The areas of western Smith Glacier with the highest melt (SW1 in Figure 2-3), found both here and elsewhere (Khazendar et al., 2016), had ungrounded since 1996 (Figure 2-1). Melt rates increased through the study period beneath all portions of Crosson except that nearest the calving front (C2 in Figure 2-3). Melt over areas that were floating throughout the study period is unaffected by ungrounding, so the increasing melt in these areas is indicative of a change in ocean forcing through this time. By contrast, the decrease in melt rates from 2010-2014 may have been caused either by the ice draft shallowing into cooler water or by a change in ocean forcing.

Table 2-1 compares our estimates of flux and melt to those from previous studies. Our estimates of grounding-line flux agree with previous estimates (Depoorter et al., 2013; J. Mouginot et al., 2014; Eric Rignot, 2008; Eric Rignot et al., 2013). Our estimate of the partitioning of the mass

loss, however, differs substantially from Rignot et al. (2013) and Depoorter et al. (2013); this discrepancy stems from different values of the calving-front flux, as well as different data used to determine the thinning. Published estimates of thinning rates range from 2.6 m a^{-1} to 5.6 m a^{-1} over Dotson and do not agree to within their stated errors, leading to a difference of 16 Gt a^{-1} when applied to the whole shelf (Fernando S. Paolo et al., 2015; Pritchard et al., 2012; A. Shepherd et al., 2004). The thinning rates measured via radar altimetry use a longer time series of thickness data (Fernando S. Paolo et al., 2015), and so we expect these values to be more representative of the average thinning over our study period than previous laser-altimeter based estimates, which range from 36-63 Gt a^{-1} (Depoorter et al., 2013; Pritchard et al., 2012; Eric Rignot et al., 2013; A. Shepherd et al., 2010). Additionally, this longer dataset matches recent, high-resolution radar-based estimates (Gourmelen et al., 2017). Some of the range in measured thinning may reflect real multi-annual variability (F. S. Paolo et al., 2018) that is sampled differently during the 5-year laser-altimetry record compared to the 18-year radar-altimetry record. However, even if this discrepancy reflects real variability, we likely underestimate the error in our melt and flux calculations by using a temporally constant thinning rate and propagating only the stated error from Paolo et al. (2015). While using different thinning rates substantially alters the estimated melt, melt rates on Dotson calculated using any of these values are larger than the grounding-line flux. Thus, using a different thinning rate within the range of published values would not substantially alter our conclusions, though it would imply greater magnitude of melt.

2.4.2 Buttressing

Previous work has shown rifts along the margins causing gradual separation of Crosson from the seaward portion of its embayment between 1984 and 2012 (Macgregor et al., 2012). Our tracing of more recent ice-front positions shows that this separation has continued to the present (Figure

2-4a). We find that in 2014 the rifts on the eastern margin of Crosson connected to the ice front, effectively detaching the last ~35 km of the shelf from the right side of the embayment (see labels in Figure 2-4). Since the ice shelf was already separated from its western margin, this detachment left the outer ~35 km essentially as a floating ice tongue within its embayment. Since there have been no large calving events, the central portion of the ice front advanced back to near its 1972 position but provided no buttressing and did not change the force balance.

There was also a progressive loss of contact between the front of Crosson and the Haynes Glacier tongue from 1984-2004 (Macgregor et al., 2012). These changes continued through 2012, and rifting also increased through this period (Figure 2-4b and c). We found the linear extent of ice along three transects near the front of Crosson through time to determine the portion of the ice front that may have experienced back force from neighboring ice. This ice extent is similar to the calving-front position for Haynes Glacier found in MacGregor et al. (2012), but we used two additional transects to determine the locality of effects on the front of Crosson, the Haynes tongue, and the Thwaites tongue. We find a generally decreasing trend starting at least as early as 1984, with reduction to almost no area in contact by 2004 (Figure 2-4d). The approximately steady decline of this tongue suggests there was no sudden drop in resistance at the margin of Crosson, and any speedup caused by the breakup of this tongue would most likely have been gradual, beginning at least as early as the 1980s and continuing into the 2000s.

2.4.3 Modeled Weakening

Figure 2-5 shows the inferred enhancement through time from the diagnostic model, which indicates a reduction in the strength of Crosson's margins from 1996 to 2014. By contrast, there is no notable change in the inferred rheology of Dotson. Stiff ice at the calving front of Crosson is similar to results from Thomas and MacAyeal (1982), which they attribute to ice that is thinner

and cooler than expected. This effect is likely not real, but rather is introduced by the model as compensation for poor estimates of temperature and thickness at the calving front. The general pattern of weakening is consistent with areas of high shear, where increases in strain heating, crystal fabric, or rifting could have caused a positive feedback with speedup; faster ice motion could have caused weakening through strain heating or rifting, allowing further speedup. Because we do not account for spatial variability of thinning within each shelf, what we interpret as weakening could in fact be a result of thinning; i.e. we may infer weaker ice in regions where ice is in fact simply thinner. Similarly, areas where the model identifies strengthening may result from local thickening on those portions of the shelves. While this ambiguity prevents us from interpreting changes in enhancement as a particular physical process, it does not adversely affect our determination of which areas afforded more or less resistance to flow.

2.5 Discussion

Here we examine how variations in ice thickness, melt, and ice strength appear to have affected the flow pattern, grounding line position, and mass balance of these ice shelves. Because of the differing behavior of the shelves, we address different processes over each shelf. On Dotson, melt alone exceeded flux onto the shelf for every year surveyed, implying elevated melt rates at least as early as 1996. Crosson's speedup, which caused more ice to reach the calving front, may have caused its imbalance, and we are unable to determine if Crosson's melt rates would be sustainable in the absence of this speedup. Thus, we first focus on the causes and implications of Dotson's elevated melt and then discuss Crosson's speedup in the following section. Finally, we compare the estimates of melt from this study to previous work and discuss the implications for the dynamics of the system.

2.5.1 Causes of Dotson's imbalance

Changes in the Amundsen Sea Embayment have generally been attributed to oceanic forcing (I. Joughin et al., 2010; e.g. A. Shepherd et al., 2004). It is possible that an increase in ocean heat content prior to our study period may have contributed to Dotson's observed imbalance. In this case, elevated melt rates on Dotson may have directly led to a retreat of its grounding line, resulting in further exposure to melt and continued retreat. Alternatively, some of the change may have resulted from ongoing thinning. For example, model results indicate a glacier catchment may thin for decades, leading to an abrupt retreat of the grounding line (Jamieson et al., 2012; I. R. Joughin et al., 2014). Thus, even modest but sustained thinning could perturb the grounding line from a stable position. In either case, once perturbed, the grounding line may undergo a rapid retreat to another stable position, thus leading to greater exposure of sub-shelf area and elevated melt (e.g. Jenkins et al., 2016). We now present evidence that suggests a large retreat of Kohler's grounding line took place prior to our study period, then evaluate whether ongoing thinning or ocean forcing caused this grounding-line retreat and Dotson's mass imbalance.

2.5.1.1 Prior retreat of Dotson's grounding line

The bathymetry near Dotson's present-day grounding line suggests that any recent unstable retreat would likely have taken place at Kohler Glacier. While the Smith Glacier grounding line was positioned on a bedrock high in 1996, Kohler Glacier's grounding line was ~1200m deep, just upstream of a ~20 km long retrograde slope (Figure 2-6b) (Millan et al., 2017). If the grounding line formerly was positioned downstream of this retrograde slope (e.g. dashed line in Figure 2-6b), it likely would have retreated rapidly if perturbed. The unsustainably high melt rates in this area (K1 and K2 in Figure 2-3) indicate that such a retreat of Kohler's grounding line had likely taken place recently prior to 1992. The overall mass balance for Dotson implies that exposure of K1 and

K2 to ocean forcing would have been the difference between sustainable and non-sustainable melt. Comparing the calving flux and the melt from D1 and D2 alone to the steady-state grounding-line flux (Figure 2-3) shows that Dotson would have been approximately in balance with 1996 melt rates if only this area had been exposed. Adding in the melt found beneath K1 and K2, even at 1996 rates (the lowest in our study period), however, would have resulted in melt exceeding grounding-line flux. Extrapolating back using current thinning rates of ~2.5 m a^{-1}, most of the shelf would have been entirely grounded 150 years prior, implying that the melt rates within this overdeepening could not have been sustained over centennial timescales. Thus, it is possible that some time in the several decades prior to 1990s, the grounding line retreated several 10s of kilometers from our hypothesized position (Figure 2-6 dashed line), increasing exposure to melting in the K1 and K2 region (Figure 2-3).

Velocity data provide an additional constraint on the possible timing of a retreat of Kohler's grounding line. Feature tracking of Landsat imagery gives sparse velocity measurements on Dotson for the period 1974-1982, and comparison of these data with recent velocities suggests that there was no substantial speedup of Dotson from 1974 to the present (Lucchitta et al., 1994; Eric Rignot, 2008). Speedup near the grounding line usually accompanies ungrounding due to the associated loss of basal resistance, so the lack of speedup suggests any substantial grounding line retreat on Dotson likely took place prior to 1974. Combining this lower limit on retreat initiation with the upper limit placed by the unsustainably high melt rates, we infer that the imbalance began years to decades before 1974. Previous work has found that grounding-line flux over Crosson and Dotson combined approximately balanced accumulation in 1974 (Eric Rignot, 2008). That balance is inferred primarily from speedup of the outer portion of Crosson during that time; however, speedup on the outer portion of the shelf can take place independently of speedup near

the grounding line (see section 2.5.2 below). On the other hand, the near-constant velocities on Dotson from 1974-1996, combined with the imbalance in 1996, suggest that Dotson may have been out of balance in the 1970s. Moreover, even if Dotson's grounding-line flux were in balance with upstream accumulation, the melt rates on the shelf may have been elevated. We therefore consider the available data to be ambiguous about the state of balance from the mid 1970s to early 1990s, and thus reconcilable with this proposed timing of retreat initiation.

In summary, observations of grounding line position and velocity are consistent with past retreat of Kohler Glacier due to marine ice-sheet instability (e.g. retreat from the example position shown in Figure 2-6b), and this retreat likely occurred in the years to decades before 1974. This consistency does not, however, identify the initial cause of that retreat, which could have been triggered either by an unstable response to ongoing thinning or by an increase in basal melt. To further investigate these two scenarios, we discuss how the present-day geometry of Dotson, particularly a large basal channel (Figure 2-1c and Figure 2-6a), informs our understanding of its history of melt and flow.

2.5.1.2 History of melt

Surface features on an ice shelf can preserve information about the flow and melt history as ice advects seaward (Fahnestock et al., 2000). To help differentiate whether ongoing thinning or ocean forcing triggered Kohler's grounding line retreat and Dotson's imbalance, we use the large surface trough visible in the surface topography (Figure 2-1c and Figure 2-6a) to estimate the onset and spatial extent of changes on Dotson. Present day melt rates in this channel, particularly after it turns towards the ice front, have been previously studied (Gourmelen et al., 2017), but here we focus on the portion of the channel that is transverse to flow. The surface expression of this portion of the channel is 5-10 km wide in a region where ice speeds are 150-200 m a^{-1}. Downstream of

this channel, the shelf thickens by ~200 m. In steady state, an ice shelf should only thicken along flow if there is basal freeze-on, high SMB, or a narrowing of the embayment. Dotson has nearly parallel sidewalls and the magnitude of the downstream increase in thickness is large compared to the SMB (~0.5-1.2 m a^{-1}; Van Wessem et al., 2014), so these causes can be eliminated. Previous work (Depoorter et al., 2013; Gourmelen et al., 2017; Eric Rignot et al., 2013) found no evidence of large-scale freeze-on beneath Dotson, and we eliminated the possibility of localized freeze-on being the primary cause of the channel by comparing radar observations to floatation levels. Where marine ice is present, ice penetrating radar generally does not propagate into the saline marine ice layer, hence the radar only records the thickness of the meteoric ice. As result, significant differences between the radar (meteoric-only) and hydrostatic-equilibrium (full column) derived thicknesses indicate the presence of marine ice (Crabtree & Doake, 1986; Robin et al., 1983; Thyssen, 1988). No such differences are found for Dotson, indicating little or no marine ice (Further details can be found in Appendix B.1). Thus, having ruled out other causes, we conclude the channel was produced by a transient change in ice flux or melt.

The channel originates near the grounding line on the eastern (shelf-right) margin of Dotson and continues along the grounding line to the western (shelf-left) margin and extends to the shelf front. This pattern is similar to the pattern of ocean circulation inferred from oceanographic measurements. Available data show warm inflow at the eastern margin and meltwater-laden outflow at the western margin, indicating clockwise circulation beneath the shelf (Ha et al., 2014; Miles et al., 2015). This circulation pattern suggests that the channel originates where the warm CDW inflow first comes into contact with the ice shelf draft. Generally, melt that begins at depth is sustained by entrainment of additional warm water as the buoyant meltwater plume rises along the underside of the ice (Jenkins, 2011). Basal melt channels have been observed in many locations

around Antarctica (e.g. Alley et al., 2016), and are thought to form in the location where the meltwater plume rises along the bottom of the shelf (Marsh et al., 2016; Stanton et al., 2013). The shallowing of this channel as it curves along the grounding line to the western margin of Dotson is consistent with this model of channel formation. The abrupt beginning of the channel on the eastern margin and the continuation of the channel to the shelf front on the left are thus consistent with the available oceanographic constraints. However, high resolution measurements of melt from 2010-2016 do not show high melt rates throughout this channel, but rather localized melt near the grounding line along the western portion of the channel before it turns toward the shelf front (Gourmelen et al., 2017). While ice divergence following the initiation of channel incision may have had an effect on the channel width (Drews, 2015), there is no change in the divergence of the measured surface velocities around the transverse portion of the channel (conversely, along the flow-parallel portion there is significant convergence). Thus, any change in width due to divergence is at or below the level of uncertainty in the velocity measurements, and therefore small compared to the advection of the channel. Thus, the present pattern of melt suggests that transverse portion of the channel is at least partially a mark of past thinning rather than a signal of currently elevated melt.

To constrain the timing of the formation of the channel, we assumed that it resulted from a perturbation at the grounding line and used the 1996 velocity to determine how long the perturbation would take to advect to the current channel location (Figure 2-6a). For this calculation, we assume the perturbation happens at or close to the grounding line; since grounding line positions and surface elevations before 1992 are unknown, this is the simplest assumption. Additionally, the present-day concentration of melt immediately near the grounding line in the western portion of this channel suggests such an assumption is reasonable (Gourmelen et al.,

2017). Estimates for the timing of the perturbation are 30-45 years before 2013 (i.e. 1968-1983) for various points along the channel. This timing is consistent with our inference of when a retreat of Kohler's grounding line may have occurred, suggesting that there were widespread changes in melt near Dotson's grounding line in the decades prior to 1974, and that the channel and the retreat of Kohler's grounding line were both consequences of these changes. This timing is consistent with prior work on the upstream propagation of thinning over these glaciers, which found that thinning initiated around 1970±30 at the grounding lines of Smith and Kohler (Konrad et al., 2017), as well as with an altimetry-based study of Dotson, which found that the shelf had been thinning for at least two decades but not more than a century (Gourmelen et al., 2017). Grounding-retreat is thought to have begun on other glaciers in the region at a similar time (e.g. Jenkins et al., 2010), but the complex nature of ice streams' response to perturbations prevents interpreting a synchronous change as evidence of synchronous forcing.

While ocean forcing is likely responsible for these changes, we cannot fully eliminate other possibilities. The most likely alternative is that retreat of Kohler Glacier's grounding line, perhaps due to ongoing thinning, resulted in changes to the circulation patterns beneath the shelf, causing increased melt and channel incision. Exposure of deeper ice at Kohler's retreated grounding line could have led to increased melt not only at the grounding line, but also downstream as meltwater from the grounding line entrained warm water. This increased outflow, which would have risen along the bottom of the shelf as it flowed northward along the left margin of Dotson, may have enhanced overall circulation beneath the shelf, incising the channel as additional warm water cycled through the cavity. Such grounding line retreat may have also resulted in speedup and thus dynamic thinning in the area of the channel as the portion of shelf downstream of Kohler thinned and resistance to flow was reduced. Incision of the transverse portion of the channel through

dynamic thinning would also be consistent with the low melt rates in that area found by Gourmelen et al. (2017).

2.5.2 Causes of Crosson's speedup

Understanding the changes in flow in this area, particularly the observed changes in Crosson's velocity, is important for predicting the future stability of this system as well as understanding the causes of increased calving and grounding-line flux through the study period. Crosson's speedup was strongest in two distinct regions: near eastern Smith Glacier's grounding line and near the eastern (shelf-right) margin of the calving front (Figure 2-2). These two regions suggest that multiple processes may have influenced the speedup, and so we discuss these regions separately.

2.5.2.1 Speedup of the outer shelf

The most notable changes near Crosson's calving front are the loss of the Haynes Glacier tongue and the increased rifting near the eastern margin. The rifts in this area coincide with inferred enhancement from our diagnostic model (Figure 2-5), suggesting that the strength of this area is important to the flow of the shelf. To understand how this rifting may have affected the shelf, we compared the enhancement to Crosson's compressive arch (contour in Figure 2-5).

The spreading side walls of Crosson's embayment result in a transition from compression to extension that is nearly perpendicular to flow, with most changes to enhancement downstream of this transition (Figure 2-5). The overall dynamics of Crosson would have been relatively insensitive to weakening seaward of this transition, but changes landward of this transition would have resulted in broad speedup. Because the weakening on Crosson was primarily just in the tensile area, the effects of the weakening would have been isolated to the freely spreading area downstream of the arch, which is consistent with the observed speedup (Figure 2-2b&c). This weakening is unlikely to have had a widespread effect on the shelf dynamics, but breakup of the

outer shelf exposes the inner shelf to further weakening. This weakening would involve dynamic effects beyond the immediate vicinity of the rifting/damage, possibly causing speedup upstream on the portions of Crosson that remained at nearly constant velocity through the 1990s and 2000s. By contrast, there has been little weakening of Dotson.

The local nature of the speedup on the outer portion of Crosson suggests a local cause (e.g. the breakup of neighboring ice). Loss of resistance at the shelf front can increase calving rates, reducing lateral contact area and initiating speedup (Cassotto et al., 2015). The Haynes Glacier tongue may have provided a small but critical shear resistance on the corner of the shelf, and the gradual loss of this tongue may have allowed a cycle of increasing speedup and weakening of Crosson's eastern corner. The speedup of this area of the shelf began before the 1990s (Lucchitta et al., 1994; Eric Rignot, 2008) and continued through 2009, and the Haynes tongue broke up throughout this same period. However, due to feedbacks between strain heating or rifting and speedup, the observed Crosson weakening may either have caused or been caused by its speedup, and the simultaneous breakup of the Haynes tongue may have been unrelated or a response to the same forcing that weakened Crosson. Utilizing a parameterization of damage (e.g. C. Borstad et al., 2016) in a prognostic model, which would let weakening of the shelf evolve with speedup, could help to identify whether these changes initiated with the breakup of the Haynes tongue or some other forcing.

2.5.2.2 Speedup near the grounding line

Speedup near eastern Smith Glacier's grounding line is most likely associated with loss of basal resistance caused by grounding-line retreat. The grounding line could have been perturbed directly through increased basal melt, either synchronously or asynchronously with the increased melt on Dotson. However, the changes in Crosson's grounding-line position also could be a result of the

ungrounding on Dotson. Thinning of western Smith Glacier would have led to thinning of the eastern branch as well. Such thinning could have led to ungrounding of the trunk of eastern Smith Glacier and thus loss of basal resistance, dynamic thinning, and speedup. Finally, we cannot eliminate the possibility that weakening of the outer shelf resulted in this speedup. Prior work has addressed the effect that thinning (equivalently, weakening) over different portions of Crosson and Dotson would have on ice loss upstream (Daniel N. Goldberg et al., 2016), and the areas in which we find weakening encompass several regions that are important for upstream dynamics. That work suggests that while the overall dynamics are insensitive to the bulk of weakening we find here, weakening in key areas, particularly near the Haynes tongue and at the western shear margin, is important for loss of grounded ice upstream, and thus may have influenced speeds near the grounding line as well. The velocity and thinning signatures of these different causes of retreat could be addressed with a prognostic ice-flow model.

2.5.3 Comparison to previous melt estimates

Despite the limited resolution, the broad spatial and temporal coverage afforded by the methods used here have advantages compared to previous estimates of melt. First, the radar-based methods used by Khazendar et al. (2016) do not directly represent melt but rather anomalous melt under the assumption of no dynamic thinning. Adding the flux divergence recovers the melt rate (Table A-1 and Figure A-1) and yields a different spatial pattern with higher peak melt (187 m/yr). Irrespective of correction for this dynamic component, these estimates are 1-5 year snapshots of melt at single points, and the interannual variability in melt rates in the region (e.g. Dutrieux et al., 2014; Jacobs et al., 2012) prevents extrapolation through time. Average melt rates beneath the shelves cannot be easily obtained from these point measurements, but the polygon-based methods

we use, though limited in spatial resolution, yield average rates beneath large portions of the shelves.

While Gourmelen et. al (2017) are able to compute spatially resolved melt rates beneath all of Dotson, their altimetry-based method has greater sensitivity to certain errors than the methods we employ. The amount of snow on an ice shelf significantly influences surface elevations because the lower-density snow does not hydrostatically depress the shelf as much as an equivalent thickness of ice. Thus, uncertainty in SMB leads to significant uncertainty in thickness changes, particularly because SMB may be inversely correlated with basal melt on seasonal-to-interannual timescales (F. S. Paolo et al., 2018). Moreover, mismeasurement of the surface elevation is increased tenfold in estimating the melt rate using altimetry-based methods, leading to substantial uncertainty. Our method is primarily sensitive to horizontal flux divergence, so it is less sensitive to errors in surface elevation and SMB than the method of Gourmelen et al.

The peak regionally-averaged melt rates found in this study (23 m/yr) occur in the same regions (K1, SW1 and SE1) as found in other studies but the values are lower than the locally computed rates (50 m/yr in Gourmelen et. al (2017) and 129 m/yr in Khazendar et al. (2016)). This difference is not surprising, since the polygon-based method we use has limited spatial resolution and thus misses variations in melt rate in small-scale features such as within the channel on Dotson. Over broad scales, flux-gate and altimetry-based methods should agree, and indeed the overall melt rate we find beneath Dotson, 7.7±1.3 m/yr, agrees with the 6.1±0.7 m/yr found by Gourmelen et al. (2017). The lower peak melt rates found here compared to prior studies may also result from our assuming a spatially constant thinning rate over shelves where thinning rates vary substantially (Gourmelen et al., 2017). The shelf-wide rates used here likely cause us to underestimate melt in small polygons where thinning is most rapid (e.g. K1, SW1, and SE1 in Figure 2-3). Similarly,

they may cause us to slightly overestimate melt over broad, slower-changing regions (e.g., D1 and D2), but this effect should be smaller due to the shelf-wide thinning rate being more representative of rates in these regions. On scales smaller than the polygons we use to calculate melt, thinning may reach 50 m/yr (Gourmelen et al., 2017), comparable to flux divergence in these areas. This thinning may cause the polygon-averaged rates to locally underestimate melt by a factor of two and introduce an error in the polygon average that we estimate may be as high as 50% in small polygons near the grounding line.

2.6 Summary

We used observations of elevation and velocity along with an inverse model to investigate the causes of grounding-line retreat and speedup on Crosson and Dotson ice shelves. These two ice shelves exhibited contrasting responses to changes in forcing, despite comparable grounding-line flux and similar changes in basal melt. Confirming earlier results (J. Mouginot et al., 2014; Eric Rignot, 2008), we find that both ice shelves were out of balance at the beginning of our observational period in 1996. We find that thinning and speedup early in the study period are likely an ongoing response to earlier changes. Similar to previous studies, we show that basal melt rates increased on areas that were floating throughout the study period, and we find that total basal melt was further increased as ungrounding exposed more area to melt. We find that the melt rates, grounding line position, and incised channel geometry on Dotson suggest that it began to retreat in the early 1970s or before. These conditions lead us to speculate that a change in melt, likely resulting from a change in ocean forcing years or decades before 1974, may have led to Dotson's imbalance in 1996. Our results indicate that Dotson's grounding-line retreat and thinning exposed more sub-shelf area, increasing its sensitivity to ocean forcing and likely contributing to the high melt rates that we and others find during the 2000s. Prior work has shown that Crosson sped up

through our study period, primarily near eastern Smith Glacier's grounding line and near the former tongue of Haynes glacier. We used a diagnostic ice-flow model to show that this speedup was likely the result of multiple factors, including weakening at its eastern margin and a retreat of eastern Smith Glacier's grounding line. Determining the initial cause of change to this system is key to understanding whether the present retreat results from ongoing oceanic or climatic changes, natural variability, or internal instability, and thus important for placing these observations in the context of other changes to submarine basins around Antarctica. In the future, prognostic modeling of this system beginning in 1996 or before (i.e. "hindcasting"), could help test how different initial perturbations to the system would have affected its flow speed and mass balance, and thus provide context to these changes relative to those observed in other glaciers.

Acknowledgements. This work was supported by NASA. D. Lilien and D. Shean were supported through the NASA Earth and Space Science Fellowship (NESSF) Program (NNX15AN53H and NNX12AN36H). I. Joughin was supported by NNX17AG54G, and B. Smith by NNX13AP96G. Computing resources for ice-flow modeling and for WorldView/GeoEye DEM processing were provided by the NASA High-End Computing (HEC) Program through the NASA Advanced Supercomputing (NAS) Division at Ames Research Center. RACMO2.3 SMB data were provided by J.M. van Wessem (Utrecht University). F. Paolo (JPL) provided thinning rates over the ice shelves.

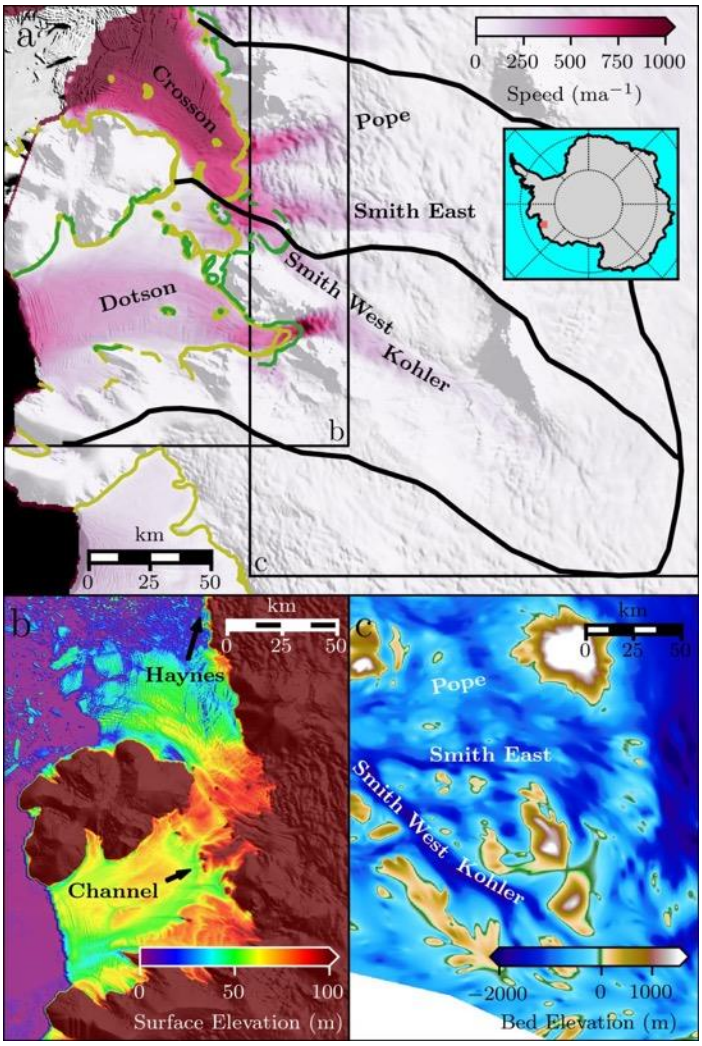

Figure 2-1: Overview of study area.

a. 1996 surface speed overlaid on the mosaic of Antarctica (MOA) (Haran et al., 2013). Yellow and green lines show grounding line positions in 1996 and 2011 respectively (E. Rignot et al., 2014). Black lines indicate catchment boundaries of Crosson and Dotson used for flux calculations. **b.** Surface elevation relative to the EGM2008 geoid from WorldView/GeoEye stereo DEM mosaic (D. E. Shean et al., 2016). **c)** Ice bottom elevation relative to the EGM2008 geoid, which represents bed elevation over grounded ice.

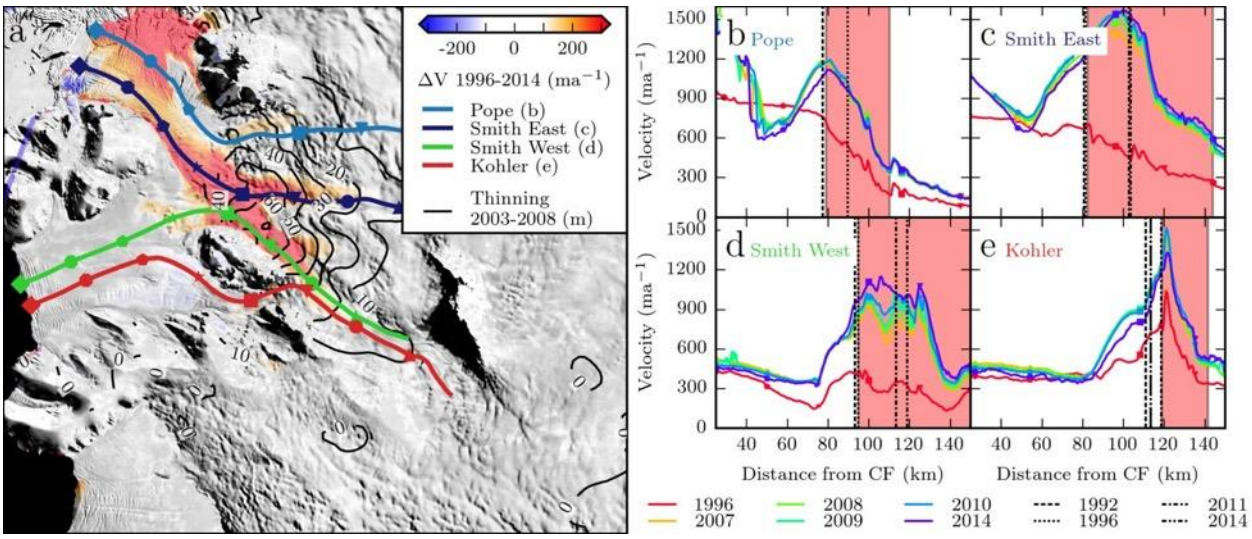

Figure 2-2: Recent changes in velocity and surface elevation.

a. Color shows change in speed from 1996 to 2014. Contours indicate thinning of grounded ice from 2003-2008 at 10-m intervals, derived from OIB altimetry, ICESat-1 and WorldView/GeoEye DEMs. Colored lines indicate flowlines plotted in panels (b - e). Background is MOA. **b – e.** Velocity profiles as distance from the 2014 calving front (CF). Dashed lines indicate grounding line positions in different years. Red shading indicates areas that thinned by more than 5 m a^{-1} from 2003-2008.

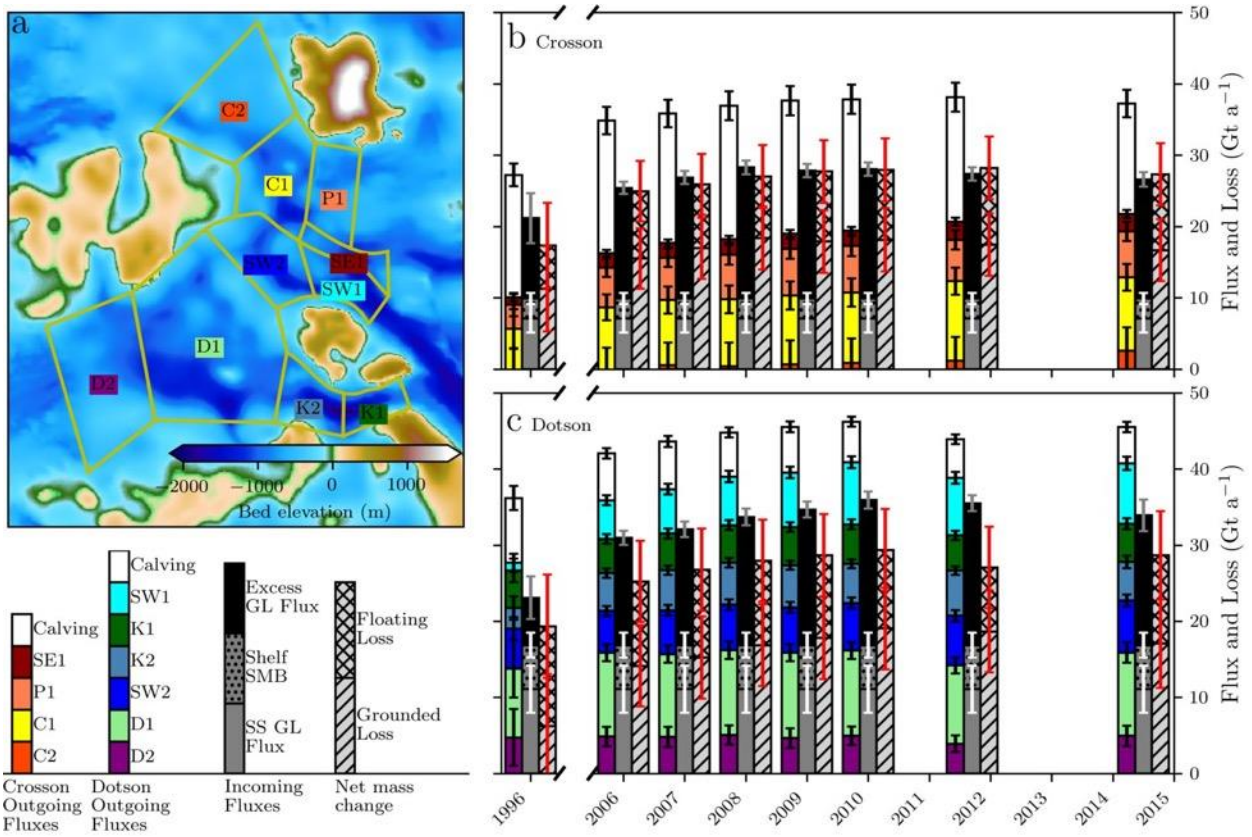

Figure 2-3: Flux and melt changes over Crosson and Dotson.

a. Areas used for flux divergence calculations, outlined in yellow, plotted over bathymetry from Millan et al., (2017). **b.** and **c.** Flux and melt over Crosson and Dotson respectively. Stacked, colored bars show melt over each of the polygons from (a) while white bars on top show calving flux; these bars sum to the total outgoing flux. Solid gray bars show the steady-state (SS) grounding line (GL) flux (calculated from catchment-wide SMB), the dotted gray bars show the SMB over the shelves, and the solid black bar indicates the additional flux crossing the grounding line each year due to dynamic imbalance; these bars total to all incoming flux to the shelves. Light gray slashed bars indicate the loss of grounded ice (equal to the black bars in the previous column) and the cross-hatched light grey region shows the additional loss of floating ice (equal to the difference between the first two columns); these total to the annual mass loss rates.

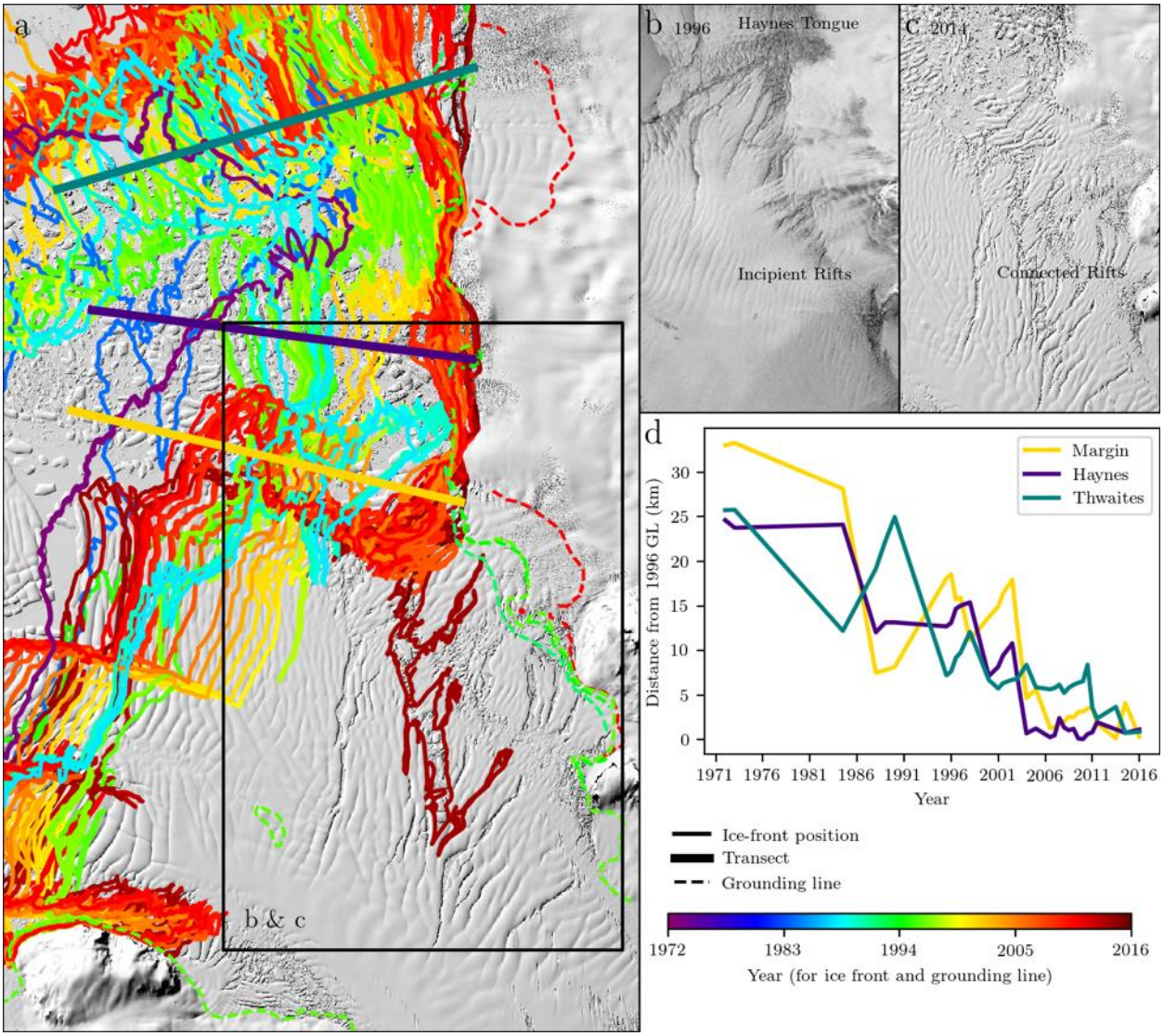

Figure 2-4: Crosson Ice Shelf front position.

a. Selection of digitized shelf-front positions from MacGregor et al. (2012) and from our work, with grounding lines from Rignot et al. (2014). Teal, purple, and gold overlays correspond to transects used for (d). Box shows the outline of zoomed in area for (b) and (c). **b-c.** Zoomed in Landsat imagery from 1996 and 2014 respectively. Isolated rifts in 1996 appear connected by 2014, effectively detaching Crosson from its eastern margin. The disintegration of the Haynes Glacier Tongue also occurred during this period. **d.** Time series of ice-shelf-front distance relative to the 1996 grounding line.

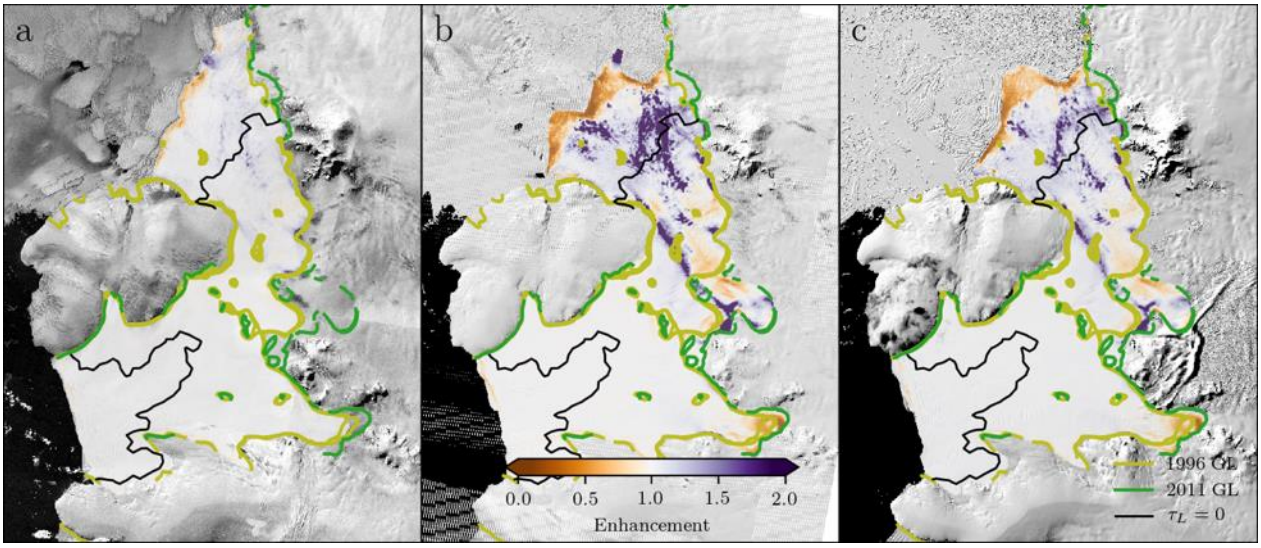

Figure 2-5: Inferred enhancement to ice flow.

a. 1996, **b.** 2010, and **c.** 2014. The enhancement factor gives the depth-averaged weakening of the ice relative to that predicted by a temperature model, with values larger than 1.0 indicating weakening. Black line indicates the zero contour of τ_L in 1996, i.e. the boundary between the compressive (upstream) and extensional (seaward) regimes. Backgrounds are Landsat images from the same year as the inversion.

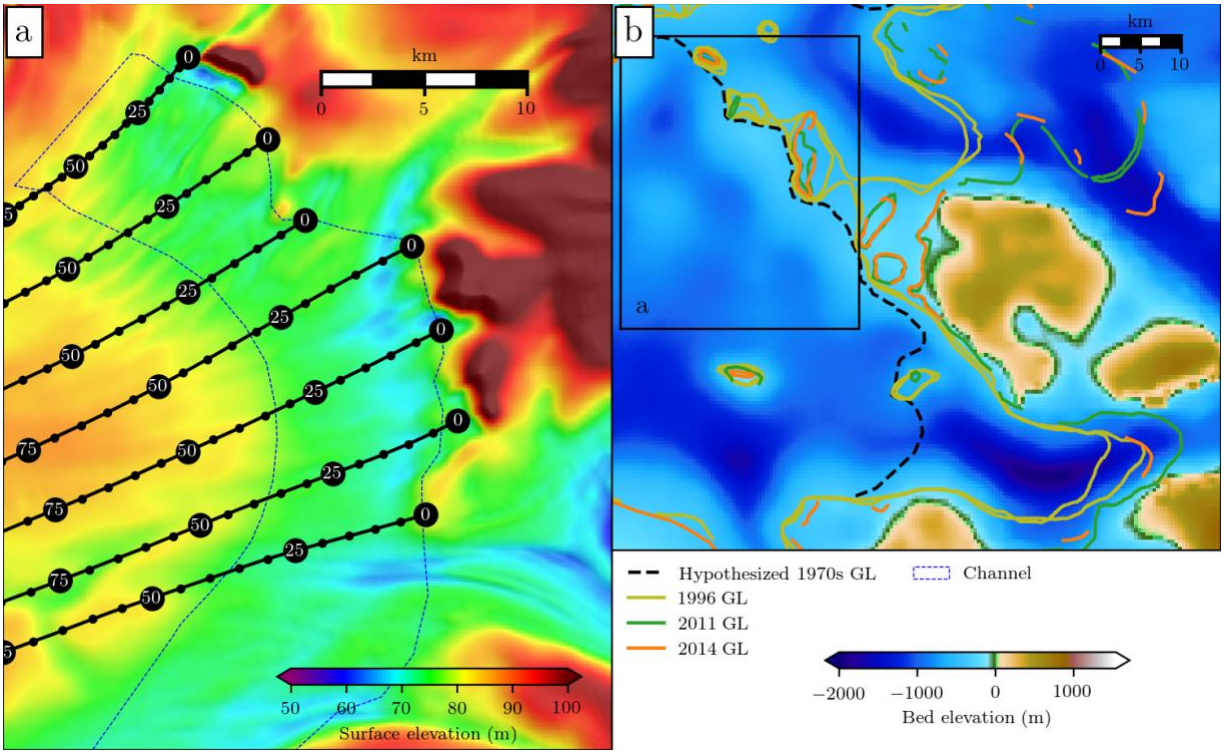

Figure 2-6: Evidence for pre-satellite retreat of Dotson.

a. Detail of Dotson surface trough (region outlined in blue). Solid black lines show flowlines calculated from the 1996 velocity, with dots placed every 5 years. Large black circles are spaced every 25 years and labeled with age in years. Background is 2012 surface elevation. **b.** A possible location of the grounding line before recent retreat (black dashed line). This position is illustrative only, but shows a location that would have been susceptible to a retreat that would have increased melt rates and grounding line flux. Other lines show grounding line positions as above. Black box shows location of panel (a). Background is bathymetry (Millan et al., 2017).

	Grounding-Line Flux			Calving Flux			Basal Melt Rate			Volume Change		
		(R13)	(D13)		(R13)	(D13)		(R13)	(D13)		(R13)	(D13)
Crosson	25±1	27.4±2	--	18±2	12±2	--	19±3	38.5±3	--	-9±2	-19±1	--
Dotson	30±1	28.4±3	--	5±1	6±1	--	41±2	45.2±3	--	-11±3	-17±2	--
Total	55±2	55±5	51±5	25±3	17±3	18±2	60±5	83.7±6	78±7	-20±4	-36±3	-36±3

Table 2-1: Comparison of fluxes and melt between this study and prior work.

This study is in white columns and those from *Rignot et al.* (2013) (R13) and *Depoorter et al.* (2013) (D13) are in gray. Values from this study are for 2010, while the *Depoorter et. al.* values are for 2009, and the *Rignot et al.* values are for 2007-2008. Columns show grounding-line flux, calving flux, basal melt rate, and volume change. All values are given in gigatons per year (Gt a^{-1}).

Chapter 3 Melt at grounding line controls observed and future retreat of Smith, Pope, and Kohler glaciers

Abstract. Smith, Pope, and Kohler Glaciers and the corresponding Crosson and Dotson Ice Shelves have undergone speedup, thinning, and rapid grounding-line retreat in recent years, leaving them in a state likely conducive to future retreat. We conducted a suite of numerical model simulations of these glaciers and compared the results to observations to determine the processes controlling their recent evolution. The model simulations indicate that the state of these glaciers in the 1990s was not inherently unstable, i.e. that small perturbations to the grounding line would not necessarily have caused the large retreat that has been observed. Instead, sustained, elevated melt at the grounding line was needed to cause the observed retreat. Weakening of the margins of Crosson Ice Shelf may have hastened the onset of grounding-line retreat but is unlikely to have initiated these rapid changes without an accompanying increase in melt. In the simulations that most closely match the observed thinning, speedup, and retreat, modeled grounding-line retreat and ice loss continue unabated throughout the 21st century, and subsequent retreat along Smith Glacier's trough appears likely. Given the rapid progression of grounding-line retreat in the model simulations, thinning associated with the retreat of Smith Glacier may reach the ice divide and undermine a portion of the Thwaites catchment as quickly as changes initiated at Thwaites' terminus.

3.1 Introduction

Glaciers along the Amundsen Sea Embayment (ASE) have long been thought to be vulnerable to catastrophic retreat (Hughes, 1981), and the major ice streams in the region have recently undergone significant speedup and grounding-line retreat (J. Mouginot et al., 2014; E. Rignot et al., 2014; Scheuchl et al., 2016). Largely due to synchronicity between variability in ocean

temperature and glacier response, ocean-induced melting is thought to be the primary driver of these changes (Jenkins et al., 2010; I. R. Joughin et al., 2012). Oceanographic observations (Assmann et al., 2013) and modeling (Thoma et al., 2008) indicate that variable transport of warm circumpolar deep water (CDW) onto the continental shelf has caused significant variability in sub-shelf melt over the past two decades, with melt thought to have peaked around 2010 (Jenkins et al., 2018). Melt rates influence the large-scale flow of ice streams by affecting ice-shelf thickness; thinner ice shelves provide less buttressing to ice upstream, and ice is forced to flow faster to increase strain-rate dependent stresses in the ice. Ice-flow modeling (e.g., I. R. Joughin et al., 2014) and glaciological observations (e.g., E. Rignot et al., 2014) suggest that retreat of Thwaites and perhaps Pine Island Glacier, the largest along the ASE, will continue under all realistic melt scenarios (Favier et al., 2014; I. Joughin et al., 2010).

Despite their lower ice discharge relative to Thwaites and Pine Island Glaciers, Smith, Pope and Kohler Glaciers (see Figure 3-1 for an overview of the area) have gained attention as some of the most rapidly changing outlets along the Amundsen Sea Embayment (J. Mouginot et al., 2014). These glaciers, and the associated Crosson and Dotson Ice Shelves, have undergone >30 km of grounding-line retreat in recent decades (E. Rignot et al., 2014; Scheuchl et al., 2016), leaving their grounding lines positioned more than 1 km below sea level, where they are vulnerable to warm ocean waters (Jenkins et al., 2018; Thoma et al., 2008). By contrast, the Thwaites grounding line sits approximately 50 km downstream of the deepest portions of its basin (E. Rignot et al., 2014) and the Pine Island grounding line has remained stable on the retrograde slope at the seaward end of its overdeepening from 2009-2015 (I. Joughin et al., 2016). Thus, the positioning of Smith Glacier's grounding line in the deep portion of its trough suggests that it is in a more advanced stage of retreat than its larger neighbors. Indeed, Smith Glacier comprises one of the most

extensive instances of modern glacier retreat and can serve as an important example of a marine ice-sheet basin in an advanced state of collapse.

Modeling of the grounded portion of the Smith, Pope, Kohler catchment indicates that further retreat is committed on decadal timescales (D. N. Goldberg et al., 2015). However, this modeling was focused on transient calibration and did not assess causes of retreat or examine likely changes over periods longer than 30 years. Additional modeling work shows that the ice-shelf response is highly sensitive to the sub-shelf melt rates, which, when determined from an ocean model, are in turn highly dependent on how well the bathymetry is resolved (D. N. Goldberg et al., 2018). Regardless of the initial cause of retreat, the ice shelves are unsustainable at present melt rates, and Dotson Ice Shelf may melt through in the next 50 years (Gourmelen et al., 2017). The ice presently within the Smith, Pope, Kohler drainage could raise global mean sea level by a relatively modest 6 cm (Fretwell et al., 2012), but thinning can lead to drainage capture and therefore increased loss of ice volume. Thus, due to a shared divide, rapid thinning could potentially hasten the collapse of the larger reservoir of ice in the neighboring Thwaites catchment.

Although there is evidence of increased transport of warm ocean waters beneath these ice shelves, the complex nature of ice-sheet dynamics involves the responses to past and present forcing. Present observations represent a combination of adjustment to past imbalance and response to recent melt (e.g., Jenkins et al., 2018). In the case of Smith, Pope, and Kohler Glaciers, multiple lines of evidence suggest that retreat began before widespread satellite observations (Gourmelen et al., 2017; Konrad et al., 2017; Lilien, Joughin, et al., 2018), though the exact cause and timing of retreat initiation are unknown. Separating the effects of different forcings is key to understanding the extent to which continued forcing is required to sustain retreat. Since future forcing is uncertain, identifying whether retreat is inevitable within the expected range of ocean

warming is particularly valuable. Because of the short length of the satellite record, separating the compounded influence of the possible drivers of retreat is difficult with observations alone, and numerical ice-flow models are an important tool for identifying plausible scenarios that could have resulted in the observed changes to ice thickness, velocity, and grounding-line position.

Here, we describe a suite of model simulations designed to investigate which processes control the ongoing retreat of Smith, Pope, and Kohler Glaciers. Our modeling experiments tested the effects of melt distribution, melt intensity, basal resistance, and marginal buttressing on speedup, thinning, and grounding-line position. We compared these modeled changes to remotely sensed observations in order to determine which processes have driven retreat over the last two decades. After comparing the modeled velocity, surface elevation, and grounding-line position to observations, we ran a subset of the simulations for a longer duration to investigate the sensitivity of the future evolution of this system to a range of forcing.

Simulations of Antarctic ice streams generally require a melt forcing to determine the mass balance of the bottom of the ice shelves. Spatially resolved sub-shelf melt rates have only recently been measured for ice shelves in the ASE (Gourmelen et al., 2017; D. E. Shean et al., 2017), and these observations are limited by their brief record and low temporal resolution. Thus, use of these high-resolution melt rates as inputs to prognostic ice-flow models that extend further into the past or into the future requires extrapolation. To avoid such extrapolation, models are usually forced with simple, often solely depth-dependent, parameterizations of melt (e.g., Favier et al., 2014; I. Joughin et al., 2010). Significant progress has been made in coupling state-of-the-art ice and ocean models (e.g., De Rydt & Gudmundsson, 2016; Jordan et al., 2018), though to our knowledge only one study has applied a fully coupled model with moving grounding line to the geometry of a real glacier (H. Seroussi et al., 2017). Coupled simulations capture spatial and temporal variability in

melt rates but require substantial high-performance computing resources. Moreover, modeled sub-shelf melt rates are highly sensitive to the sub-shelf bathymetry (D. N. Goldberg et al., 2018), which is difficult to measure or infer due to the ice and ocean cover. Because these coupled ice-ocean models require additional development and substantial high-performance computing resources, and are sensitive to uncertain bathymetry, they are not yet readily available for assessing sensitivity to a suite of forcings.

While ocean forcing is thought to be the primary driver of retreat along the ASE, a glacier's sensitivity to sub-shelf melt is modulated by additional processes. Grounding-line retreat exposes additional and, for a retrograde bed, deeper sub-shelf area to melt, potentially increasing the integrated melt rate without any change in ocean heat content (De Rydt et al., 2014). Additionally, ungrounding on a retrograde bed causes ice-flow speeds to increase due to the nonlinear dependence of ice velocity on ice thickness. These feedbacks cause some grounding-line positions to be inherently unstable, such that upstream perturbations to those grounding-line positions can lead to self-sustaining retreat (e.g., Christian Schoof, 2007). Changes to the effective viscosity of ice shelves, such as weakening from mechanical damage, fabric development, or higher ice temperatures, can reduce the shelf's ability to transmit stresses and thus reduce buttressing in the same manner as a decrease in the shelf's cross sectional area (e.g., C. Borstad et al., 2016). Observations (Macgregor et al., 2012) and inverse modeling (Lilien, Joughin, et al., 2018) suggest that changes to viscosity have indeed played a role in the speedup of Crosson Ice Shelf, and a modeling sensitivity study suggests that weakening of several key regions of the ice shelves would significantly alter ice discharge (Daniel N. Goldberg et al., 2016). While some other processes, such as loss of terminal buttressing due to retreat of the neighboring Haynes Glacier, may have destabilized Crosson Ice Shelf, changes to melt, marginal weakening, and feedbacks between

ungrounding and increased ice-flow speeds represent the most likely drivers of retreat in this system.

3.2 Methods

We conducted a suite of prognostic numerical model simulations of Smith, Pope, and Kohler Glaciers, primarily using a shallow-shelf (SSA) model implemented in the finite element software package Elmer/Ice (Olivier Gagliardini et al., 2013; Zwinger et al., 2007). The shallow-shelf equations describe ice flow in two dimensions under the assumptions that the ice is thin relative to its extent and that ice velocity is uniform with depth (i.e., the model is depth-averaged); while a simplification, these assumptions are generally applicable to ice streams (MacAyeal, 1989) and have been applied to other glaciers in the ASE (e.g., Favier et al., 2014; I. R. Joughin et al., 2014). To validate the use of these simplified ice physics, we performed one simulation using a state-of-the-art full-Stokes (FS) ice-flow model, also implemented in Elmer/Ice. In slower flowing regions where our inversion results show that internal deformation comprises a significant portion of motion, incorporating the variation of velocity with depth may be important. The full-Stokes simulation allows to identify potential drawbacks of applying the simplified shallow-shelf model to this particular system of glaciers.

3.2.1 Model setup

The model domain extended from the ice divide (determined from the measured velocity field) to the 1996 calving front. For the majority of simulations, the horizontal mesh resolution was 300 m near the grounding line and 3 km elsewhere. The full-Stokes domain was extruded to 9 vertical layers, with 5 layers concentrated in the bottom third of the ice, giving an effective resolution of 20 to 500 m depending on ice thickness and depth within the ice column. This resolution is generally considered sufficient to accurately capture grounding-line dynamics (Pattyn et al., 2013),

and sensitivity to mesh resolution is explored further in Appendix B.2.1. The upper ice surface at initialization was found by adjusting a high-quality reference digital elevation model (DEM) mosaic, derived from WorldView/GeoEye stereo imagery, to match expected conditions in 1996. This adjustment used thinning rates found from ICESat-1, the Airborne Topographic Mapper from NASA's Operation IceBridge, and WorldView/GeoEye stereo DEMs (further description of the determination of this surface can be found in Lilien, Joughin, et al., 2018). The bed elevations were determined from all publicly available airborne radio echo sounding data, anisotropically interpolated to 1-km posting so as to weight measurements along flow more heavily than those across flow; details can be found in Medley et al. (2014) and the supplementary materials to Joughin et al. (2014). The advantage to this method of interpolation is that it is free of assumptions related to a particular state of mass balance, unlike mass conservation methods. The lower ice surface was then determined using those bed elevations beneath grounded ice and an assumption of hydrostatic equilibrium downstream of the 1996 grounding line. Firn-air content for the hydrostatic calculation was found by comparing coincident ice-thickness and surface-elevation measurements over the ice shelves (supplementary materials of Lilien, Joughin, et al., 2018).

All model simulations were initialized to best match the transient state of these ice streams in 1996, the earliest year with relatively complete maps of ice velocity in this area. The velocity measurements were acquired by the European Remote-Sensing Satellites (ERS-1 and 2) and processed using a combination of interferometry and speckle tracking (I. R. Joughin, 2002). Model initialization consisted of an iterative process using a full-Stokes, diagnostic thermomechanical model in Elmer/Ice. We iterated between updating the temperature field and using inverse procedures to infer the basal shear stress of grounded ice and the enhancement factors over floating ice. These inferred fields minimized the misfit between modeled velocity

and the measurements from 1996. In order to minimize transient effects of data errors while capturing the real transient state of these ice streams in 1996, the model was briefly relaxed by running forward in time for one year under constant forcing. Then, the inversions were repeated to infer the final inputs for the forward model. Further details of inversion procedures, temperature initialization, and relaxation are provided in Appendix B.

3.2.2 Prognostic simulations

We ran suite of more than 20 ice-flow model simulations for at least 23 years, all beginning in model-year 1996. These relatively brief simulations enabled comparison with observations, and 6 of these simulations were subsequently run over 100 years to investigate likely future evolution of these glaciers; those 6 simulations were selected after the full suite of shorter runs and were chosen to represent a range of retreat rates. Table 3-1 summarizes the inputs for all model runs, indicating the model physics, run length, melt distribution and intensity, and any other forcing as described below. In all model simulations, time stepping used a backwards-difference formula with timestep size of 0.05 years.

Most of the model simulations used a Coulomb-type sliding law proposed by Schoof (2005) and Gagliardini et al. (2007), which takes the form

$$\tau_b = CN\left(\frac{\chi u_b^{-m}}{1+\chi}\right)^{\frac{1}{m}} u_b \qquad \text{Equation 1}$$

where τ_b is the basal shear stress, u_b the basal velocity, N the effective pressure, C proportional to the maximum bed slope, m the sliding law exponent, and $\chi = \frac{u_b}{C^m N^m A_c}$, where A_c is a coefficient that is determined using the inversion results. This sliding law was derived to represent sliding

over a rigid bed with cavitation behind obstacles, but its high- and low-pressure limits make it suitable for describing Antarctic ice streams. At high effective pressure, generally found in slow-flowing regions that may be underlain by hard beds, the sliding law approximates Weertman (1957) sliding ($\tau_b \propto \mathrm{u_b^m}$). At low effective pressures, this Equation 1 approaches Coulomb-type sliding ($\tau_b \propto CN$), which is thought to be appropriate for sliding over soft beds (e.g., Iverson et al., 1998; Tulaczyk et al., 2000) and hard beds where fast-sliding with cavitation takes place (C. Schoof, 2005). We take $m = 3$, and assume that the effective pressure is equal to the ice overburden minus the hydrostatic pressure. This assumption is valid if a drainage system connects every point on the glacier bed to the ocean, which is only likely for areas near the grounding line. However, this assumption is often employed (e.g., Morlighem et al., 2010), and because coupling to a hydrologic model is beyond the scope of this study, we retain the assumption here. To some extent, errors in the assumption compensated for in the solution or the sliding coefficient, C, though it may introduce errors as the basal shear stress is reduced too drastically in response to inland thinning. For comparison, we ran four additional simulations with a commonly used Weertman-type sliding law ($\tau_b = \mathrm{A_w u_b^m}$), with $\mathrm{A_w}$ calculated from the same inversion results, again with $m = 3$.

3.2.2.1 Melt sensitivity experiments

We explored the effect of a variety of plausible melt forcings on the evolution of Smith, Pope, and Kohler Glaciers. The forcings can be separated into melt intensity (i.e. shelf-integrated melt) and its spatial distribution; simulations were conducted varying the melt intensity and distribution independently to determine their relative importance in controlling retreat. Because of their low computational expense, we used simple prescriptions of melt: three depth-dependent parameterizations (Favier et al., 2014; I. Joughin et al., 2010; D. Shean, 2016), all tuned to fit the

melt-depth relationship of nearby Pine Island Glacier, and an interpolation from previously published high-resolution melt-rate estimates inferred from Cryosat-2 by assuming hydrostatic equilibrium (Gourmelen et al., 2017), which was extended to cover both ice shelves. Hereafter, we refer to these melt distributions as F2014, J2010, S2016, and Cryo2, respectively. The parameterizations are intended to span a reasonable range of likely melt distributions, and none of them were expected to match the Cryosat-inferred pattern of melt exactly. Any depth-dependent parameterization will fail the span of melt rates observed at a given depth. However, the depth-dependent parameterizations capture the general form of the Cryo2-inferred melt rates, despite not having been tuned to Crosson and Dotson Ice Shelves (Figure 3-2).

Melt rates inferred from Cryosat 2 are limited to areas that were floating during the period of 2010-2016, which potentially complicates forcing the model with the Cryo2 distribution. If additional area beyond what was afloat in 2016 were to unground in a model simulation, some extrapolation is needed to apply a melt forcing to that area. Fortuitously, modeled grounding-line retreat rates with the Cryo2 melt forcing were low, and these simulations did not generally require extrapolating the Cryosat-inferred melt distribution. For the minor extrapolation that was necessitated, we first smoothed the melt rates to 2-km resolution then used nearest-neighbor interpolation to extend the rates inland. However, during the first 25 years of the model simulations no extrapolation was required, so the limited extent of the inferred melt rates does not affect comparison modeled and observed retreat.

During each timestep from model years 1996-2014, each melt distribution was scaled to match the shelf-total melt rate. Note that this scheme differs from prior studies (Favier et al., 2014; I. Joughin et al., 2010; I. R. Joughin et al., 2014) that instead fix the parameterization for a particular run and accept temporal variation in melt rate as the depth of shelf's underside evolves; comparative

advantages and disadvantages of our approach are discussed in section 3.4.2.2 . The melt intensity was determined by linear interpolation between available measurements of shelf-total melt obtained from flux divergence measurements through time (Lilien, Joughin, et al., 2018). In general, this scheme requires adjusting the depth-dependent parameterizations down from the "1x" versions by a factor of 4-5, and the Cryo2 rates down by 20%, in order to match the relatively low melt rates 1996; such scaling is unsurprising given the large differences between the Dotson and Crosson cavities and the Pine Island Glacier cavity for which the parameterizations were originally tuned. Through the simulations, the scaling factor for melt was generally increased to force the observed increases in melt. For the depth-dependent parameterizations, this increase was compounded by the need to compensate for the rapid decrease of ice-shelf draft due to intense melt at depth, which can result in the shelves "shallowing out" of high melt rates over most of their area. Thus, the scaling through time varied significantly based upon how quickly the ice-shelf draft shallowed and how much new area became exposed to the ocean and contributed to the shelf-total melt rate. After 2014, when melt-rate estimates are no longer available, the scaling was fixed to the value determined for 2014 and the total melt rate was allowed to vary as in previous studies. For partially floating elements, melt was applied only over the floating portion, and the model resolution employed avoided significant sensitivity to this choice (Hélène Seroussi & Morlighem, 2018).

We also conducted simulations changing melt intensity to twice that observed (simulations 3, 11, 18, and 25 in Table 3-1). To vary the melt intensity, we again rescaled the parameterization at every timestep through 2014 in order to force the total melt rate to match twice the observations. To distinguish these from what previous authors refer to as "1x", "2x", and "4x", we instead refer to the different intensities as "1Obs" and "2Obs". It is important to note that in the prior studies,

"Nx" referred to scaling of the parameters, which, due to shallowing of the ice-shelf draft, could lead to substantially less melt than N times the observations. During the period of observations, 2Obs actually doubled the shelf-wide integrated melt.

3.2.2.2 Marginal weakening experiments

We manually masked the areas within 10 km of the edge of Crosson and Dotson Ice Shelves and applied an ad-hoc change to the depth-averaged enhancement factor over these areas to test the model's sensitivity to marginal weakening. These runs were conducted using the shallow-shelf model and used an enhancement factor of 4 (a 44% reduction in B) to weaken the margins. These weakening experiments were done with all four melt distributions at 1Obs melt intensity. One additional simulation was run with an enhancement factor of 1.8 (a 17% reduction in B) using the J2010 melt parameterization at 1Obs intensity (simulation 5 in Table 3-1). In order to test the effect of marginal weakening in the absence of any increase in melt, an additional set of simulations were conducted fixing the melt parameterization to its 1996 scaling and applying the enhancement factor of 4; these simulations again used each of the four melt distributions at 1Obs intensity (simulations 4, 12, 19, and 26 in Table 3-1). We refer to these experiments with weakened margins but fixed melt parameterization as "control melt" simulations (simulations 6, 13, 20, and 27 in Table 3-1).

3.2.2.3 Forced ungrounding experiments

Since model simulations cannot be expected to perfectly replicate observed grounding-line retreat, we ran an additional suite of experiments to test the effect of the ungrounding itself on thinning and speedup. These simulations allow us to assess whether feedbacks between ungrounding, thinning, and speedup may have caused the observed retreat, and to separate errors in modeled grounding-line retreat rates from their effects on ice-flow speed and thinning. To estimate the grounding-line position at times between the three available measurements (1996, 2011, and

2014), we linearly interpolated the time of ungrounding along a suite of flowlines spaced approximately every kilometer across flow, creating maps of the grounded area every 0.1 years. At each model timestep through a forcing period (1996-2001 or 1996-2014 depending on the simulation), the grounding-line position was set to match the nearest grounding map, without changing the ice geometry, (i.e. the basal shear stress was set to zero and melt was applied under ungrounded area). We only forced retreat and not the re-advance of Kohler between 2011 and 2014 since forcing re-advance is complicated by the changing geometry after the ice goes afloat. After the period of forced ungrounding finished, the grounding line was allowed to retreat freely based upon hydrostatic equilibrium. Simulations were conducted with all four melt distributions at 1Obs intensity and with both 5 and 18 years of forced ungrounding (simulations 7-8, 14-15, 21-22, 28-29 in Table 3-1).

3.3 Results

Model outputs are composed of the spatio-temporal evolution of a number of variables, notably ice velocity, ice thickness, and grounding-line position. To distill this many-dimensional output into a manageable format, we focus on comparing the changes to grounding-line position and ice-surface speeds along the centerlines of the three main outlet glaciers under various forcings.

3.3.1 Melt variability

Figure 3-3 shows the results of the eight experiments designed to evaluate the melt intensity and distribution (experiments 1-3, 10-11, 17-18, and 24-25 in Table 3-1). Collectively, the results show that grounding-line position and the pattern of thinning are highly sensitivity to the spatial distribution of melt. For the 1Obs experiments, there was <10 km of grounding-line retreat in the shallow-shelf simulations, and the retreat that does occur happens after model year 25. Amongst the 1Obs shallow-shelf simulations, only the one with J2010 melt shows more than 2 km of retreat,

during which time Smith Glacier's grounding line retreated by ~9 km. The full-Stokes simulation with 1Obs, however, shows substantial (30 km) retreat along Smith Glacier during that time, in relatively good agreement with the observations.

Over the first 25 years, retreat in the shallow-shelf models is generally confined to simulations with the 2Obs melt forcing and is greatest with parameterizations that concentrate melt at depth. While the timing of retreat onset varies with melt forcing, the 2Obs parameterizations generally yield similar retreat along Smith and Kohler glaciers. An exception is the Cryo2 melt, which consistently produces the least retreat. For Pope, the 2Obs extent of the retreat varies greatly with melt distribution, ranging from 0 to 18 km compared the observed 5-km retreat. Along Smith and Kohler glaciers, both of which had deep (800-1000 m.b.s.l.) grounding lines in 1996, melt distributions with greater rates at depth tend to cause faster retreat (Figure 3-3b-d). With the 2Obs melt, the simulations using the three depth-dependent parameterizations quickly retreat into similar positions along Smith and Kohler Glaciers (see observed change from 1996 to 20011 in Figure 3-3f). Along Smith and Kohler Glaciers, simulations with the J2010 distribution retreat most rapidly, followed by S2016, F2014, and Cryo2. Melt rates near the grounding line need to reach some threshold before retreat commences; in the shallow-shelf model of Smith Glacier, retreat of the grounding line does not begin unless melt rates of ~100 m a^{-1} or higher are reached near the grounding line. Retreat commences more easily in the full-Stokes model, requiring only ~50 m a^{-1} of melt. The grounding-line retreat rate of Pope Glacier, which had a slightly shallower (~750 m.b.s.l.) grounding line, has a less direct relationship with melt distribution. While retreat initiates most quickly with the J2010 parameterization, it is eventually overtaken by retreat with the S2016 and F2014 parameterizations (Figure 3-3c).

3.3.2 Marginal weakening

We ran nine simulations with weakened margins, and all displayed notable differences in grounding-line position and speedup compared to the simulations with no weakening. Figure 3-4 shows the effects of weakening on grounding-line retreat and ice-flow speedup. The grounding-line position of Smith and Pope Glaciers are sensitive to the shelf viscosity. With the J2010 melt parameterization, the retreat for Smith Glacier initiates ~10 years sooner with enhancement of 4 in the margins (Figure 3-4a-b). While this lag can lead to substantial differences in grounding-line position at any given time, the simulations with full-strength margins generally continue to retreat and reach that same state 10 years later. The notable exception is the simulation with the S2016 melt, which shows >10 km more grounding-line retreat when the margins are weakened (Figure 3-4a). Kohler Glacier's grounding line also retreats sooner with enhanced margins, but as retreat progresses grounding-line position does not differ by more than ~2 km from the unweakened case (Figure 3-4c). In the case of the S2016, F2014, and Cryo2 melt forcings, within 50 years, weakening of the margins causes grounding-line retreat on Pope and Kohler glaciers that did not take place even in 100 years without marginal weakening (Figure 3-4a and c). Simulations with enhancement of 1.8 display approximately half as much change in the timing of retreat as an enhancement of 4 does (not shown). Effects of marginal strength on ice speeds differ markedly between the two ice shelves; Crosson/ Pope flows almost 50% faster in some regions (Figure 3-4d-e) when the margins are weakened while Dotson/Kohler is nearly insensitive to the strength of the margins (Figure 3-4f).

Although some of the simulations with weakened margins show more retreat, these simulations all are forced using the 1Obs melt intensity and thus incorporate the increases in melt observed between 1996 and 2014. In the "control melt" simulations with weakening but with the melt

parameterization fixed at 1996 values, there is only minor grounding-line retreat over the 50-year duration of the simulations (Figure 3-4a-c). If the weakening alone were sufficient to cause grounding-line retreat, we would expect to have seen retreat in these simulations.

3.3.3 Forced ungrounding

Figure 3-5 shows the results of the simulations in which the grounding line was forced to migrate at the rate observed. The forced ungrounding had differing effects depending on the melt distribution, and in some cases no subsequent grounding-line retreat ensued after the period of imposed ungrounding. For Smith Glacier, the effect of exposing additional area to melt and decreasing basal resistance results in significant speedup near the grounding line that continued over 25 years even when only 5 years' retreat was forced. Ice-flow speeds on Pope and Kohler glaciers are relatively unaffected by the forced 5-year grounding-line retreat, but when forced through 2014 (18 years) they display some speedup as well (Figure 3-5d and f). In simulations with the 5-year forced ungrounding, the grounding line is able to stabilize temporarily (Figure 3-5a-c), though retreat subsequently ensues on Smith Glacier for the melt distributions that concentrate melt at depth (J2010, S2016). For the 18-year forced-ungrounding simulations, however, little grounding-line retreat occurs in the subsequent 25 years, and by the end of the 50-year simulations the grounding-line positions using all four simulations approximate the retreated position found with the J2010 1Obs melt and a freely evolving grounding line.

3.3.4 Longer term simulations

Figure 3-6 shows the evolution of the ice volume and grounding-line position for the centennial-scale simulations, displaying sustained loss of ice volume through 2100 CE. These six simulations (simulations 2, 4, 10, 17, 19, 24 in Table 3-1) were simply extensions of model runs mentioned above; four used the different melt distributions at 1Obs intensity and no marginal weakening

while two used the J2010 and S2016 melt distribution at 1Obs intensity with marginal weakening. Simulations with marginal weakening and/or the J2010 melt parameterization show continuing grounding-line retreat throughout the simulation (Figure 3-6). In simulations with significant retreat, the grounding line of Smith Glacier eventually extends upstream of Kohler, and the grounding lines of these two glaciers merge. Even in these simulations with the most retreat, melt rates remain below 75 Gt a^{-1} (within 25% of 2014 levels) for most of the 21st century before gradually increasing to 120 Gt a^{-1} between 2080 and 2100, as more deep ice is exposed to melt. Even with these relatively modest melt rates, the overall contribution to sea-level rise ranges from 6–to–10 mm by 2100 and Smith Glacier's grounding line retreats by >80 km in the simulations with J2010 melt distribution. Despite continued loss of ice volume, significant grounding-line retreat never initiates when using the F2014, S2016, or Cryo2 melt distributions with 1Obs intensity. Even in these simulations with little retreat, contributions to sea level exceed 2 mm by 2100.

3.4 Discussion

After evaluating how well the model simulations are able to replicate observed retreat over 1996-2018, we discuss how necessarily subjective modeling choices may have affected these results. We then evaluate the implications for the future evolution of this system.

3.4.1 Match to observations

Here we evaluate how different model forcings affect the match between the simulations and the observations of grounding-line position, thinning, and speed change.

3.4.1.1 Grounding-line position

The extensive, observed 30-km retreat (E. Rignot et al., 2014; Scheuchl et al., 2016) provides a clear metric for whether model simulations match the data. Along the Smith centerline, the bed depth remains at around 1 km b.s.l. for the first 10 km upstream from the grounding line before deepening to close to 2 km b.s.l. over the following ~10 km (Figure 3-3f), and in many simulations the grounding line never retreats off this relatively flat, shallow portion of the bed. This geometry leads to an essentially bimodal distribution bimodal distribution of grounding-line position along the Smith glacier centerline. Model simulations where the retreat reaches the retrograde slope past 10 km all reach >20 km of grounding-line retreat (Figure 3-3c). While only the full-Stokes simulation matches the timing of the observed retreat under 1Obs melt intensity, the pattern of retreat is similar regardless of model physics (discussed more in 3.4.2.1). We partition the simulations into those that display 15 km or more grounding-line retreat on Smith glacier, regardless of the timing, and those that do not; those that display this large retreat are considered generally good matches to the observed grounding-line positions where ~30-km of retreat was observed. The simulations that matched this large retreat were: those with the J2010 melt parameterization, regardless of melt intensity or marginal weakening; those with the S2016 or F2014 parameterization and 2Obs melt; and the simulation with the S2016 parameterization, 1Obs melt, and marginal enhancement of 4 (Table 3-1).

We find that grounding-line position is controlled by a combination of melt distribution, melt intensity, and marginal weakening, though melt near the grounding-line (a product of melt distribution and intensity) is the primary driver of retreat. This result confirms the conclusion of previous work that has also highlighted the importance of the melt distribution for determining ice-shelf stability (e.g., Olivier Gagliardini et al., 2010; D. N. Goldberg et al., 2018; Hélène

Seroussi & Morlighem, 2018). To match the observed grounding-line retreat using the 1Obs melt intensity, the models suggest that melt must have been concentrated near the grounding line. Concentrated melt at depth is expected given that the warm, salty CDW which drives melt generally intrudes at depth (e.g., Jacobs et al., 2012). However, without elevated melt intensity (relative to 1996) or greater concentration of melt at the grounding line than considered by our melt forcings, the "control melt" simulations show that the modeled grounding-line positions of Smith, Pope, and Kohler glaciers would have remained stable for the 50 years following 1996. The stable grounding-line position found by forcing the model with Cryo2 melt (Gourmelen et al., 2017) may result from underestimation of melt near the grounding line due to the difficulty of using satellite altimetry to infer melt rates in an area not in hydrostatic equilibrium (Fricker & Padman, 2006; Eric Rignot, 1998). Moreover, since melt rates were inferred over 2010-2016, the inferred melt rate beneath areas that ungrounded during that time mix periods of no melt and more intense melt. While our rescaling of parameterizations can increase the melt rates at the grounding line as the shelf-averaged ice draft decreases, the Cryo2 distribution does not allow the shelf to shallow out of melt, and so any underestimation of melt near the grounding line persists through the simulation. Thus, effective melt rates at the grounding line are lowest using the Cryo2 distribution, and they remain too low to instantiate retreat. Estimates of melt rates from ocean models should eventually provide a better option for forcing models, but computational constraints and poorly constrained cavity geometry prevent their widespread application at present (e.g., De Rydt & Gudmundsson, 2016).

It is possible that weakening of the margins of Crosson affected the timing of grounding-line retreat. Our model simulations applied an ad-hoc enhancement of 4 to the margins, which is akin to ~5° C of warming (Cuffey & Paterson, 2010), development of a relatively weak anisotropic

fabric (Ma et al., 2010), or some damage due to rifting (e.g., C. P. Borstad et al., 2013). While snapshot inversions for ice-shelf viscosity in 1996, 2011, and 2014 indicate some weakening of Crosson Ice Shelf (Lilien, Joughin, et al., 2018), this weakening cannot be definitively associated with a particular process. Thus, we are unable to identify if the weakening of the margins was causal in the observed speedup and retreat or if it was merely a result of the otherwise-initiated speedup (e.g. caused by rifting due speedup associated with ungrounding). We consider it unlikely, however, that changes to the strength of the shelf were the primary cause of retreat since the simulations marginal weakening but no increase beyond 1996 melt rates showed little retreat. Additionally, inversion results do not show significant weakening of Dotson Ice Shelf through this time (Lilien, Joughin, et al., 2018), suggesting that weakening was not the cause of Kohler Glacier's retreat even if it affected Pope and Smith Glacier, and thus does not explain widespread retreat in the area.

The modeled grounding-line positions demonstrate the stepwise nature of grounding-line retreat and highlight the complexity of assessing whether unstable retreat is taking place. Previous modeling has found that grounding lines tend to remain in relatively favorable positions for a period before abruptly retreating (e.g., I. Joughin et al., 2010), and the presence of grounding-line wedges at various points on the continental shelf indicate that retreat since the last glacial maximum followed a similar stepwise pattern with extended periods of stability (Graham et al., 2010; Smith et al., 2014). Similarly, exposure dating of glacial erratics along Pine Island Glacier indicate that during the Holocene it experienced periods slow retreat punctuated by decades or centuries of rapid thinning (Johnson et al., 2014). Our forced ungrounding experiments were designed to test whether the grounding line was situated such that some perturbation necessarily led to a continued step back to a new stable grounding-line position. While forced ungrounding

for 5 years resulted in retreat of one simulation that otherwise remained stable (17 vs. 19 in Table 3-1), even with elevated melt intensity the grounding line was able to stabilize on the retrograde slopes under some melt distributions (Figure 3-5), at least over the period of our simulations. Additionally, regardless of melt distribution, little further retreat was found in the 25 years following 18 years of forced ungrounding (Figure 3-5). The re-stabilization of the retreated grounding line indicates that small perturbations do not necessarily lead to immediate retreat, though 25- to 50-year simulations may simply be too short to capture the retreat that may eventually ensue. These forced ungrounding experiments also serve as a check upon the low temporal resolution of the melt forcing; the shelf-total melt was linearly interpolated between measurements in 1996 and 2006, and a brief period of elevated melt could have perturbed the grounding line during a subset of that time. However, the simulations with 5 years of forced ungrounding suggest that such a perturbation would not have led to immediate and sustained grounding-line retreat. Rather, sustained high melt rates at the grounding line appear to be necessary to cause the continuing grounding-line retreat that has been observed.

3.4.1.2 Ice surface elevation

In Figure 3-7, we compare modeled and measured ice-surface lowering. The comparison is confined to ice that was grounded in 1996 since observations have greater signal-to-noise ratio over grounded ice; on grounded ice, all thinning is expressed as surface lowering whereas on floating ice only ~10% of thinning is expressed at the surface. Observations of surface lowering were derived from the various altimetry products described in section 3.2.1 . The full-Stokes simulation slightly overestimates thinning along Smith Glacier while producing thickening upstream of Kohler Glacier's grounding line (Figure 3-7a). In general, the shallow-shelf simulations match the pattern of observed surface change reasonably well in the Smith and Pope

drainages, but the simulations generally thin too little in the Kohler drainage (Figure 3-7b-d). Even the simulations with 1Obs forcing that showed the most thinning slightly underestimate surface lowering. Part of this difference may reflect errors in the bed elevation; if the true bed elevation were greater than estimated in the bed product we used, a larger portion of dynamic thinning would have directly affected the surface height rather than contributing to ice-draft shallowing. An additional portion of the model-data mismatch is likely due to timing of retreat; a delayed response of the model could lead to underprediction of surface lowering. Given that the shallow-shelf simulations have delayed grounding-line retreat, it is unsurprising that they generally underestimate surface change.

The thickening (or lack of thinning) on Kohler may result from difficulties in initiating a model of an out-of-balance system. Melt and calving in 1996 were already larger than accumulation, likely due to elevated melt on Kohler (Lilien, Joughin, et al., 2018), and it is possible that the relaxation of the model prior to the simulations dampened real surface changes rather than artifacts from data errors in the Kohler drainage. Regardless of its cause, this discrepancy is transient and surface lowering eventually propagates up the trunk of Kohler as in observations. However, this thickening on Kohler, along with the shallow-shelf simulations' delayed grounding-line retreat and thinning, suggest that the simulations may underestimate future ice loss.

3.4.1.3 Ice-flow speed

We compare the model results to velocity mosaics for 2006-2012, 2014, and 2016-2018. The 2007-2010 velocities are derived from the Advanced Land Observation Satellite, processed using a combination of interferometry and speckle tracking (I. R. Joughin, 2002). We used feature tracking of Landsat-8 imagery to obtain velocities for the 2014–2015 austral summer. Velocity data for 2006 and 2011 are part of the NASA MEaSUREs dataset (J. Mouginot et al., 2014). We determined

the 2016–2018 velocity using speckle-tracking applied to data to Copernicus Sentinel-1A/B data. These observations indicate speedup both near the grounding lines of Smith and Kohler Glaciers and farther out on Crosson Ice Shelf (J. Mouginot et al., 2014). While the speedup near the grounding line is likely due a loss of basal resistance as a result of ungrounding, the speedup of the outer shelf may be due to changes in shelf viscosity or loss of buttressing at the terminus due to the breakup of the Haynes glacier tongue (Lilien, Joughin, et al., 2018).

The simulations indicate that ungrounding primarily affects speeds near the grounding line while speeds farther out on the shelf remain constant or decrease (Figure 3-1 and Figure 3-5). This heterogeneity results from buttressing; if the shelves were spreading freely, a change in grounding-line speed would cause an equal change in the speed of the shelves. Thus, speedup of the ice shelves is likely a result of local changes to buttressing. The model experiments with weakened margins find speedup along the Pope Glacier centerline on the outer portion of Crosson Ice Shelf (Figure 3-4d). While the modeled speed changes in the simulations with weakening closely match the observed speeds 40-60 km from the 1996 calving front, they show too little speedup closer to the front. This discrepancy across the shelf suggests that part of the observed changes in speed may be a result of forcing near the calving front, possibly associated with a loss of buttressing due to the breakup of the Haynes glacier tongue around 2002 or the progressive rifting of this area. While the simulations with weakened margins do not fully capture the observed velocity changes near the shelf margin, the marginal weakening does cause the model to more accurately reproduce speedup of the bulk of Crosson Ice Shelf. There are variety of possible reasons that the model does not capture the full spatial complexity of the observed speedup, for example weakening of the ice shelves, bed elevation errors, or inferred basal resistance being too low, and we cannot identify a single cause.

For the grounded ice, the simulations tend to under predict speedup on Smith Glacier, while generally overpredicting speed changes on Kohler Glacier (Figure 3-1). The timing of the speedup corresponds with the timing of rapid grounding-line retreat, so the delay in modeled grounding-line retreat likely causes the delay in modeled speedup. The scarcity of observations of grounding-line position and ice velocity earlier in the satellite records complicate the interpretation. Reliable grounding-line positions are unavailable between 1996 and 2011, and ice velocities are unavailable between 1996 and 2006. Significant retreat occurred during this time period, and transient speedup, such as that seen in the full-Stokes model along Kohler Glacier from 2005-2014 (Figure 3-1d), could have occurred during the gap in the observations.

3.4.2 Model limitations

We now evaluate effects that our choices in model complexity and melt forcing have on interpreting our results. In addition, the relative insensitivity of the modeled retreat to our choice of sliding law and of the model resolution are shown in Appendix B.

3.4.2.1 Model complexity

Full-Stokes models require significantly greater computing resources than shallow-shelf models of similar resolution. In the case of our simulations, the shallow-shelf simulations took ~1% of the CPU hours of an equivalent full-Stokes simulation, necessitating high-performance computing resources rather than local workstations. Thus, using the simplified physics of shallow-shelf models is desirable in cases where it is sufficient to capture the relevant processes. While we find slower initiation of retreat with shallow-shelf than with full-Stokes models, after initialization the pattern of retreat is similar between both classes of models.

Uncertainties in the model inputs, and necessary choices when initializing models, create significant spread in model retreat rates that could explain the difference between full-Stokes and

shallow-shelf simulations. For example, at Pine Island Glacier uncertainty in bed elevation propagates to uncertainty in the timing of retreat of around ±5-10 years depending on assumptions about the spectrum of the bed roughness (Sun et al., 2014). Moreover, with idealized geometry L1L2 models, a class of depth-integrated models with slightly greater complexity than shallow-shelf models, are more sensitive to high-frequency noise than full-Stokes models (Sun et al., 2014), suggesting the possibility that the uncertainty in bedrock elevation may affect the full-Stokes and shallow-shelf models in different ways.

The spacing of bed elevation measurements in our study region does not resolve detail with wavelengths of ~5 km and below. In addition, noise with longer wavelengths may be present if there are systematic biases in the measurements. Without constraints on this roughness, we cannot realistically assess how bed uncertainty may have affected the two types of models differently. However, comparison of observed and modeled grounding-line position and surface elevation suggest that errors in the bed dataset have indeed affected our results. The path of ungrounding of Smith Glacier for most model simulations progresses directly through an area that has been identified as having remained grounded through 2014 (E. Rignot et al., 2014; Scheuchl et al., 2016) despite the thinning rates in that area matching observations there. If the bed elevations were accurately captured by the bed product, accurately modeling thinning would be sufficient to accurately model retreat. By contrast, in an area where the bed is shallower than the bed product suggests, ungrounding would occur too early in the model and a greater portion of thinning would be expressed as ice-draft shallowing rather than surface lowering. Since the model finds ungrounding of a portion of Smith while approximately matching thinning rates there, it is likely that the bed is shallower there than the bed product indicates.

Bed elevation is only one of several inputs and aspects of initialization that could potentially cause different responses of models with differing physics. Time to full relaxation in the model spin-up, differences in the inferred basal shear stress resulting from inversion procedure implementation, or different response to errors in surface elevation all may explain a portion of the difference between full-Stokes and shallow-shelf models. Assessing the effect of uncertainties in these parameters would require considerable investigation that is beyond the scope of this study. However, given that there are known errors in the bed topography, and that the unconstrained frequency of bed noise affects the models differently, bed errors alone may change the timing of retreat by as much the model-data mismatch. Thus, while the difference in timing between full-Stokes and shallow-shelf models might indicate substantially better full-Stokes performance for at least one of the three glaciers, it could also reflect the uncertainty and not an indication that one type of model is better suited to describing this system. Indeed, while the full-Stokes model better matches the timing of retreat on Smith Glacier, its finds thinning rates that are a poorer match to observations and does not do a better job than the shallow-shelf model at reproducing retreat on Pope or Kohler glaciers. Unfortunately, we did have the computational resources to run sufficient full-Stokes runs to make a robust comparison of relative performance.

3.4.2.2 Melt forcing scheme

The application of the melt parameterizations in this study differs from previous work because, at each timestep where there are data, it rescales the parameterization so that model matches the observed shelf-wide integrated melt through time (Lilien, Joughin, et al., 2018). The primary advantage of this scheme is that it prevents the large, likely unrealistic changes to the shelf-total melt rate that occur as concentrated melt at depth causes the ice-shelf draft to shallow. We utilized this scheme primarily out of necessity; the grounding lines of Smith and Kohler Glaciers are

sufficiently deep that without scaling the melt forcing the shelf-total melt rates are drastically out of balance as simulations begin, and significant retreat ensues before the shelf is able to shallow out of the intense melt, thus leading to sustained, unphysically high melt rates. On the other hand, the continuous-rescaling scheme dampens feedbacks between the grounding-line retreat and the melt rate. Whereas a fixed parameterization generally causes an initial increase in shelf-total melt in response to a retreat of the grounding line since greater sub-shelf area is exposed, this continuous-scaling scheme will reduce the scaling of the melt distribution in response to that retreat. The continuous-rescaling scheme may thus unrealistically dampen feedbacks leading to rapid retreat, since increasing exposure of sub-shelf area may truly increase the total melt rate. Because melt is not solely a function of depth, any depth-dependent melt parameterization faces tradeoffs between fidelity to observations and simplicity, but the scheme used here is a reasonable compromise for a study that needs quasi-realistic melt rates at the beginning of simulations to enable comparison between model and observations.

3.4.2.3 Centennial simulations

The centennial-scale simulations that emulate observed grounding-line retreat (2, 4, and 19 in Table 3-1) all continue to produce retreat into the future. Even those simulations that do not capture the magnitude of recent retreat yield continuing mass loss resulting in over 2 mm of contribution to global mean sea level by 2100 (Figure 3-6). In the simulations with the 1Obs J2010 melt parameterization, nominally equivalent to no increase beyond 2014 melt forcing, ice losses exceed 8 mm sea-level equivalent and reaches 10 mm when marginal weakening is included. With the S2016 parameterization and marginal weakening, the grounding line also continues to retreat, albeit at a more moderate pace, and losses still reach 6 mm sea-level equivalent by 2100. This simulation with the S2016 forcing and marginal weakening is essentially a minimum loss scenario

amongst simulations capable of producing the observed retreat; shelf-total melt rates after 2014 remain below 50 Gt a^{-1}, lower than observed in 2006-2014, yet grounding line retreat and sea-level contribution continue unabated. Moreover, the delayed grounding-line retreat compared to observations and underestimation of thinning suggest that these projections are more likely to underestimate than overestimate future ice loss. Given the retreat produced by the simulations with the lowest melt, and that the thinning and grounding-line retreat rates suggest that these simulations underestimate loss, it is unclear whether Smith Glacier could now reach a new stable configuration before the grounding line recedes to the head of its trough.

While the volume above floatation in the Smith, Pope, Kohler catchment is relatively modest, if thinning were to extend to the divide with the Thwaites catchment, additional losses could result. Due to the extensive grounding-line retreat already undergone by Smith Glacier, the simulations with the J2010 melt distribution suggest that significant (>50 m) thinning could reach the divide shared with Thwaites by the end of the 21st century. This thinning could further contribute to the destabilization of the interior of Thwaites caused by changes at Thwaites' terminus (I. R. Joughin et al., 2014). Because of their limited domain, our model simulations are unable to assess the effects of divide migration on regional ice loss, and bed topography might isolate the loss to Smith's present catchment. However, given the potential for divide migration, studies concerned with the stability of Thwaites Glacier on timescales longer than ~100 years may underestimate ice loss if they do not account for potential drainage capture by Smith Glacier.

3.5 Conclusions

Using reasonable melt intensity distributed with simple, depth-dependent parameterizations, our model simulations are able to reproduce the recent speedup, thinning, and retreat of Smith, Pope, and Kohler Glaciers, albeit with some uncertainty in the timing. These simulations suggest that in

1996 Smith Glacier was in a state of precarious stability, but nonetheless elevated melt rates were needed to cause the observed grounding-line retreat. While weakening of the margins of Crosson Ice Shelf may have played a role in the speedup of the shelf, it is unlikely that such a change precipitated the observed retreat. Those model simulations that successfully reproduce recent changes continue to show grounding-line retreat into the future, and we find that the rate of ice loss is likely to grow in the coming decades. By the end of our ~100-year simulations, thinning has extended to the ice divide separating Smith and Kohler from Thwaites Glacier, indicating the potential for Smith's retreat to hasten the destabilization of that larger catchment.

Acknowledgements Computing resources were provided by the NASA high performance computing center. DL was supported by NASA headquarters through the NASA Earth and Space Sciences Fellowship (NNX15AN53H). NASA (NNX17AG54G) also provided support for contributions by IJ and BS.

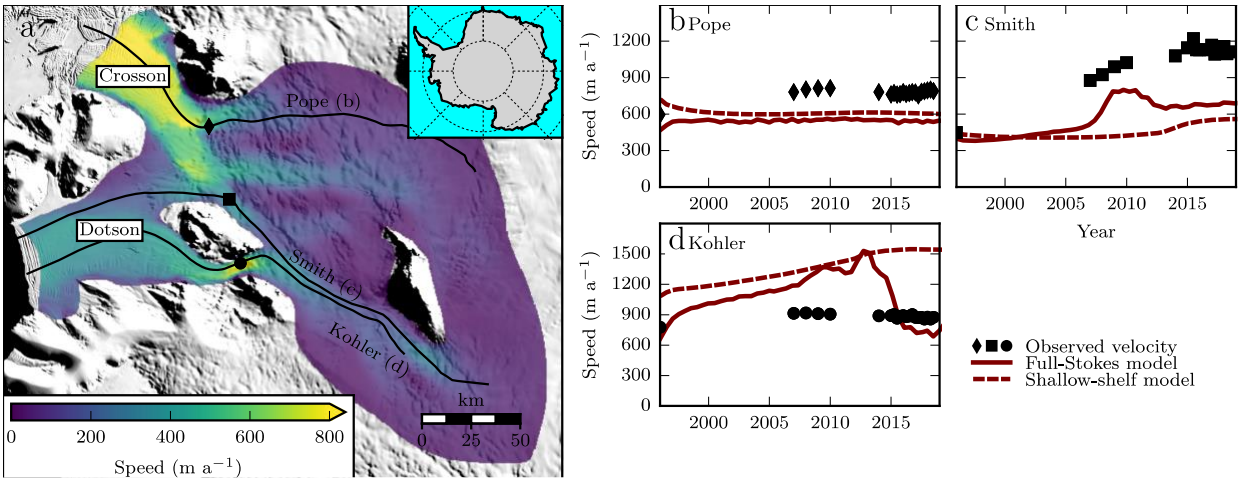

Figure 3-1. Modeled velocity changes.

a. Modeled velocities after initialization in the full-Stokes model. Black lines indicate flowlines for the three outlet glaciers. Inset shows location of study area. **b-d.** Observed and modeled velocities at points indicated in a. Solid line corresponds to the full-Stokes model with 1Obs J2010 melt forcing and thin, dashed line corresponds to shallow-shelf model, also with 1Obs J2010 melt forcing. Symbols indicate satellite observations of velocity.

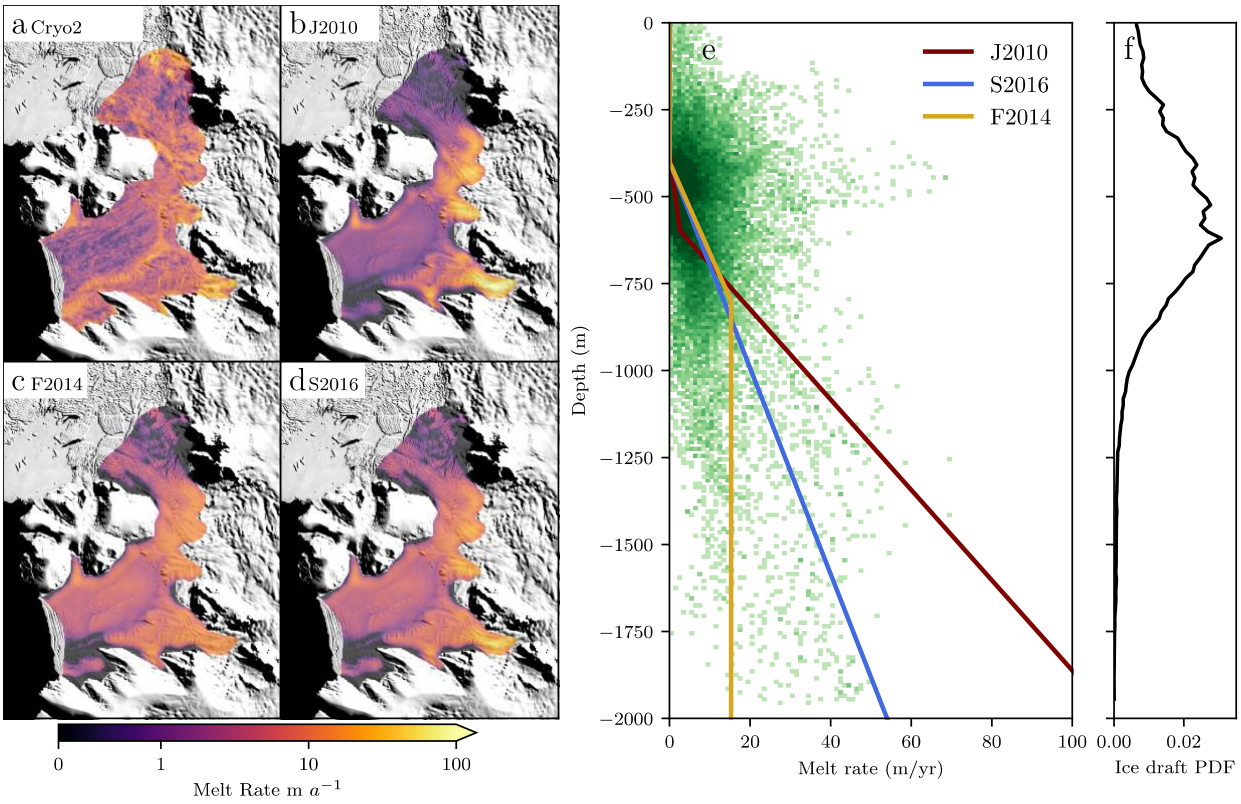

Figure 3-2. Melt forcings used for modeling.

a-d. Distribution of melt rates at the beginning of simulations using Cryosat-inferred rates from Gourmelen et al. (2017), and parameterizations from Joughin et al. (2010), Favier et al. (2014), and Shean (2016) respectively. **e.** Scaled parameterizations (colored lines) plotted over green points showing Cryosat-derived distribution of melt. Darker colors indicate greater area with a given combination of depth and melt rate. **f.** PDF of depths; this indicates the total area at each depth, showing how shelf-total melt rates are most sensitive to melt rates between ~250 and 600 meters.

	Model physics	*Melt dist.*	*Melt intensity*	*Enhancement in margins*	*Forced ungrounding*	*Sliding Law*	*Sim. len. (years)*	*>15 km retreat*
1	FS	J2010	1Obs	1	No	Schoof	23	Yes
2	SSA	J2010	1Obs	1	No	Schoof	104	Yes
3	SSA	J2010	2Obs	1	No	Schoof	25	Yes
4	SSA	J2010	1Obs	4	No	Schoof	104	Yes
5	SSA	J2010	1Obs	1.8	No	Schoof	50	Yes
6	SSA	J2010	Control	4	No	Schoof	50	No
7	SSA	J2010	1Obs	1	5 years	Schoof	50	Yes
8	SSA	J2010	1Obs	1	18 years	Schoof	50	Yes*
9	SSA	J2010	1Obs	1	No	Weertman	50	Yes
10	SSA	F2014	1Obs	1	No	Schoof	104	No
11	SSA	F2014	2Obs	1	No	Schoof	25	Yes
12	SSA	F2014	1Obs	4	No	Schoof	50	No
13	SSA	F2014	Control	4	No	Schoof	50	No
14	SSA	F2014	1Obs	1	5 years	Schoof	50	No
15	SSA	F2014	1Obs	1	18 years	Schoof	50	Yes*
16	SSA	F2014	1Obs	1	No	Weertman	50	No
17	SSA	S2016	1Obs	1	No	Schoof	104	No
18	SSA	S2016	2Obs	1	No	Schoof	25	Yes
19	SSA	S2016	1Obs	4	No	Schoof	104	Yes
20	SSA	S2016	Control	4	No	Schoof	50	No
21	SSA	S2016	1Obs	1	5 years	Schoof	50	Yes
22	SSA	S2016	1Obs	1	18 years	Schoof	50	Yes*
23	SSA	S2016	1Obs	1	No	Weertman	50	No
24	SSA	Cryo2	1Obs	1	No	Schoof	104	No
25	SSA	Cryo2	2Obs	1	No	Schoof	25	No
26	SSA	Cryo2	1Obs	4	No	Schoof	50	No
27	SSA	Cryo2	Control	4	No	Schoof	50	No
28	SSA	Cryo2	1Obs	1	5 years	Schoof	50	No
29	SSA	Cryo2	1Obs	1	18 years	Schoof	50	Yes*
30	SSA	Cryo2	1Obs	1	No	Weertman	50	No

Table 3-1. Summary of model inputs.

Model physics and inputs are summarized in the first six columns. The last column indicates whether the Smith Glacier grounding line retreated over 15 km within the simulation, with starred entries indicating that the extent of retreat was explicitly forced.

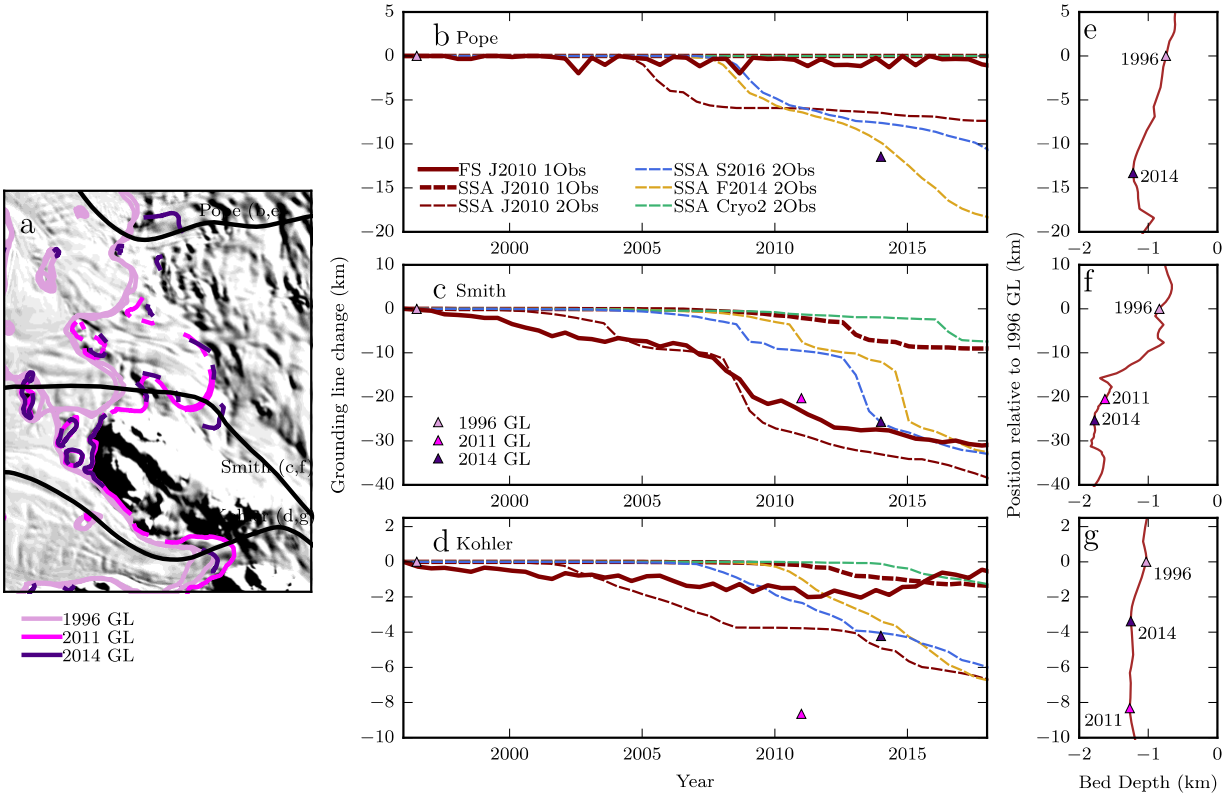

Figure 3-3. Sensitivity of change in grounding line position to melt distribution and intensity.

a. Flowlines used for evaluation of grounding line retreat (black). Pink and purple lines indicate observed grounding line positions (E. Rignot et al., 2014; Scheuchl et al., 2016). **b-d.** Modeled and observed grounding line position along the centerlines of Pope, Smith, and Kohler Glaciers respectively for different model simulations. Zero indicates no change since 1996, negative values indicate retreat. Line colors indicate melt distribution: J2010 (maroon), S2016 (blue), F2014 (gold), and Cryo2 (green). Line thickness indicates melt intensity: thin for 2Obs, thin for 2Obs. Line style indicates full-Stokes (solid) or shallow-shelf model (dashed). Simulations that display less than 2 km of grounding-line retreat on all centerlines are not shown. Triangles indicate observations of grounding line position, with colors corresponding to lines in a. **e-g.** Bed elevations vs distance from 1996 grounding line along the centerlines of Pope, Smith, and Kohler Glaciers respectively. Vertical scale matches panels b-d. Purple triangles again indicate observed grounding line positions through time.

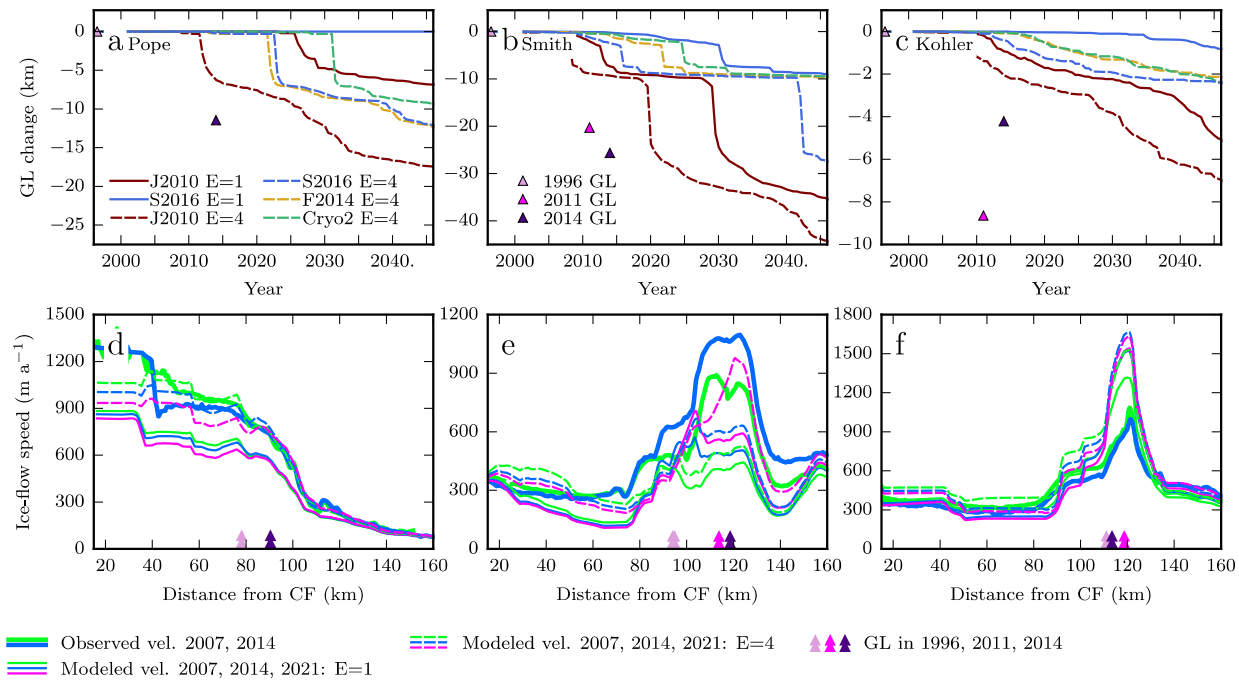

Figure 3-4. Effect of marginal weakening on grounding-line position and velocity.

a-c. Modeled grounding-line position through time along Pope, Smith East, and Kohler along flowlines shown in Figure 3-1. All simulations used 1Obs melt intensity. Colors indicate the melt forcing as in Figure 3-3. Solid line indicates no weakening, and dashed line indicates 4x enhancement within 10 km of the ice-shelf margins. Triangles show observed grounding line position (E. Rignot et al., 2014; Scheuchl et al., 2016). **d-f.** Velocity along flowlines corresponding to upper panels, with all simulations now using the J2010 melt parameterization. Color of line indicates the year (blue for 2007, green for 2014, pink for 2021). Thick lines show observations. Thinner lines show model results (using the J2010 melt parameterization), with dashed and solid patterns corresponding to the upper panels. Arrows at bottom indicate observed grounding-line position through time.

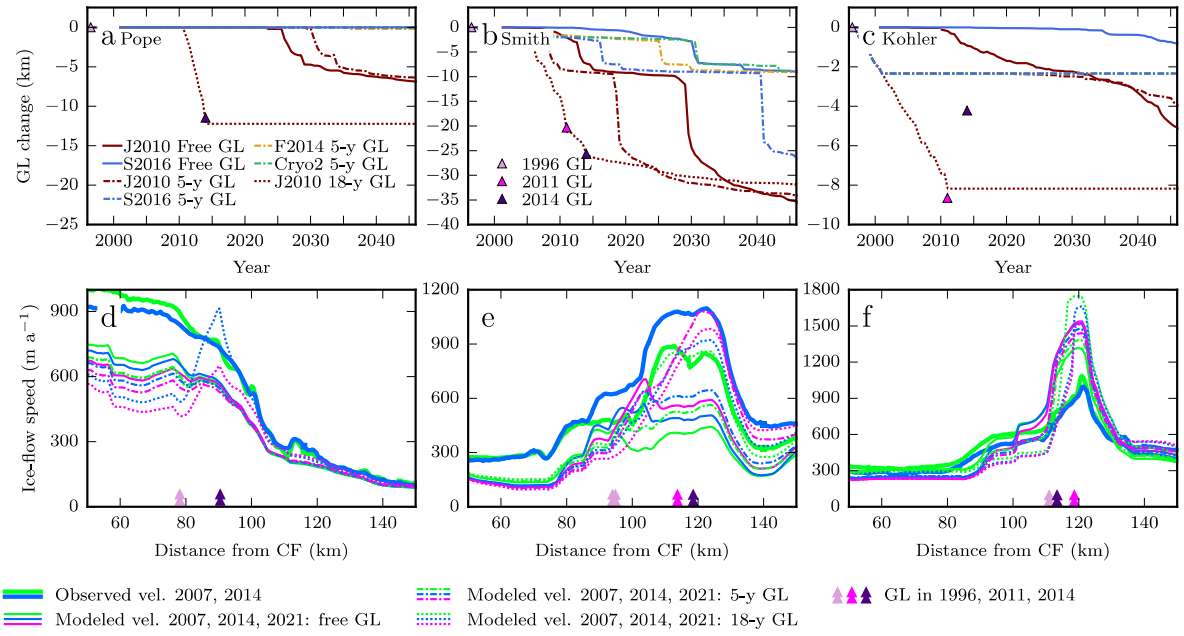

Figure 3-5. Grounding line and speed changes resulting from forced ungrounding.

a-c. Modeled grounding-line positions along centerlines of Pope, Smith East, and Kohler centerlines, respectively, from Figure 3-1. All simulations used 1Obs melt intensity with no marginal enhancement. Line style indicates how the grounding line was treated: solid line for freely evolving grounding line, dashed line for forced ungrounding for 18 years (1996-2014), and dash-dot for forced ungrounding for 5 years only (1996-2001). Triangles indicate observed grounding-line positions through time (E. Rignot et al., 2014; Scheuchl et al., 2016).. Simulations with no change in grounding-line position after the forced ungrounding are not shown. d-e. Observed and modeled ice speed along centerlines from upper panels, with line color indicating year as in Figure 3-4. Thick lines show observations. Thinner lines show model simulations (using J2010 melt distribution) with line style indicating ungrounding scheme as in a-c. Color of the line indicates the year. Triangles at bottom indicate the observed grounding-line position in different years; the effect of forced ungrounding on modeled ice speed is generally restricted to the area around the grounding line where the surface remains relatively steep while basal resistance is removed.

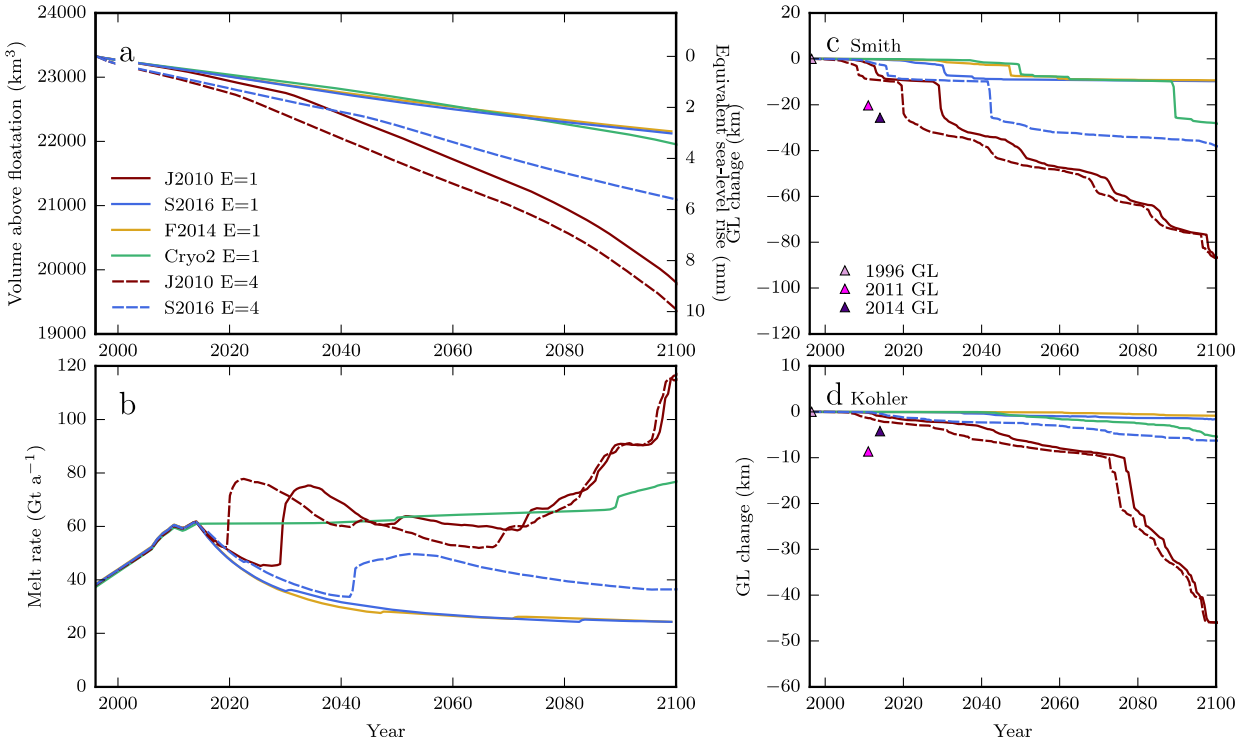

Figure 3-6. Results of centennial-scale model simulations.

a. Volume above floatation in the Smith, Pope, Kohler catchment and equivalent sea-level rise through time for extended simulations. All runs use 1Obs melt intensity. Color of line indicates melt distribution as in previous figures. Solid line corresponds to shallow-shelf model, and dashed line shows shallow-shelf model with enhanced margins. The difference in volume during the period including forcing result from different ice-flow speeds causing different calving rates. **b.** Melt rate through time. Runs are forced to observations through 2014, so melt rates correspond through this period, then diverge since the scaling of the melt parameterization is fixed at the 2014 value. Note that melt rates do not directly cause loss of volume above floatation since some melt distributions cause melt of the shelves without significant loss of grounded ice. **c-d.** Grounding-line position change through time along Smith and Kohler centerlines, respectively, from Figure 3-1. Purple triangles again show observed grounding-line positions through time (E. Rignot et al., 2014; Scheuchl et al., 2016).

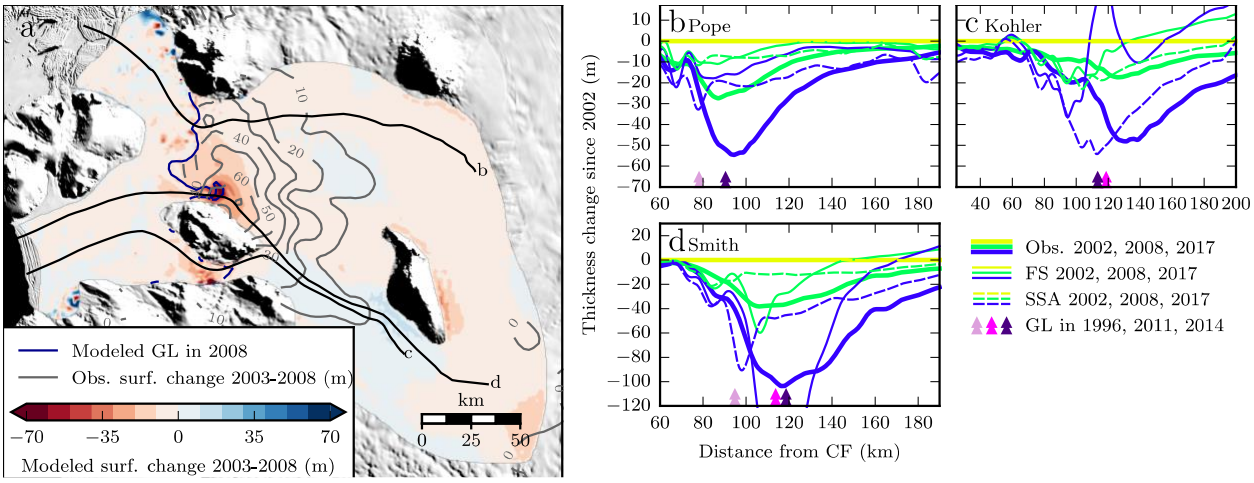

Figure 3-7. Modelled and observed thinning during the ICESat era (2003-2008).

a. Spatial distribution of thinning using the shallow-shelf model with J2010 1Obs melt. Colors indicate modelled thickness change while grey contours indicate observations. Black lines show flowlines as in other figures. Thin, blue line shows the modelled grounding line in 2008. **b-e.** Thinning through time along flowlines. Color indicates the year. Thin lines show model, thick lines show data derived from Operation IceBridge altimetry, ICESat-1, and WorldView/GeoEye DEMs. Triangles indicate grounding-line position (E. Rignot et al., 2014; Scheuchl et al., 2016).

Chapter 4 Holocene ice-flow speedup in the vicinity of South Pole

Abstract. The South Pole Ice Core (SPICEcore) was drilled at least 180 km from an ice-flow divide. Thus, the annual-equivalent layer thicknesses in the core are affected by spatial variations in accumulation upstream in addition to temporal variations in regional accumulation. We use a new method to compare the SPICEcore accumulation record, derived by correcting measured layer thicknesses for thinning, with an accumulation record derived from new GPS and radar measurements upstream. When ice speeds are modeled as increasing by 15% since 10 ka, the upstream accumulation explains 77% of the variance in the SPICEcore-derived accumulation (vs. 22% without speedup). This result demonstrates that the ice-flow direction and spatial pattern of accumulation were stable throughout the Holocene. The 15% speedup in turn suggests a slight (3-4%) steepening or thickening of the ice-sheet interior and provides a new constraint on the evolution of the East Antarctic Ice Sheet following the glacial termination.

Plain Language Summary. Understanding past changes in the flow of Antarctic ice is key to contextualizing modern glacier speedup and retreat, but there are few estimates of past flow speeds in the Antarctic interior. We used a new method to compare a direct record of the past 10,000 years of snowfall accumulation near South Pole, derived from layers in the new South Pole Ice Core, with an estimate of the snowfall upstream over the last 150 years. By seeing how these records correlate, we provide a new constraint on past ice flow in the region, showing that the flow direction has been unchanged for 10,000 years while flow speeds have increased slightly during that time. This analysis also shows that most of the variations of layer thickness in the South Pole Ice Core result from ice flow rather than variations in accumulation through time. These results provide new data that can help improve models of ice flow over the last 10,000 years.

4.1 Introduction

The East Antarctic Ice Sheet (EAIS) contains enough ice to raise sea level by ~53 m (Fretwell et al., 2013). However, for the EAIS to significantly contribute to future sea level, interior ice flow must speed up to evacuate currently slow-moving ice to the coast, a phenomenon that is not well constrained by observations. Ice-sheet models suggest the EAIS may be more responsive to climate changes than previously thought (e.g., DeConto & Pollard, 2016), and some models show that destabilization of marginal basins may rapidly cause thinning of the ice-sheet interior (Mengel & Levermann, 2014). Observations of past thickness and velocity changes of the EAIS can provide a useful constraint on such models.

Since ice-sheet thickness is affected by both accumulation and ice flow, information about past thickness is a useful constraint on both these quantities. Cosmogenic exposure dating of bedrock outcrops has been used to infer hundreds of meters of thinning near the East Antarctic margins during glacial termination, likely as a result of grounding-line retreat (e.g., Mackintosh et al., 2014). However, there is no exposed bedrock to constrain thinning in the EAIS interior. Ice cores provide one of the few direct sources of information about ice and climate history in the ice-sheet interior. For example, measurements of ice-core total gas content suggest ~100 m of thickening from the glacial to present at Vostok (Lorius et al., 1984), though poorly constrained firn-air content and atmospheric pressure lead to large uncertainties (Martinerie et al., 1994). Ice-core layer thicknesses suggest that EAIS thickening resulted from a ~50% accumulation increase from the glacial into the Holocene, with relatively steady accumulation since ~11 ka BP 1950 (hereafter simply ka; e.g., Veres et al., 2013). Targeted ice-flow models tuned to ice-core age and temperature records have been used to infer ~150 m of thickening at Domes C and Fuji from the Last Glacial Maximum to present (Parrenin et al., 2007). Continental-scale models forced by ice-core climate

histories also show similar changes in the EAIS interior (e.g., Golledge et al., 2012; Pollard & DeConto, 2009).

Despite Holocene (10.1 ka to present) thickness-change estimates for the EAIS interior, observational constraints on Holocene ice flow remain elusive. Here, we present a new constraint on the Holocene flow history near South Pole, where the present-day ice-flow speed is about 10 m/yr (Figure 4-1). Accumulation rates in the region are ~8 cm water-equivalent per year (Casey et al., 2014) and the ice is approximately 2700 m thick (Fretwell et al., 2013). This region is near the onset of Academy Glacier and the Support Force and Foundation Ice Streams, which drain into the Filchner-Ronne ice shelf (e.g., Wu & Jezek, 2004). Bingham et al. (2007) used internal radar reflections to infer a regional pattern of ice flow with faster flow in ice-stream tributaries. Beem et al. (2017) further analyzed deep radar structure and performed temperature modeling to infer a reorganization of ice flow and cessation of basal sliding prior to the Holocene (16.8-10.7 ka) but neither examined Holocene ice flow.

An intermediate-depth (1750 m) ice core (SPICEcore) was drilled at South Pole between 2014 and 2016. South Pole is at least 180 km from any ice divide, so the thickness of a packet of ice formed over a certain length of time (hereafter termed "layer thickness) in SPICEcore contains information about both spatial and temporal accumulation variations. The spatial variability has the potential to complicate interpretation of the climate history from the core, but here we use new field measurements to separate the spatial and temporal components of accumulation variability at the SPICEcore site. We then use the spatial variability to constrain the Holocene ice-flow history upstream.

4.2 Methods

To assess Holocene ice-flow conditions near South Pole, we compare two estimates of accumulation through time. The first is the SPICEcore-derived accumulation estimate, which incorporates information about both spatial and temporal variations in accumulation, but these influences are not easily separated. The second is an estimate of the component of the accumulation variations that would result from advection of the spatial pattern of accumulation upstream, inferred from geophysical (GPS and radar) measurements upstream. Combining this geophysically derived accumulation estimate, which contains purely spatial information, with the SPICEcore-derived history, which contains a mix of spatial and temporal information, allows the spatial and temporal records to be separated, yielding insight into Holocene variations in both ice flow and accumulation.

4.2.1 SPICEcore-derived accumulation history

The SPICE-core derived accumulation history is comprised of layer thicknesses measured in the core converted to accumulation using a model of the vertical component of ice flow. We derived a depth-age relationship for SPICEcore by matching the pattern of volcanic events (Rasmussen et al., 2013) identified with electrical conductivity measurements (Hammer et al., 1994) to ECM and Sulfur/Sulfate measurements of the annually resolved West Antarctic Ice-Sheet (WAIS) Divide ice core (Sigl et al., 2016). A total of 55 matches spanning 135 to 10,116 years BP 1950 (33.1 to 728.4 m) were found (Figure 4-2c; example matches in Figure C-3**Error! Reference source not found.**). We calculate the average annual-layer thickness between each pair of dated layers from the differences in their depths and differences in their ages (Figure 4-2d).

SPICEcore layer thicknesses are affected by three modes of variability (e.g. Waddington et al., 2007): advection of spatial variability in accumulation; temporal variability in accumulation at the

point where the parcel of ice originated; and post-depositional strain thinning due to ice flow. Our subsequent analysis uses only layers within the top third of the ice sheet, where the effects of strain thinning are relatively well constrained. We use a one-dimensional ice-flow model (Dansgaard & Johnsen, 1969), to estimate strain thinning of the SPICEcore layer thicknesses. For subsequent analysis, we "un-strain" the SPICEcore layer thicknesses to obtain the ice-equivalent thickness of these layers when and where they were deposited (Figure 4-2e). The result is a history of the accumulation rates at the variable times and places where different parcels of ice in SPICEcore originated upstream. The resulting accumulation history is essentially trendless with time, providing a check that the ice-flow thinning function is reasonable.

4.2.2 Geophysically derived accumulation estimate

The geophysically derived accumulation estimate was determined by using our new measurements of ice-flow velocity vectors to determine the flowline into the SPICEcore site, then using new shallow radar profiles to infer the accumulation along this flowline.

4.2.2.1 Ice-flow velocities

The ice-flow velocity field was determined using repeat GPS surveys of pole positions (Figure 4-1). Accurate satellite velocity measurements are inhibited by the slow velocities in the region and by the oblique look angle of the few available satellite passes (Jeremie Mouginot et al., 2012; E Rignot et al., 2011). The modern flowline into the SPICEcore site (Figure 4-1) was determined by recursively stepping upstream in the direction opposite the velocity vectors (interpolated linearly from the GPS measurements) to obtain positions along the flowline (for details of GPS and flowline calculations, see Appendix C.1).

4.2.2.2 Spatial pattern of accumulation

Conversion of shallow radar-layer depths to accumulation rates requires knowing the layer ages. To determine the age of the radar layers discussed below, in January 2017 our team drilled a shallow (126 m) firn core (USP50) 50 km upstream from South Pole (Figure 4-1). We dated the USP50 firn core by matching volcanic events identified with ECM to either SPICEcore or WAIS Divide ECM and Sulfate (Table C-1). There are 16 match points between 1089 and 1877 CE (106.3 m and 22.15 m depth at ages 927 and 139 years respectively). To date each layer, we first found its depth in the radar trace closest to USP50. We then linearly interpolated between USP50 depths with ages known from the volcanic match to determine the ages of the radar layers.

We collected 238 line-km of 200-MHz radar data along and across the flowline leading to SPICEcore (for details, see Appendix C.2). Attenuation rates are low in the cold firn near South Pole, so radars operating at this frequency can image layers down to around 100 m depth. In the along-flow profile, we traced 16 continuously imaged layers for 100 km upstream from South Pole (Figure 4-3), and we also traced one of these layers, which was ~23 m deep, in our across-flow transects. This layer, which we dated to 1866 (150 years old), is old enough to average out annual-to-decadal-scale variability in accumulation, yet shallow enough to reduce the influence of horizontal advection on the inferred accumulation rate (for details, see Appendix C.3). The accumulation rate, in meters of ice equivalent per year, was found by integrating the density profile of the USP50 core above this layer at each radar trace and dividing by the layer age obtained from the ECM measurements of the USP50 core.

We used density profiles measured along four cores in the vicinity of South Pole to estimate the uncertainty in accumulation contributed by regional density variations; we find that these variations are small compared to the variation in accumulation rate inferred by variations in layer

depth (see Appendix C.4). To determine sensitivity of accumulation rate to the position of the flowline, we calculated a decorrelation length, defined as the lag distance at which the spatial autocorrelation of the accumulation rate becomes insignificant at the 95% confidence level (see Appendix C.5).

4.2.2.3 Estimated accumulation variations

From the data described above, we estimate the variations in accumulation expected to advect to the SPICEcore site at different times given the hypothesis that the modern accumulation rate and pattern and ice-flow velocity upstream have not changed through the Holocene. While constant accumulation rate and pattern, and constant ice-flow direction, began as hypotheses of our analysis, the correlations that we later show demonstrate their correctness. We first determined the modern accumulation rate at each point along the flowline using the depth of the 150-year layer at the nearest radar trace (Figure 4-2a and b). The spatially-integrated reciprocal of the horizontal velocity between SPICEcore and each point along the flowline determines that point's transit time to SPICEcore; in this region Holocene ice is in the upper ~600 m of the ice sheet, so surface velocities represent the horizontal flow speed along the entire paths of particles advected to SPICEcore. We use these transit times to convert the accumulation rate along the flowline into an accumulation as a function of transit time to the SPICEcore site (Figure 4-2f).

4.2.3 Correlation between accumulation records

Since both accumulation estimates are functions of time, comparison of these estimates can be done directly without knowledge of the exact path particles traversed to arrive at different depths in SPICEcore. Previous work on past accumulation near other ice cores has been forced to rely upon calculating particle paths (e.g., Koutnik et al., 2016), and so by avoiding this dependence our methods eliminate a significant source of complexity and uncertainty. To calculate the correlation

between accumulation records, we first binned the geophysically derived accumulation estimate into the intervals between dated layers in SPICEcore, since this is the temporal resolution of the SPICEcore-derived history. We limited the analysis to intervals between 1.3 ka and 10.1 ka. For ages younger than 1.3 ka, the radar line is more than 1 km from the flowline due to data-collection restrictions near South Pole Station. For ages older than 10.1 ka, the large variations in accumulation during the glacial termination (e.g., Bazin et al., 2013; Fudge et al., 2016) complicate the correlation analysis because assumptions about temporally variable accumulation and flow are required. We calculated Pearson's correlation coefficient (r) between accumulation records for all 43 dated intervals between 1.3 ka and 10.1 ka to determine the amount of variance explained (r^2).

Given different hypotheses about velocity changes upstream of SPICEcore, this analysis can be repeated to determine if the accumulation estimates derived from any alternative velocity histories better explain the variance in the SPICEcore-derived history than the constant-velocity model does. The highest correlation with the SPICEcore-derived accumulation history is expected from the flow speed that best matches the actual conditions through the Holocene. For simplicity, we retain the hypothesis that accumulation rates and flow directions were stable at their modern values, but we evaluate the effect of hypothesized linear temporal variations in speed from either slower or faster than modern at 10.1 ka to modern speeds at present. For each of these hypothesized changes in flow speed (we used a range from 30% slowdown to 60% speedup in 1% increments), we recalculated the age at points along the flowline using the transit time between those points and the SPICEcore site. By interpolating the accumulation rates onto these points, we inferred 90 alternate estimates of the annual-layer thickness that would be advected to the SPICEcore site. We then computed the correlation between each new estimate and the SPICEcore-derived history. For all estimates, accumulation is nearly trendless with time, and thus correlation with the SPICEcore-

derived history is driven by alignment of the high-frequency variability in the accumulation estimates.

4.3 Results

Surface velocities range from ~10 m/yr near SPICEcore to ~3 m/yr at 100 km upstream (Figure 4-1, Table S2). Flow towards South Pole is generally along the 140E meridian, though 100 km from SPICEcore the flow aligns closer to 160E, indicating the ice originates from Titan Dome (Figure 4-1). At modern speeds, ice 100 km upstream would take ~17,000 years to reach the SPICEcore site, while ice at 70 km would take ~10,000 years. Uncertainty in the GPS measurements (~1-6 cm in each horizontal direction) introduces an uncertainty of less than 1% in the velocity with the smallest velocity uncertainties nearest to South Pole because of the higher velocities. The GPS uncertainties have a minimal impact on the flowline position: at 70 km, the standard deviation is 0.24 km along or across flow (equivalent to 31 years in the along flow direction) along flow and at 100 km the standard deviation is 0.9 km (equivalent to 293 years along flow).

The accumulation rate along the flowline is 9±1.5 cm/yr (ice equivalent), with no statistically significant spatial trend. The accumulation-rate pattern decorrelates after a radius of 0.9 km across flow and 1.8 km along flow. The relatively short across-flow profile suggests the along-flow estimate is more reliable, but both length scales are several times larger than the 95% confidence bounds on the modern flowline during the 1.3-10.1 ka interval.

The correlation between accumulation records is shown in Figure 4-4. The variance explained is calculated with each interval weighted equally regardless of its duration. Appendix C.6 and Figure C-3**Error! Reference source not found.** show correlations with three additional methods of weighting the layers; they all produce similar correlations (maximum r^2 values for each method

range from 0.72 to 0.81). Figure 4-4d shows the fraction of variance of the SPICEcore-derived history explained by the model for different linear trends in velocity; a positive value for the speed change indicates the speed was slower than today at 10.1 ka, and a negative value indicates the speed was faster than today. Speedups between 3 and 33% all result in geophysically derived estimates that are correlated with the SPICEcore-derived history at the 95% confidence level (see Appendix C.5). For all methods of weighting the intervals, the variance explained is maximized with a 14-15% speedup during the Holocene, i.e. speeds were likely ~15% slower at 10.1 ka than at present. With the 15% speedup applied, the model explains 77% of the variance in the SPICEcore-derived history, while with no speedup 22% of the variance is explained. Because a 15% speedup is large compared to the age uncertainty in the modern flowline (<1% at 10 ka), it represents a real change in velocity rather than poor measurement of present-day flow.

4.4 Discussion

In order to interpret our results as a constraint on flow speed and direction, we use the across- and along-flow variations in accumulation rate to determine how flow change would have affected the correlation. Because the decorrelation length of the upstream accumulation rate is large compared to the uncertainty in the modern flowline, the correlation between the SPICEcore-derived history and the geophysically derived estimate is insensitive to the uncertainty in the modern velocities. However, relatively minor (2 km) horizontal variations of past flow would have caused significant changes to the correlation. Thus, the high correlation between the SPICEcore and upstream records implies that neither the position of the flowline nor the accumulation pattern changed by more than two kilometers in the past ~10 ka, confirming the hypothesis that these quantities have been approximately constant through the Holocene.

We have chosen one simple parameter (linear change in ice-flow speed) to vary in this analysis in order to match the SPICEcore-derived accumulation history. More free parameters (e.g. temporally variable accumulation or flow direction) almost certainly would allow tuning to explain more of the variance in the SPICEcore-derived history, but additional data are required to prevent overfitting if more free parameters are added to the model. Future work could attempt to utilize additional data, such as additional radar layers, with the goal of uniquely inferring more complex changes.

The pattern of accumulation (Figure 4-3), and the relatively small spatial scale on which it varies, suggests that the pattern of snowfall is controlled by persistent surface topography (e.g., Hamilton, 2004). We are unable to find a simple relationship between the accumulation pattern and the surface elevation, slope, or curvature along the flowline. This contrasts with Hamilton (2004), who found a qualitative relationship between the accumulation rate in a firn core at South Pole and the surface slope for ~8 km upstream, where the ice originated for the past 800 years. However, accumulation patterns are likely controlled by topography in the wind direction rather than the flow direction (e.g., Arcone et al., 2005). South Polar winds primarily come from ~30E (Lazzara et al., 2012), which is oblique to our radar profiles, so we cannot assess the relationship between accumulation and along-wind topography.

The small (23%) residual variability in the SPICEcore-derived accumulation not explained by the geophysically derived accumulation estimate represents the sum of temporal variability in climate, and any incorrect assumptions in our analysis. The key assumption used to separate the spatial and temporal variations in layer thickness is that the temporal signal is not correlated with the spatial pattern upstream; because we perform the analysis with the same 150-year accumulation interval for all distances upstream, this assumption is valid. Thus, we attribute the correlation solely to

advection of conditions upstream, while the residual primarily represents the temporally variable processes that decrease the correlation. The residual layer-thickness variability (5% for interval lengths > 50 years) is similar to the temporal variations in accumulation rate inferred from other East Antarctic sites (4-7%; Veres et al., 2013), but is less than half of WAIS Divide (13%; Fudge et al., 2016). Thus, it is unlikely that the relatively large Holocene accumulation variations at WAIS Divide extended to the South Pole region.

A 15% increase in velocity through the Holocene could have resulted from small, gradual increases of thickness or surface slope in response to deglaciation. Assuming no sliding, as suggested by modeled temperature-depth profiles near South Pole (Beem et al., 2017; Price et al., 2002), the surface velocity of ice is proportional to the third power of the surface slope and the fourth power of the ice thickness (e.g., Cuffey & Paterson, 2010). Thus, a 4.4% increase in slope (~0.65 m/km) would result in a 15% speedup. This change is reasonable given the increase in accumulation in the interior of the EAIS prior to 10.1 ka (e.g., Bazin et al., 2013; Parrenin et al., 2007) and the ~350 m thinning ~800 km downstream on the Foundation Ice Stream between ~10 and 2.5 ka (Bentley et al., 2017). A thickening of 3.3% (~90 m), could also cause 15% speedup. Such thickening is consistent with the ~150 m of thickening found by ice-flow models, both continental scale (e.g., Golledge et al., 2012) and targeted to ice-core sites in the EAIS (Parrenin et al., 2007), though models differ as to whether thinning has continued at constant rates since 17 ka or has slowed through time. Thus, a 15% speedup is consistent with current estimates of Holocene changes to ice-sheet geometry.

Ice-flow models of Antarctica for the Holocene differ even as to the sign of the velocity changes near South Pole. For example, recent improvements to a well-established model have resulted in an estimate of 50% speedup rather than 11% slowdown (Pollard et al., 2016; Pollard & DeConto,

2009), though data to with which to compare such changes were absent. Our inferred speedup provides an important source of validation for the EAIS-interior ice-flow speeds produced by this type of model of deglaciation.

4.5 Conclusions

We have used a new method to compare two estimates of past accumulation near South Pole. Our work yields two primary insights. First, the majority of variance in SPICEcore-derived accumulation history is due to advection of temporally consistent spatial variations in accumulation upstream; most of the Holocene variability in SPICEcore layer thicknesses is not from changes in climate. Second, ice-flow speed near South Pole has increased approximately 15% during the Holocene. We are unaware of previous estimates of Holocene ice-flow velocities of the EAIS; prior work on past variations in ice velocity is limited to West Antarctica (e.g., Hulbe & Fahnestock, 2007; Ng & Conway, 2004). Our results support the overall findings of studies focused on EAIS thickness history, which generally infer that the EAIS experienced grounding-line retreat at the margins and modest thickening inland in response to the accumulation rate increase during the Holocene compared to glacial conditions (e.g., Mackintosh et al., 2014; Parrenin et al., 2007). Our measurements from South Pole can be used to assess the response of models of the EAIS to glacial-interglacial change and thus help constrain projections of EAIS contribution to future sea level rise.

Acknowledgements. This project was supported by the National Science Foundation (grants PLR-1443471 and 1443232). DL was partially supported by a NASA Earth and Space Sciences Fellowship (NNX15AN53H). We thank the Antarctic Support Contractor, Air National Guard, South Pole Station, UNAVCO, and Ice Drilling and Design Office (IDDO) for logistical support. We also thank Maurice Conway, David Clemens-Sewall, Austin Danicic, Elizabeth Morton and

Mike Waszkiewicz for assistance in the field. South Pole GPS data are available at https://www.unavco.org/instrumentation/networks/status/polar/overview/AMU2; ECM volcanic ties tied to the SP-ECM, and our GPS and radar data are archived at the US Antarctic Program Data Center (http://www.usap-dc.org/)

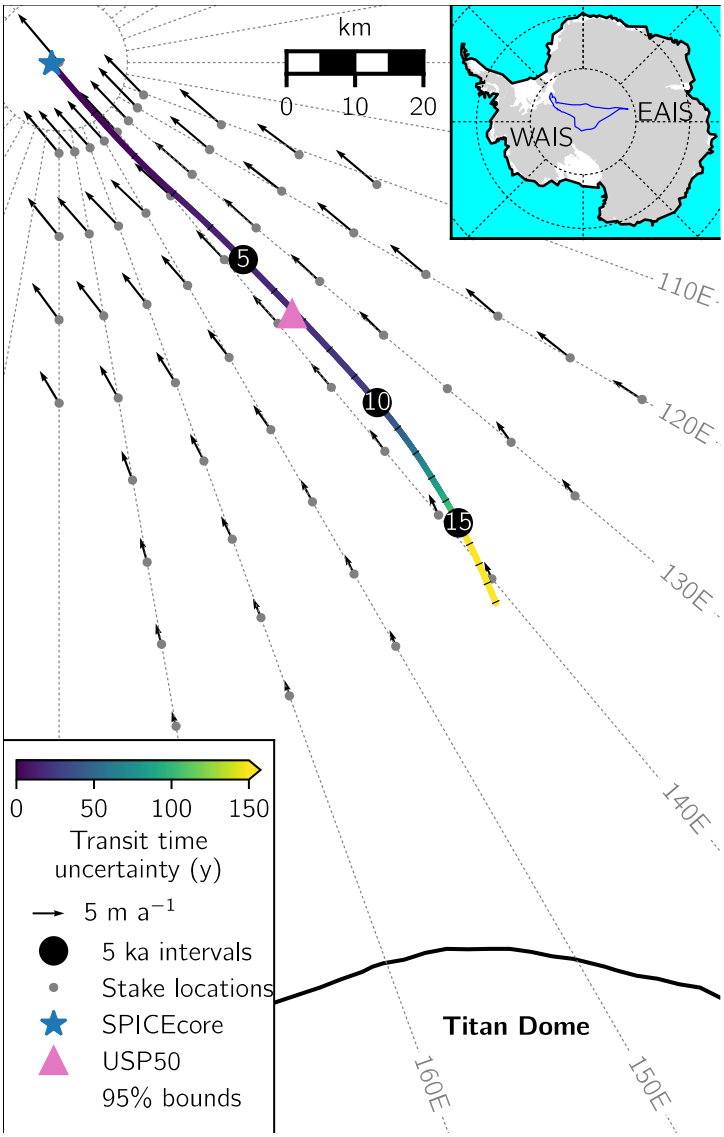

Figure 4-1 Flowline reaching SPICEcore.

Black circles indicate the time ice takes to flow to SPICEcore, in thousands of years, with ticks every 1000 years. Note that the South Pole is contained within the star representing SPICEcore. Colors along the flowline show uncertainty in transit time. Gray shaded region shows 95% confidence interval on the flowline. Vectors show GPS velocities at stakes locations; note, one stake was only surveyed once and does not have a velocity measurement. Black line indicates the 3130 m contour, which contains Titan Dome (Fretwell et al., 2013). Red box on inset shows location of main panel in the vicinity of South Pole, and blue outline indicates the drainage area of Academy Glacier through which ice from South Pole is thought to drain (E Rignot et al., 2011).

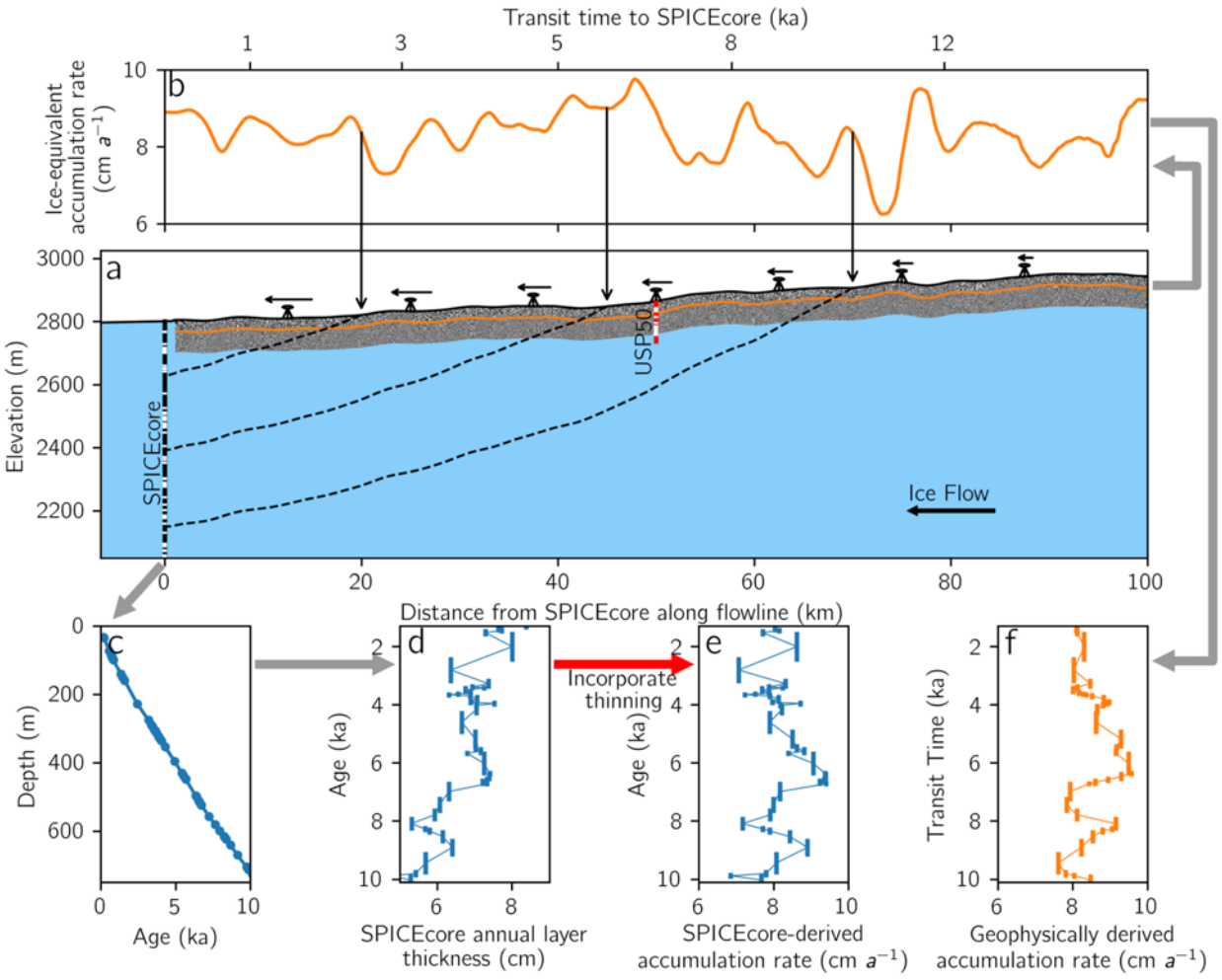

Figure 4-2 Methods used for correlation.

Gray arrows indicate the steps used to derive the datasets used for correlation. **a.** Relevant geometry. Shaded blue region shows the ice along the flowline to SPICEcore. Upper gray region shows shallow radar data; orange line is the layer traced to infer accumulation (layer 4 in Figure 3b). Illustrations of GPS receivers and vectors represent variations in ice-flow speed at measurement locations; speed decreases upstream from SPICEcore. Dashed, black lines show estimated particle paths from locations that reach SPICEcore; these lines are solely illustrative, as the exact paths are not needed in our analysis. Thick, black and red vertical lines show the locations of SPICEcore and USP50 respectively, with white marks showing the depth of dated layers in the cores. **b.** Spatial pattern of accumulation from layer 4. The integrated reciprocal of the velocity downstream of each point yields its transit time to SPICEcore (secondary x-axis). **c.** Age vs. depth at SPICEcore derived from ECM measurements. **d.** SPICEcore annual layer thicknesses. **e.**

SPICEcore-derived accumulation history. Less the error in the thinning function, this is the actual spatial and temporal variability in accumulation incorporated into SPICEcore. Red arrow emphasizes that this panel adds a modeled component to the data-based (c) and (d). **f.** Geophysically derived accumulation vs time (as in (b) but binned and plotted against transit time).

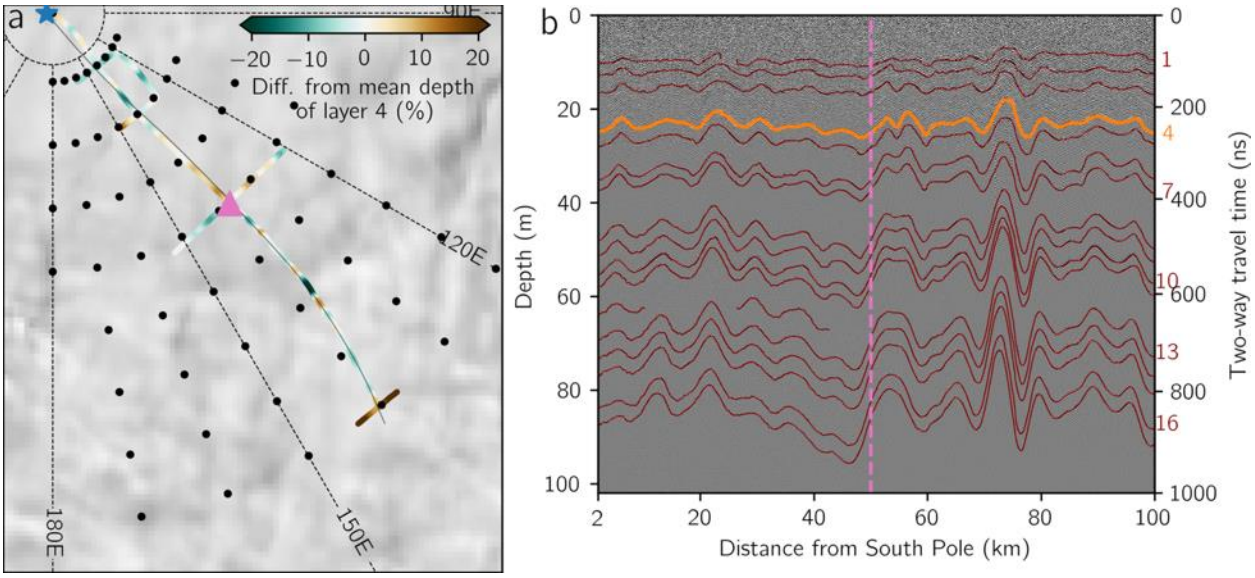

Figure 4-3 Shallow radar data used to determine the spatial pattern of accumulation.

a. Colors show depth of layer 4 from (b) compared to its mean, which is a proxy for accumulation rate over the last ~150 years. Green indicates shallower than average, brown indicates deeper. Solid black line shows the present-day flowline. Blue star and pink triangle indicate SPICEcore and USP50, respectively. Background shows satellite imagery (Haran et al., 2013); the scale and of features give a sense of kilometer-scale surface variability surrounding our survey. **b.** Radar-detected layers along the flowline (numbered on the right). Here, we use layer 4. Pink, dashed line indicates location of USP50.

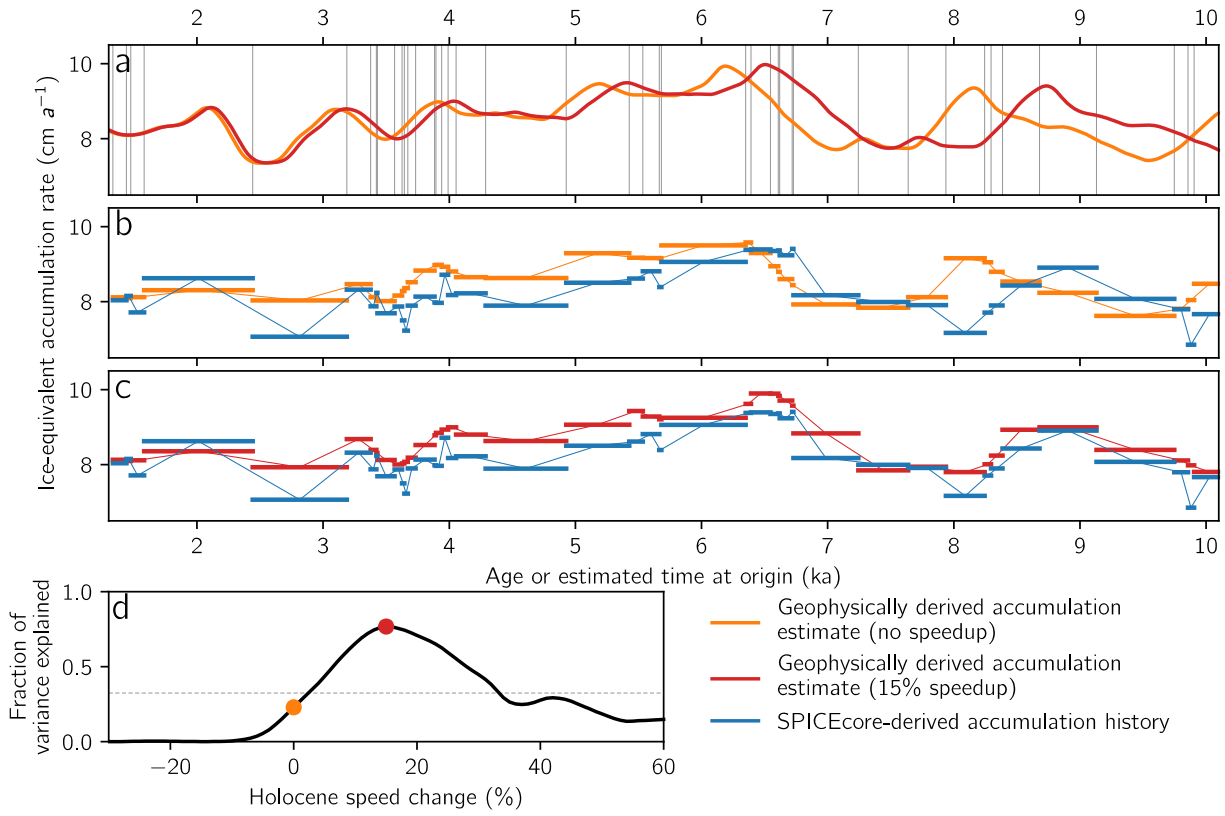

Figure 4-4 Correlation between accumulation records.

An identical figure incorporating uncertainty envelopes is included as Figure C-4. **a.** Geophysically derived accumulation rate as a function of transit time using modern velocities (orange) and applying the linear 15% increase in speed through the Holocene (i.e. with speeds 15% slower than modern at 10.1 ka) that maximizes correlation (red). Vertical lines show ages when SPICEcore is dated. **b.** Geophysically derived accumulation estimate without speedup (orange) and SPICEcore-derived accumulation history (blue). Thick lines show intervals between two dated layers in the core (the effective resolution); thin lines linearly connect these intervals for visual continuity). **c.** Same as (b), but the geophysically derived estimate incorporates a 15% speedup (red). **d.** Correlation coefficient between the accumulation estimates for different linear trends in Holocene speed. Positive speed change indicates speedup since 10.1 ka and negative change indicates slowdown since 10.1 ka. Dashed gray line indicates 95% confidence that the records are correlated. Dots show the correlations between the pairs of curves in b and c, respectively.

Bibliography

Ackert, R. P., Mukhopadhyay, S., Parizek, B. R., & Borns, H. W. (2007). Ice elevation near the West Antarctic Ice Sheet divide during the Last Glaciation. *Geophysical Research Letters*, *34*(21), L21506. https://doi.org/10.1029/2007GL031412

Alley, K. E., Scambos, T. A., Siegfried, M. R., & Fricker, H. A. (2016). Impacts of warm water on Antarctic ice shelf stability through basal channel formation. *Nature Geoscience*, *9*(4), 290–293. https://doi.org/10.1038/ngeo2675

Arcone, S. A., Spikes, V. B., & Hamilton, G. S. (2005). Stratigraphic variation within polar firn caused by differential accumulation and ice flow: interpretation of a 400 MHz short-pulse radar profile from West Antarctica. *Journal of Glaciology*, *51*(174), 407–422. https://doi.org/10.3189/172756505781829151

Assmann, K. M., Jenkins, A., Shoosmith, D. R., Walker, D. P., Jacobs, S. S., & Nicholls, K. W. (2013). Variability of Circumpolar Deep Water transport onto the Amundsen Sea Continental shelf through a shelf break trough. *Journal of Geophysical Research: Oceans*, *118*(12), 6603–6620. https://doi.org/10.1002/2013JC008871

Barnes, D. K. A., & Hillenbrand, C.-D. (2010). Faunal evidence for a late quaternary trans-Antarctic seaway. *Global Change Biology*, *16*(12), 3297–3303. https://doi.org/10.1111/j.1365-2486.2010.02198.x

Bazin, L., Landais, A., Lemieux-Dudon, B., Toyé Mahamadou Kele, H., Veres, D., Parrenin, F., … Wolff, E. (2013). An optimized multi-proxy, multi-site Antarctic ice and gas orbital chronology (AICC2012): 120-800 ka. *Climate of the Past*, *9*(4), 1715–1731. https://doi.org/10.5194/cp-9-1715-2013

Beem, L. H., Cavitte, M. G. P., Blankenship, D. D., Carter, S. P., Young, D. A., Muldoon, G. R., … Siegert, M. J. (2017). Ice-flow reorganization within the East Antarctic Ice Sheet deep interior. *Geological Society, London, Special Publications*, *461*.

Bentley, M., Hein, A., Sugden, D. E., Whitehouse, P. L., Shanks, A., Xuc, S., & Freeman, S. (2017). Deglacial history of the Pensacola Mountains, Antarctica from glacial geomorphology and cosmogenic nuclide surface exposure dating. *Quaternary Science Reviews*, *158*, 58–76. https://doi.org/10.1016/J.QUASCIREV.2016.09.028

Bingham, R. G., Siegert, M. J., Young, D. A., & Blankenship, D. D. (2007). Organized flow from the South Pole to the Filchner-Ronne ice shelf: An assessment of balance velocities in interior East Antarctica using radio echo sounding data. *Journal of Geophysical Research*, *112*(F3), F03S26. https://doi.org/10.1029/2006JF000556

Borstad, C. P., Rignot, E., Mouginot, J., & Schodlok, M. P. (2013). Creep deformation and buttressing capacity of damaged ice shelves: theory and application to Larsen C ice shelf. *The Cryosphere*, *7*(6), 1931–1947. https://doi.org/10.5194/tc-7-1931-2013

Borstad, C., Khazendar, A., Scheuchl, B., Morlighem, M., Larour, E., & Rignot, E. (2016). A constitutive framework for predicting weakening and reduced buttressing of ice shelves based on observations of the progressive deterioration of the remnant Larsen B ice shelf. *Geophysical Research Letters*, *43*(5), 2027–2035. https://doi.org/10.1002/2015GL067365

Calvetti, D., Morigi, S., Reichel, L., & Sgallari, F. (2000). Tikhonov regularization and the L-curve for large discrete ill-posed problems. *Journal of Computational and Applied Mathematics*, *123*(1–2), 423–446. https://doi.org/10.1016/S0377-0427(00)00414-3

Casey, K. A., Fudge, T. J., Neumann, T. A., Steig, E. J., Cavitte, M. G. P., & Blankenship, D. D. (2014). The 1500 m South Pole ice core: recovering a 40 ka environmental record. *Annals of Glaciology*, *55*(68), 137–146. https://doi.org/10.3189/2014AoG68A016

Cassotto, R., Fahnestock, M., Amundson, J. M., Truffer, M., & Joughin, I. (2015). Seasonal and interannual variations in ice melange and its impact on terminus stability, Jakobshavn Isbræ, Greenland. *Journal of Glaciology*, *61*(225), 76–88. https://doi.org/10.3189/2015JoG13J235

Ciais, P., Sabine, C., Bala, G., Bopp, L., Brovkin, V., Canadell, J., … Thornton, P. (2013). The physical science basis. Contribution of working group I to the fifth assessment report of the intergovernmental panel on climate change. *Change*, *IPCC Climate*. https://doi.org/10.1017/CBO9781107415324.015

Crabtree, R. D., & Doake, C. S. M. (1986). Radio-Echo Investigations of Ronne Ice Shelf. *Annals of Glaciology*, *8*, 37–41. https://doi.org/10.1017/S0260305500001105

Cuffey, K. M., & Paterson, W. S. B. (2010). The physics of glaciers.

Dahl, K. A., Spanger-Siegfried, E., Caldas, A., & Udvardy, S. (2017). Effective inundation of continental United States communities with 21st century sea level rise. *Elem Sci Anth*, *5*(0), 37. https://doi.org/10.1525/elementa.234

Dansgaard, W., & Johnsen, S. J. (1969). A Flow Model and a Time Scale for the Ice Core from Camp Century, Greenland. *Journal of Glaciology*, *8*(53), 215–223. https://doi.org/10.3189/S0022143000031208

De Rydt, J., & Gudmundsson, G. H. (2016). Coupled ice shelf-ocean modeling and complex grounding line retreat from a seabed ridge. *Journal of Geophysical Research: Earth Surface*, *121*(5), 865–880. https://doi.org/10.1002/2015JF003791

DeConto, R. M., & Pollard, D. (2016). Contribution of Antarctica to past and future sea-level rise. *Nature*, *531*(7596), 591–597. https://doi.org/10.1038/nature17145

Depoorter, M. A., Bamber, J. L., Griggs, J. A., Lenaerts, J. T. M., Ligtenberg, S. R. M., van den Broeke, M. R., & Moholdt, G. (2013). Calving fluxes and basal melt rates of Antarctic ice shelves. *Nature*, *502*(7469), 89–92. https://doi.org/10.1038/nature12567

Doake, C. S. M., Corr, H. F. J., Rott, H., Skvarca, P., & Young, N. W. (1998). Breakup and conditions for stability of the northern Larsen Ice Shelf, Antarctica. *Nature*, *391*(6669), 778–780. https://doi.org/10.1038/35832

Drews, R. (2015). Evolution of ice-shelf channels in Antarctic ice shelves. *The Cryosphere*, *9*(3), 1169–1181. https://doi.org/10.5194/tc-9-1169-2015

Dutrieux, P., De Rydt, J., Jenkins, A., Holland, P. R., Ha, H. K., Lee, S. H., … Schröder, M. (2014). Strong sensitivity of Pine Island ice-shelf melting to climatic variability. *Science (New York, N.Y.)*, *343*(6167), 174–8. https://doi.org/10.1126/science.1244341

Dutton, A., Carlson, A. E., Long, A. J., Milne, G. A., Clark, P. U., DeConto, R., … Raymo, M. E. (2015). Sea-level rise due to polar ice-sheet mass loss during past warm periods. *Science*.

https://doi.org/10.1126/science.aaa4019

Fahnestock, M. A., Scambos, T. A., Bindschadler, R. A., & Kvaran, G. (2000). A millennium of variable ice flow recorded by the Ross Ice Shelf, Antarctica. *Journal of Glaciology*, *46*(155), 652–664.

Favier, L., Durand, G., Cornford, S. L., Gudmundsson, G. H., Gagliardini, O., Gillet-Chaulet, F., … Le Brocq, A. M. (2014). Retreat of Pine Island Glacier controlled by marine ice-sheet instability. *Nature Climate Change*, *4*(2), 117–121. https://doi.org/10.1038/nclimate2094

Fretwell, P. T., Pritchard, H. D., Vaughan, D. G., Bamber, J. L., Barrand, N. E., Bell, R. E., … Zirizzotti, A. (2012). Bedmap2: improved ice bed, surface and thickness datasets for Antarctica. *The Cryosphere Discussions*. https://doi.org/10.5194/tcd-6-4305-2012

Fretwell, P. T., Pritchard, H. D., Vaughan, D. G., Bamber, J. L., Barrand, N. E., Bell, R. E., … Zirizzotti, A. (2013, February 28). Bedmap2: improved ice bed, surface and thickness datasets for Antarctica. *The Cryosphere*. Copernicus Publications on behalf of the European Geosciences Union.

Fricker, H. A., & Padman, L. (2006). Ice shelf grounding zone structure from ICESat laser altimetry. *Geophysical Research Letters*, *33*(15), L15502. https://doi.org/10.1029/2006GL026907

Fudge, T. J., Markle, B. R., Cuffey, K. M., Buizert, C., Taylor, K. C., Steig, E. J., … Koutnik, M. (2016). Variable relationship between accumulation and temperature in West Antarctica for the past 31,000 years. *Geophysical Research Letters*, *43*(8), 3795–3803. https://doi.org/10.1002/2016GL068356

Gagliardini, O., Durand, G., Zwinger, T., Hindmarsh, R. C. A., & Le Meur, E. (2010). Coupling of ice-shelf melting and buttressing is a key process in ice-sheets dynamics. *Geophysical Research Letters*, *37*(14), L14501. https://doi.org/10.1029/2010GL043334

Gagliardini, O., Zwinger, T., Gillet-Chaulet, F., Durand, G., Favier, L., Fleurian, B. de, … Thies, J. (2013). Capabilities and performance of Elmer/Ice, a new generation ice-sheet model. *Geoscientific Model Development Discussions*, *6*(1), 1689–1741. https://doi.org/10.5194/gmd-6-1299-2013

Gagliardini, O., Cohen, D., Råback, P., & Zwinger, T. (2007). Finite-element modeling of subglacial cavities and related friction law. *Journal of Geophysical Research*, *112*(F2), F02027. https://doi.org/10.1029/2006JF000576

Geuzaine, C., & Remacle, J.-F. (2009). Gmsh: A 3-D finite element mesh generator with built-in pre- and post-processing facilities. *International Journal for Numerical Methods in Engineering*, *79*(11), 1309–1331. https://doi.org/10.1002/nme

Gillet-Chaulet, F., Durand, G., Gagliardini, O., Mosbeux, C., Mouginot, J., Rémy, F., & Ritz, C. (2016). Assimilation of surface velocities acquired between 1996 and 2010 to constrain the form of the basal friction law under Pine Island Glacier. *Geophysical Research Letters*, *43*(19), 10,311-10,321. https://doi.org/10.1002/2016GL069937

Goldberg, D. N., Heimbach, P., Joughin, I., & Smith, B. (2015). Committed retreat of Smith, Pope, and Kohler Glaciers over the next 30 years inferred by transient model calibration. *The Cryosphere*, *9*(6), 2429–2446. https://doi.org/10.5194/tc-9-2429-2015

Goldberg, D. N., Gourmelen, N., Kimura, S., Millan, R., & Snow, K. (2018). How accurately should we model ice shelf melt rates? *Geophysical Research Letters*. https://doi.org/10.1029/2018GL080383

Goldberg, D. N., Narayanan, S. H. K., Hascoet, L., & Utke, J. (2016). An optimized treatment for algorithmic differentiation of an important glaciological fixed-point problem. *Geoscientific Model Development*, *9*(5), 1891–1904. https://doi.org/10.5194/gmd-9-1891-2016

Golledge, N. R., Fogwill, C. J., Mackintosh, A. N., & Buckley, K. M. (2012). Dynamics of the last glacial maximum Antarctic ice-sheet and its response to ocean forcing. *Proceedings of the National Academy of Sciences of the United States of America*, *109*(40), 16052–6. https://doi.org/10.1073/pnas.1205385109

Gourmelen, N., Goldberg, D. N., Snow, K., Henley, S. F., Bingham, R. G., Kimura, S., … van de Berg, W. J. (2017). Channelized Melting Drives Thinning Under a Rapidly Melting Antarctic Ice Shelf. *Geophysical Research Letters*. https://doi.org/10.1002/2017GL074929

Graham, A. G. C., Larter, R. D., Gohl, K., Dowdeswell, J. A., Hillenbrand, C.-D., Smith, J. A., … Deen, T. (2010). Flow and retreat of the Late Quaternary Pine Island-Thwaites palaeo-ice stream, West Antarctica. *Journal of Geophysical Research*, *115*(F3), F03025. https://doi.org/10.1029/2009JF001482

Ha, H. K., Wåhlin, A. K., Kim, T. W., Lee, S. H., Lee, J. H., Lee, H. J., … Kalén, O. (2014). Circulation and Modification of Warm Deep Water on the Central Amundsen Shelf. *Journal of Physical Oceanography*, *44*(5), 1493–1501. https://doi.org/10.1175/JPO-D-13-0240.1

Hamilton, G. S. (2004). Topographic control of regional accumulation rate variability at South Pole and implications for ice-core interpretation. *Annals of Glaciology*, *39*, 214–218. https://doi.org/10.3189/172756404781814050

Hammer, C. U., Clausen, H. B., & Langway, C. C. (1994). Electrical conductivity method (ECM) stratigraphic dating of the Byrd Station ice core, Antarctica. *Annals of Glaciology*. https://doi.org/doi:10.3189/172756494794587555

Haran, T., Bohlander, T., Scambos, T., Painter, T., & Fahnestock, M. (2013). *MODIS Mosaic of Antarctica (MOA) Image Map*. *National Snow and Ice Data Center*. Boulder, CO.

Hauer, M. E., Evans, J. M., & Mishra, D. R. (2016). Millions projected to be at risk from sea-level rise in the continental United States. *Nature Climate Change*, *6*(7), 691–695. https://doi.org/10.1038/nclimate2961

Hughes, T. J. (1981). The Weak Underbelly of the West Antarctic Ice- Sheet. *Journal of Glaciology*, *25*(9), 5–57.

Hulbe, C. L., & Fahnestock, M. (2007). Century-scale discharge stagnation and reactivation of the Ross ice streams, West Antarctica. *Journal of Geophysical Research*, *112*(F3), F03S27. https://doi.org/10.1029/2006JF000603

IPCC. (2007). Climate change 2007: the physical science basis. *Intergovernmental Panel on Climate Change*. https://doi.org/10.1038/446727a

Iverson, N. R., Hooyer, T. S., & Baker, R. W. (1998). Ring-shear studies of till deformation: Coulomb-plastic behavior and distributed strain in glacier beds. *Journal of Glaciology*, *44*(148), 634–642. https://doi.org/10.3189/S0022143000002136

Jacobs, S., Jenkins, A., Hellmer, H., Giulivi, C., Nitsche, F., Huber, B., & Guerrero, R. (2012). The Amundsen Sea and the Antarctic Ice Sheet. *Oceanography*, *25*(3), 154–163. https://doi.org/10.5670/oceanog.2012.90

Jamieson, S. S. R., Vieli, A., Livingstone, S. J., Cofaigh, C. Ó., Stokes, C., Hillenbrand, C.-D., & Dowdeswell, J. A. (2012). Ice-stream stability on a reverse bed slope. *Nature Geoscience*, *5*(11), 799–802. https://doi.org/10.1038/ngeo1600

Jenkins, A. (2011). Convection-Driven Melting near the Grounding Lines of Ice Shelves and Tidewater Glaciers. *Journal of Physical Oceanography*, *41*(12), 2279–2294. https://doi.org/10.1175/JPO-D-11-03.1

Jenkins, A., Dutrieux, P., Jacobs, S., Steig, E. J., Gudmundsson, G. H., Smith, J., & Heywood, K. J. (2016). Decadal ocean forcing and Antarctic ice sheet response: Lessons from the Amundsen Sea. *Oceanography*, *29*(4), 106–117. https://doi.org/10.5670/oceanog.2016.103

Jenkins, A., Shoosmith, D., Dutrieux, P., Jacobs, S., Kim, T. W., Lee, S. H., … Stammerjohn, S. (2018). West Antarctic Ice Sheet retreat in the Amundsen Sea driven by decadal oceanic variability. *Nature Geoscience*, 1. https://doi.org/10.1038/s41561-018-0207-4

Jenkins, A., Dutrieux, P., Jacobs, S. S., McPhail, S. D., Perrett, J. R., Webb, A. T., & White, D. (2010). Observations beneath Pine Island Glacier in West Antarctica and implications for its retreat. *Nature Geoscience*, *3*(7), 468–472. https://doi.org/10.1038/ngeo890

Johnson, J. S., Bentley, M. J., Smith, J. A., Finkel, R. C., Rood, D. H., Gohl, K., … Schaefer, J. M. (2014). Rapid Thinning of Pine Island Glacier in the Early Holocene. *Science*, *343*(6174), 999 LP-1001. https://doi.org/10.1126/science.1247385

Jordan, J. R., Holland, P. R., Goldberg, D., Snow, K., Arthern, R., Campin, J.-M., … Jenkins, A. (2018). Ocean-Forced Ice-Shelf Thinning in a Synchronously Coupled Ice-Ocean Model. *Journal of Geophysical Research: Oceans*, *123*(2), 864–882. https://doi.org/10.1002/2017JC013251

Joughin, I., Shean, D. E., Smith, B. E., & Dutrieux, P. (2016). Grounding line variability and subglacial lake drainage on Pine Island Glacier, Antarctica. *Geophysical Research Letters*, *43*(17), 9093–9102. https://doi.org/10.1002/2016GL070259

Joughin, I., Smith, B. E., & Holland, D. M. (2010). Sensitivity of 21st century sea level to ocean-induced thinning of Pine Island Glacier, Antarctica. *Geophysical Research Letters*, *37*(20), L20502. https://doi.org/10.1029/2010GL044819

Joughin, I. R. (2002). Ice-sheet velocity mapping: a combined interferometric and speckle-tracking approach. *Annals of Glaciology*, *34*(1), 195–201. https://doi.org/10.3189/172756402781817978

Joughin, I. R., Alley, R. B., & Holland, D. M. (2012). Ice-Sheet Response to Oceanic Forcing. *Science*, *338*(6111), 1172–1176. https://doi.org/10.1126/science.1226481

Joughin, I. R., Smith, B. E., & Medley, B. (2014). Marine ice sheet collapse potentially under way for the Thwaites Glacier Basin, West Antarctica. *Science (New York, N.Y.)*, *344*(6185), 735–8. https://doi.org/10.1126/science.1249055

Joughin, I. R., Tulaczyk, S., Bamber, J. L., Blankenship, D. D., Holt, J. W., Scambos, T., & Vaughan, D. G. (2009). Basal conditions for Pine Island and Thwaites Glaciers, West

Antarctica, determined using satellite and airborne data. *Journal of Glaciology*, *55*(190), 245–257. https://doi.org/10.3189/002214309788608705

Khazendar, A., Rignot, E., Schroeder, D. M., Seroussi, H., Schodlok, M. P., Scheuchl, B., … Velicogna, I. (2016). Rapid submarine ice melting in the grounding zones of ice shelves in West Antarctica. *Nature Communications*, *7*, 13243. https://doi.org/10.1038/ncomms13243

Konrad, H., Gilbert, L., Cornford, S. L., Payne, A., Hogg, A., Muir, A., & Shepherd, A. (2017). Uneven onset and pace of ice-dynamical imbalance in the Amundsen Sea Embayment, West Antarctica. *Geophysical Research Letters*, *44*(2), 910–918. https://doi.org/10.1002/2016GL070733

Kopp, R. E., Simons, F. J., Mitrovica, J. X., Maloof, A. C., & Oppenheimer, M. (2009). Probabilistic assessment of sea level during the last interglacial stage. *Nature*, *462*(7275), 863–7. https://doi.org/10.1038/nature08686

Koutnik, M. R., Fudge, T. J., Conway, H., Waddington, E. D., Neumann, T. A., Cuffey, K. M., … Taylor, K. C. (2016). Holocene accumulation and ice flow near the West Antarctic Ice Sheet Divide ice core site. *Journal of Geophysical Research: Earth Surface*, *121*(5), 907–924. https://doi.org/10.1002/2015JF003668

Lazzara, M. A., Keller, L. M., Markle, T., & Gallagher, J. (2012). Fifty-year Amundsen-Scott South Pole station surface climatology. *Atmospheric Research*. https://doi.org/10.1016/j.atmosres.2012.06.027

Leith, C. E. (1973). The Standard Error of Time-Average Estimates of Climatic Means. *Journal of Applied Meteorology*, *12*(6), 1066–1069. https://doi.org/10.1175/1520-0450(1973)012<1066:TSEOTA>2.0.CO;2

Ligtenberg, S. R. M., Helsen, M. M., & van den Broeke, M. R. (2011). An improved semi-empirical model for the densification of Antarctic firn. *The Cryosphere*, *5*(4), 809–819. https://doi.org/10.5194/tc-5-809-2011

Lilien, D. A., Joughin, I., Smith, B., & Shean, D. E. (2018). Changes in flow of Crosson and Dotson ice shelves, West Antarctica, in response to elevated melt. *The Cryosphere*, *12*(4), 1415–1431. https://doi.org/10.5194/tc-12-1415-2018

Lilien, D. A., Fudge, T. J., Koutnik, M. R., Conway, H., Osterberg, E. C., Ferris, D. G., … Stevens, C. M. (2018). Holocene Ice-Flow Speedup in the Vicinity of the South Pole. *Geophysical Research Letters*. https://doi.org/10.1029/2018GL078253

Lorius, C., Raynaud, D., Petit, J.-R., Jouzel, J., & Merlivat, L. (1984). Late-glacial maximum-Holocene atmospheric and ice-thickness changes from Antarctic ice-core studies. *Annals of Glaciology*, *5*(1), 88–94.

Lucchitta, B. K., Mullins, K., Smith, C. E., & Ferrigno, J. (1994). Velocities of the Smith Glacier ice tongue and Dotson Ice Shelf, Walgreen Coast, Marie Byrd Land, West Antarctica. *Annals of Glaciology*, *20*(1), 101–109. https://doi.org/10.3189/172756494794587573

Ma, Y., Gagliardini, O., Ritz, C., Gillet-Chaulet, F., Durand, G., & Montagnat, M. (2010). Enhancement factors for grounded ice and ice shelves inferred from an anisotropic ice-flow model. *Journal of Glaciology*, *56*(199), 805–812. https://doi.org/10.3189/002214310794457209

MacAyeal, D. R. (1989). Large-scale ice flow over a viscous basal sediment: Theory and application to ice stream B, Antarctica. *Journal of Geophysical Research*, *94*(B4), 4071–4087. https://doi.org/10.1029/JB094iB04p04071

MacAyeal, D. R. (1993). A tutorial on the use of control methods in ice-sheet modeling. *Journal of Glaciology*, *39*(131). https://doi.org/10.1017/S0022143000015744

Macgregor, J. A., Catania, G. A., Markowski, M. S., & Andrews, A. G. (2012). Widespread rifting and retreat of ice-shelf margins in the eastern Amundsen Sea Embayment between 1972 and 2011. *Journal of Glaciology*, *58*(209), 458–466. https://doi.org/10.3189/2012JoG11J262

Mackintosh, A. N., Verleyen, E., O'Brien, P. E., White, D. A., Jones, R. S., McKay, R., … Masse, G. (2014). Retreat history of the East Antarctic Ice Sheet since the Last Glacial Maximum. *Quaternary Science Reviews*, *100*, 10–30. https://doi.org/10.1016/j.quascirev.2013.07.024

Marsh, O. J., Fricker, H. A., Siegfried, M. R., Christianson, K., Nicholls, K. W., Corr, H. F. J., & Catania, G. (2016). High basal melting forming a channel at the grounding line of Ross Ice Shelf, Antarctica. *Geophysical Research Letters*, *43*(1), 250–255. https://doi.org/10.1002/2015GL066612

Martinerie, P., Lipenkov, V. Y., Raynaud, D., Chappellaz, J., Barkov, N. I., & Lorius, C. (1994). Air content paleo record in the Vostok ice core (Antarctica): A mixed record of climatic and glaciological parameters. *Journal of Geophysical Research*, *99*(D5), 10565. https://doi.org/10.1029/93JD03223

Maule, C. F., Purucker, M. E., Olsen, N., & Mosegaard, K. (2005). Heat flux anomalies in Antarctica revealed by satellite magnetic data. *Science (New York, N.Y.)*, *309*(5733), 464–7. https://doi.org/10.1126/science.1106888

Medley, B., Joughin, I. R., Smith, B. E., Das, S. B., Steig, E. J., Conway, H., … Leuschen, C. (2014). Constraining the recent mass balance of Pine Island and Thwaites glaciers, West Antarctica with airborne observations of snow accumulation. *The Cryosphere Discussions*, *8*(1), 953–998. https://doi.org/10.5194/tcd-8-953-2014

Mengel, M., & Levermann, A. (2014). Ice plug prevents irreversible discharge from East Antarctica. *Nature Climate Change*, *4*(6), 451–455. https://doi.org/10.1038/nclimate2226

Miles, T., Lee, S. H., Wåhlin, A., Ha, H. K., Kim, T. W., Assmann, K. M., & Schofield, O. (2015). Glider observations of the Dotson Ice Shelf outflow. *Deep Sea Research Part II: Topical Studies in Oceanography*, *123*, 16–29. https://doi.org/10.1016/j.dsr2.2015.08.008

Millan, R., Rignot, E., Bernier, V., Morlighem, M., & Dutrieux, P. (2017). Bathymetry of the Amundsen Sea Embayment sector of West Antarctica from Operation IceBridge gravity and other data. *Geophysical Research Letters*, *44*(3), 1360–1368. https://doi.org/10.1002/2016GL072071

Morlighem, M., Rignot, E., Seroussi, H., Larour, E., Ben Dhia, H., & Aubry, D. (2010). Spatial patterns of basal drag inferred using control methods from a full-Stokes and simpler models for Pine Island Glacier, West Antarctica. *Geophysical Research Letters*, *37*(14), n/a-n/a. https://doi.org/10.1029/2010GL043853

Morlighem, M., Rignot, E., Seroussi, H., Larour, E., Ben Dhia, H., & Aubry, D. (2011). A mass conservation approach for mapping glacier ice thickness. *Geophysical Research Letters*,

38(19), L19503. https://doi.org/10.1029/2011GL048659

Mouginot, J., Scheuchl, B., & Rignot, E. (2012). Mapping of Ice Motion in Antarctica Using Synthetic-Aperture Radar Data. *Remote Sensing*, *4*(9), 2753–2767. https://doi.org/10.3390/rs4092753

Mouginot, J., Rignot, E., & Scheuchl, B. (2014). Sustained increase in ice discharge from the Amundsen Sea Embayment, West Antarctica, from 1973 to 2013. *Geophysical Research Letters*, *41*(5), 1576–1584. https://doi.org/10.1002/2013GL059069

Ng, F., & Conway, H. (2004). Fast-flow signature in the stagnated Kamb Ice Stream, West Antarctica. *Geology*, *32*(6), 481–484. https://doi.org/10.1130/G20317.1

Paolo, F. S., Fricker, H. A., & Padman, L. (2015). Ice sheets. Volume loss from Antarctic ice shelves is accelerating. *Science (New York, N.Y.)*, *348*(6232), 327–31. https://doi.org/10.1126/science.aaa0940

Paolo, F. S., Padman, L., Fricker, H. A., Adusumilli, S., Howard, S., & Siegfried, M. R. (2018). Response of Pacific-sector Antarctic ice shelves to the El Niño/Southern Oscillation. *Nature Geoscience*, *11*(2), 121–126. https://doi.org/10.1038/s41561-017-0033-0

Parrenin, F., Dreyfus, G., Durand, G., Fujita, S., Gagliardini, O., Gillet, F., … Yoshida, N. (2007). 1-D-ice flow modelling at EPICA Dome C and Dome Fuji, East Antarctica. *Climate of the Past*, *3*(2), 243–259. https://doi.org/10.5194/cpd-3-19-2007

Pattyn, F., Perichon, L., Durand, G., Favier, L., Gagliardini, O., Hindmarsh, R. C. A., … Wilkens, N. (2013). Grounding-line migration in plan-view marine ice-sheet models: results of the ice2sea MISMIP3d intercomparison. *Journal of Glaciology*, *59*(215), 410–422. https://doi.org/10.3189/2013JoG12J129

Pollard, D., DeConto, R. M., & Alley, R. B. (2015). Potential Antarctic Ice Sheet retreat driven by hydrofracturing and ice cliff failure. *Earth and Planetary Science Letters*, *412*, 112–121. https://doi.org/10.1016/j.epsl.2014.12.035

Pollard, D., Chang, W., Haran, M., Applegate, P., & DeConto, R. (2016). Large ensemble modeling of the last deglacial retreat of the West Antarctic Ice Sheet: comparison of simple and advanced statistical techniques. *Geoscientific Model Development*, *9*(5), 1697–1723. https://doi.org/10.5194/gmd-9-1697-2016

Pollard, D., & DeConto, R. M. (2009). Modelling West Antarctic ice sheet growth and collapse through the past five million years. *Nature*, *458*(7236), 329–32. https://doi.org/10.1038/nature07809

Price, P. B., Nagornov, O. V., Bay, R., Chirkin, D., He, Y., Miocinovic, P., … Zagorodnov, V. (2002). Temperature profile for glacial ice at the South Pole: Implications for life in a nearby subglacial lake. *Proceedings of the National Academy of Sciences*, *99*(12), 7844–7847. https://doi.org/10.1073/pnas.082238999

Pritchard, H. D., Arthern, R. J., Vaughan, D. G., & Edwards, L. A. (2009). Extensive dynamic thinning on the margins of the Greenland and Antarctic ice sheets. *Nature*, *461*(7266), 971–975. https://doi.org/10.1038/nature08471

Pritchard, H. D., Ligtenberg, S. R. M., & Fricker, H. A. (2012). Antarctic ice-sheet loss driven by basal melting of ice shelves. *Nature*, *484*(7395), 502–505.

https://doi.org/10.1038/nature10968

Rahman, N. A., MacPherson, A. S., Rosemblatt, K. A., & Appelbaum, N. P. (1968). *A Course in Theoretical Statistics: For Sixth Forms* (2nd ed.). London: Charles Griffin & Company Limited.

Rasmussen, S. O., Abbott, P. M., Blunier, T., Bourne, A. J., Brook, E., Buchardt, S. L., … Winstrup, M. (2013). A first chronology for the North Greenland Eemian Ice Drilling (NEEM) ice core. *Climate of the Past*, *9*(6), 2713–2730. https://doi.org/10.5194/cp-9-2713-2013

Rignot, E. (1998). Fast recession of a west antarctic glacier. *Science (New York, N.Y.)*, *281*(5376), 549–51. https://doi.org/10.1126/science.281.5376.549

Rignot, E. (2008). Changes in West Antarctic ice stream dynamics observed with ALOS PALSAR data. *Geophysical Research Letters*, *35*(12), L12505. https://doi.org/10.1029/2008GL033365

Rignot, E., Mouginot, J., & Scheuchl, B. (2011). Ice flow of the Antarctic ice sheet. *Science (New York, N.Y.)*, *333*(6048), 1427–30. https://doi.org/10.1126/science.1208336

Rignot, E., Jacobs, S., Mouginot, J., & Scheuchl, B. (2013). Ice Shelf Melting Around Antarctica. *Science*, *341*(6143), 266–270. https://doi.org/10.1126/science.1235798

Rignot, E., Mouginot, J., Morlighem, M., Seroussi, H., & Scheuchl, B. (2014). Widespread, rapid grounding line retreat of Pine Island, Thwaites, Smith, and Kohler glaciers, West Antarctica, from 1992 to 2011. *Geophysical Research Letters*, *41*(10), 3502–3509. https://doi.org/10.1002/2014GL060140

Rintoul, S. R., Silvano, A., Pena-Molino, B., van Wijk, E., Rosenberg, M., Greenbaum, J. S., & Blankenship, D. D. (2016). Ocean heat drives rapid basal melt of the Totten Ice Shelf. *Science Advances*, *2*(12), e1601610–e1601610. https://doi.org/10.1126/sciadv.1601610

Robin, G. de Q., Doake, C. S. M., Kohnen, H., Crabtree, R. D., Jordan, S. R., & Möller, D. (1983). Regime of the Filchner–Ronne ice shelves, Antarctica. *Nature*, *302*(5909), 582–586. https://doi.org/10.1038/302582a0

De Rydt, J., Holland, P. R., Dutrieux, P., & Jenkins, A. (2014). Geometric and oceanographic controls on melting beneath Pine Island Glacier. *Journal of Geophysical Research: Oceans*, *119*(4), 2420–2438. https://doi.org/10.1002/2013JC009513

Sanderson, T. J. O. (1979). Equilibrium Profile of Ice Shelves. *Journal of Glaciology*, *22*(88), 435–460. https://doi.org/10.1017/S0022143000014453

Scherer, R. P., Aldahan, Tulaczyk, Possnert, Engelhardt, & Kamb. (1998). Pleistocene collapse of the west antarctic ice sheet. *Science (New York, N.Y.)*, *281*(5373), 82–5. https://doi.org/10.1126/science.281.5373.82

Scheuchl, B., Mouginot, J., Rignot, E., Morlighem, M., & Khazendar, A. (2016). Grounding line retreat of Pope, Smith, and Kohler Glaciers, West Antarctica, measured with Sentinel-1a radar interferometry data. *Geophysical Research Letters*, *43*(16), 8572–8579. https://doi.org/10.1002/2016GL069287

Schoof, C. (2005). The effect of cavitation on glacier sliding. *Proceedings of the Royal Society A: Mathematical, Physical and Engineering Sciences*, *461*(2055), 609–627.

https://doi.org/10.1098/rspa.2004.1350

Schoof, C. (2007). Ice sheet grounding line dynamics: Steady states, stability, and hysteresis. *Journal of Geophysical Research*, *112*(F3), F03S28. https://doi.org/10.1029/2006JF000664

Seroussi, H., Nakayama, Y., Larour, E., Menemenlis, D., Morlighem, M., Rignot, E., & Khazendar, A. (2017). Continued retreat of Thwaites Glacier, West Antarctica, controlled by bed topography and ocean circulation. *Geophysical Research Letters*, *44*(12), 6191–6199. https://doi.org/10.1002/2017GL072910

Seroussi, H., & Morlighem, M. (2018). Representation of basal melting at the grounding line in ice flow models. *The Cryosphere*, *12*(10), 3085–3096. https://doi.org/10.5194/tc-12-3085-2018

Severinghaus, J. P., & Battle, M. O. (2006). Fractionation of gases in polar ice during bubble close-off: New constraints from firn air Ne, Kr and Xe observations. *Earth and Planetary Science Letters*, *244*(1–2), 474–500. https://doi.org/10.1016/j.epsl.2006.01.032

Shean, D. (2016). Quantifying ice-shelf basal melt and ice-stream dynamics using high-resolution DEM and GPS time series.

Shean, D. E., Christianson, K., Larson, K. M., Ligtenberg, S. R. M., Joughin, I. R., Smith, B. E., … Holland, D. M. (2017). GPS-derived estimates of surface mass balance and ocean-induced basal melt for Pine Island Glacier ice shelf, Antarctica. *The Cryosphere*, *11*(6), 2655–2674. https://doi.org/10.5194/tc-11-2655-2017

Shean, D. E., Alexandrov, O., Moratto, Z. M., Smith, B. E., Joughin, I. R., Porter, C., & Morin, P. (2016). An automated, open-source pipeline for mass production of digital elevation models (DEMs) from very-high-resolution commercial stereo satellite imagery. *ISPRS Journal of Photogrammetry and Remote Sensing*, *116*, 101–117. https://doi.org/10.1016/j.isprsjprs.2016.03.012

Shepherd, A. P., Ivins, E. R., A, G., Barletta, V. R., Bentley, M. J., Bettadpur, S., … Zwally, H. J. (2012). A Reconciled Estimate of Ice-Sheet Mass Balance. *Science*, *338*(6111), 1183–1189. https://doi.org/10.1126/science.1228102

Shepherd, A., Wingham, D., & Rignot, E. (2004). Warm ocean is eroding West Antarctic Ice Sheet. *Geophysical Research Letters*, *31*(23). https://doi.org/10.1029/2004GL021106

Shepherd, A., Wingham, D., Wallis, D., Giles, K., Laxon, S., & Sundal, A. V. (2010). Recent loss of floating ice and the consequent sea level contribution. *Geophysical Research Letters*, *37*(13), n/a-n/a. https://doi.org/10.1029/2010GL042496

Shepherd, A., Ivins, E., Rignot, E., Smith, B., Van Den Broeke, M., Velicogna, I., … Wouters, B. (2018, June 13). Mass balance of the Antarctic Ice Sheet from 1992 to 2017. *Nature*. Nature Publishing Group. https://doi.org/10.1038/s41586-018-0179-y

Sigl, M., Fudge, T. J., Winstrup, M., Cole-Dai, J., Ferris, D., McConnell, J. R., … Sowers, T. A. (2016). The WAIS Divide deep ice core WD2014 chronology - Part 2: Annual-layer counting (0-31 ka BP). *Climate of the Past*, *12*(3), 769–786. https://doi.org/10.5194/cp-12-769-2016

Smith, J. A., Hillenbrand, C.-D., Kuhn, G., Klages, J. P., Graham, A. G. C., Larter, R. D., … Frederichs, T. (2014). New constraints on the timing of West Antarctic Ice Sheet retreat in the eastern Amundsen Sea since the Last Glacial Maximum. *Global and Planetary Change*,

122, 224–237. https://doi.org/10.1016/j.gloplacha.2014.07.015

Stanton, T. P., Shaw, W. J., Truffer, M., Corr, H. F. J., Peters, L. E., Riverman, K. L., … Anandakrishnan, S. (2013). Channelized Ice Melting in the Ocean Boundary Layer Beneath Pine Island Glacier, Antarctica. *Science*, *341*(6151). https://doi.org/10.1126/science.1239373

Sun, S., Cornford, S. L., Liu, Y., & Moore, J. C. (2014). Dynamic response of Antarctic ice shelves to bedrock uncertainty. *The Cryosphere*, *8*(4), 1561–1576. https://doi.org/10.5194/tc-8-1561-2014

Sun, S., Cornford, S. L., Gwyther, D. E., Gladstone, R. M., Galton-Fenzi, B. K., Zhao, L., & Moore, J. C. (2016). Impact of ocean forcing on the Aurora Basin in the 21st and 22nd centuries. *Annals of Glaciology*, *57*(73), 79–86. https://doi.org/10.1017/aog.2016.27

Thoma, M., Jenkins, A., Holland, D., & Jacobs, S. S. (2008). Modelling circumpolar deep water intrusions on the Amundsen Sea continental shelf, Antarctica. *Geophysical Research Letters*, *35*, L16802. https://doi.org/10.1029/2008GL034939

Thomas, R. H., & MacAyeal, D. R. (1982). Derived Characteristics of the Ross Ice Shelf, Antarctica. *Journal of Glaciology*, *28*(100), 397–412. https://doi.org/10.1017/S0022143000005025

Thyssen, F. (1988). Special Aspects of the Central Part of Filchner-Ronne Ice Shelf, Antarctica. *Annals of Glaciology*, *11*, 173–179. https://doi.org/10.1017/S0260305500006509

Tulaczyk, S., Kamb, W. B., & Engelhardt, H. F. (2000). Basal mechanics of Ice Stream B, west Antarctica: 1. Till mechanics. *Journal of Geophysical Research: Solid Earth*, *105*(B1), 463–481. https://doi.org/10.1029/1999JB900329

Veres, D., Bazin, L., Landais, A., Toyé Mahamadou Kele, H., Lemieux-Dudon, B., Parrenin, F., … Wolff, E. W. (2013). The Antarctic ice core chronology (AICC2012): An optimized multi-parameter and multi-site dating approach for the last 120 thousand years. *Climate of the Past*, *9*(4), 1733–1748. https://doi.org/10.5194/cp-9-1733-2013

Waddington, E. D., Neumann, T. A., Koutnik, M. R., Marshall, H.-P., & Morse, D. L. (2007). Inference of accumulation-rate patterns from deep layers in glaciers and ice sheets. *Journal of Glaciology*, *53*(183), 694–712. https://doi.org/10.3189/002214307784409351

Wåhlin, A. K., Kalén, O., Arneborg, L., Björk, G., Carvajal, G. K., Ha, H. K., … Stranne, C. (2013). Variability of Warm Deep Water Inflow in a Submarine Trough on the Amundsen Sea Shelf. *Journal of Physical Oceanography*, *43*(10), 2054–2070. https://doi.org/10.1175/JPO-D-12-0157.1

Walker, D. P., Brandon, M. A., Jenkins, A., Allen, J. T., Dowdeswell, J. A., & Evans, J. (2007). Oceanic heat transport onto the Amundsen Sea shelf through a submarine glacial trough. *Geophysical Research Letters*, *34*(2), L02602. https://doi.org/10.1029/2006GL028154

Weertman, J. (1957). On the Sliding of Glaciers. *Journal of Glaciology*, *3*(21), 33–38. https://doi.org/10.3189/S0022143000024709

Weertman, J. (1974). Stability of the junction of an ice sheet and an ice shelf. *Journal of Glaciology*, *13*(67), 3–11. https://doi.org/10.3198/1974JoG13-67-3-11

Van Wessem, J. M., Reijmer, C. H., Morlighem, M., Mouginot, J., Rignot, E., Medley, B., … Van

Meijgaard, E. (2014). Improved representation of East Antarctic surface mass balance in a regional atmospheric climate model. *Journal of Glaciology*, *60*(222), 761–770. https://doi.org/10.3189/2014JoG14J051

Wilhelms, F. (2005). Explaining the dielectric properties of firn as a density-and-conductivity mixed permittivity (DECOMP). *Geophysical Research Letters*, *32*(16), 1–4. https://doi.org/10.1029/2005GL022808

Wingham, D. J., Wallis, D. W., & Shepherd, A. (2009). Spatial and temporal evolution of Pine Island Glacier thinning, 1995–2006. *Geophysical Research Letters*, *36*(17), L17501. https://doi.org/10.1029/2009GL039126

Wu, X., & Jezek, K. C. (2004). Antarctic ice-sheet balance velocities from merged point and vector data. *Journal of Glaciology*, *50*(169), 219–230. https://doi.org/10.3189/172756504781830042

Zwinger, T., Greve, R., Gagliardini, O., Shiraiwa, T., & Lyly, M. (2007). A full Stokes-flow thermo-mechanical model for firn and ice applied to the Gorshkov crater glacier, Kamchatka. *Annals of Glaciology*, *45*(1), 29–37. https://doi.org/10.3189/172756407782282543

Appendix A. Supplementary materials to Chapter 2

A.1 Evidence against marine ice accretion on Dotson

Significant marine ice accretion downstream of the transverse portion of the channel on Dotson should cause a discrepancy between measurements of freeboard and ice thickness. Ice penetrating radar generally does not penetrate into saline marine ice (Crabtree & Doake, 1986; Robin et al., 1983; Thyssen, 1988), so the bottom reflector from the MCoRDS radar comes from the fresh/saline transition in areas with accreted ice. The radar measurement thus indicates the thickness of fresh ice only, while the freeboard is determined by the total ice thickness, including marine ice. In areas of marine ice, the difference between the full thickness and the fresh ice thickness should cause the actual freeboard to be greater than that which would be calculated from the thickness of the fresh ice alone.

To determine whether there is marine ice accretion on Dotson, we calculate an expected freeboard from ice-thickness measurements made by the MCorDS radar and compare this expected freeboard to surface elevations measured simultaneously by the ATM. To calculate freeboard from the MCorDS radar product, two firn corrections must be made: (1) radar waves propagate at different speeds in ice and firn, which is not accounted for in the estimates of thickness from the MCorDS radar and (2) the total thickness of the shelf includes the air in the firn, so the freeboard is greater would be expected if the full column were the density of ice. To correct for the propagation speed difference, we calculate the 2-way travel from the MCorDS thickness, then convert that value back to depth using a propagation speed that accounts for firn-air content. We calculate a floatation height from this thickness by assuming the column is pure ice, then add to that the thickness of the air column to obtain the final estimate for expected freeboard. For both of these calculations, we

assume a constant firn-air content of 13 m. This value is near the median of the spatially variable values we calculate in the main text, and using a spatially constant value prevents aliasing marine ice as variations in firn-air content. We compare surface elevations calculated using hydrostatic equilibrium to the surface elevations from the ATM, which we reference to the EGM2008 geoid and interpolate onto the MCoRDS data using the 5 nearest points, slope correcting and weighting by inverse square distance.

Along flight lines approximately parallel to flow, we find that the freeboard height calculated from ice thickness corresponds to measured surface elevation with standard deviations ranging from 2.9-4.3 m. The channel has a surface expression of 10 m over large portions of these flightlines and up to 15 m in places, so the channel is deep compared to the errors in our method. We the calculated freeboard to have 3-4 m bias towards a higher surface than the direct freeboard measurements, opposite of what is expected if marine ice is present. Further, we find no correlation between distance along flow and misfit between observed and measured ice thickness. If marine ice accreted downstream of this channel, we would expect a trend towards the hydrostatic calculation of freeboard being smaller than the freeboard measured with the ATM farther downstream. Thus, we conclude that the thickening downstream of the channel on Dotson is not caused by marine ice accretion, but rather by dynamic thinning or a temporal change in melt.

A.2 Calculation of melt rates following Khazendar et al. (2016)

We converted the thinning rates in Khazendar et al. (2016), which represent anomalous thinning under the assumption of no dynamic thinning, to melt rates using the flux divergence. As in Khazendar et al., we first calculated the thinning rate at each crossover of the MCorDS radar over Crosson and Dotson, and our values for the thinning rate agree to within error for the 27 points that they do not identify as anomalous (Table S2). To obtain the flux divergence correction, we

resampled velocity and ice thickness to a 1000-m grid and calculated the flux divergence at each grid point. We then linearly interpolated the flux divergence from the grid to each radar crossover and subtracted this value from the thinning rate to obtain the melt rate. We plot the melt rate in Figure A-1 and present the values inTable A-1. The peak value we find (187 m a^{-1}) is greater than the peak thinning rate found in Khazendar et al. (2016), though the magnitude of melt that we find is generally comparable to the thinning rates in the area. The distribution of melt is different than the distribution of thinning found in Khazendar et al. (2016), but as expected melt is highest near the grounding line and decreases downstream. These recalculated values are still sensitive to advection of heterogeneous properties of the shelf (e.g. crevasses or parcels of thick ice) that are not accounted for in the flux divergence, and thus may not be representative of melt.

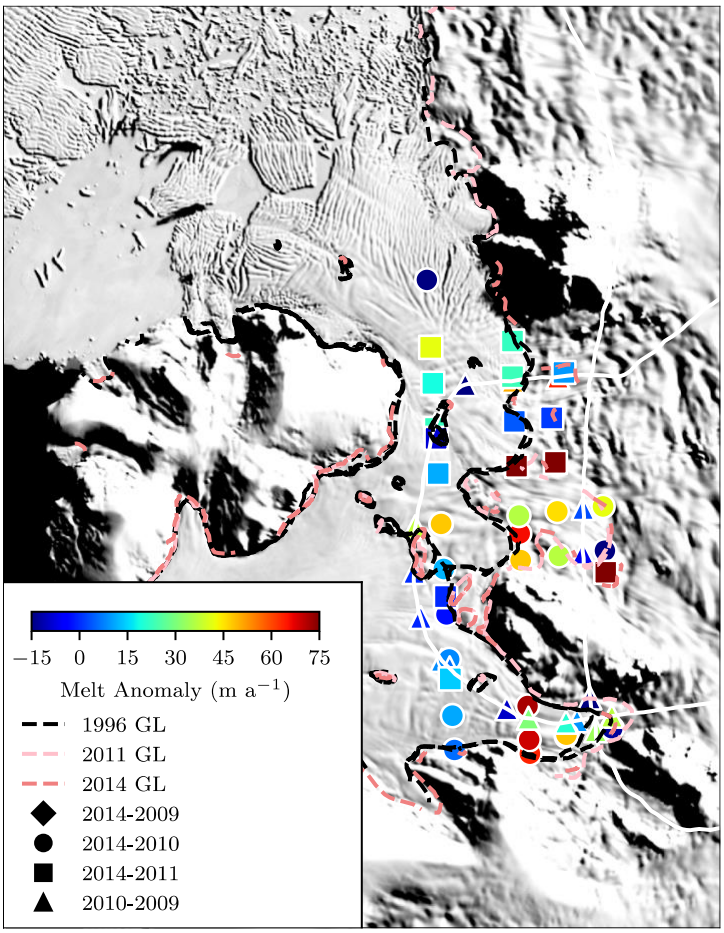

Figure A-1. Melt rate anomalies.

Calculated using the thinning rate and flux divergence, at crossover points of Operation Icebridge flightlines 2009-2014. Color indicates melt rate, and shape of the symbol indicates the years of crossover. Dashed lines show grounding lines, and the solid white line indicates the flightpath repeated in 2002 and 2009. See Khazendar et al. (2016).

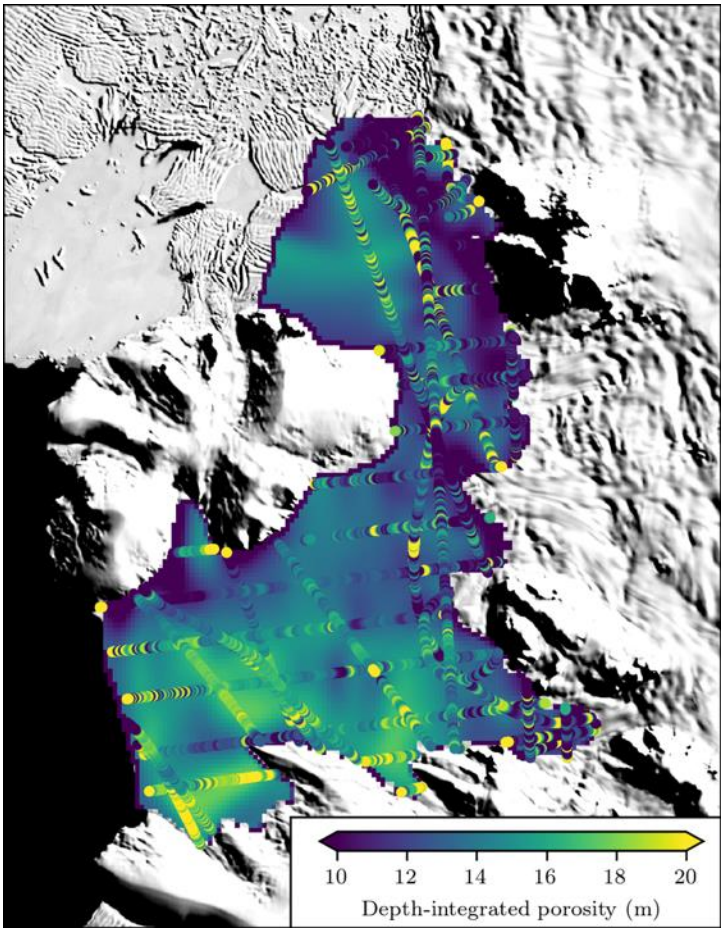

Figure A-2. Depth-integrated porosity (firn-air content) over Crosson and Dotson ice shelves.

Colors in the background show gridded product, colored circles show individual radar traces from the MCoRDS radar.

Point Number	$\partial H/\partial t$(m a^{-1})	$\partial H/\partial t$ (m a^{-1}) from (Khazendar et al., 2016)	Anomalous melt rate (m a^{-1})
1	-2	-3	23
2	-10	-10	10
3	49	38	63
4	27	30	50
5	2	5	1
6	51	44	106
7	139	129	127
8	24	16	42
9	20	14	46
10	0	-2	36
11	43	37	66
12	59	51	48
13	36	18	37
14	66	57	-30
15	41	44	3
16	59	65	-7
17	88	83	187
18	37	32	72
19	22	13	69
20	35	33	64
21	21	19	48
22	15	15	37
23	-13	-20	-13
24	-15	109	34
25	-18	-9	10
26	22	19	37
27	10	13	21
28	18	19	30

Table A-1. Comparison of values for thinning and melt rate.

We retain the numbering of points used in that Khazendar et al. (2016)'s supplementary material. Columns 2 and 3 show the thickness changes estimated here and that paper respectively. Column 4 shows the melt rate, calculated by subtracting the flux divergence from the thinning rate. Note that Khazendar et al. identify point 24 as anomalous, though the value we calculate is similar to others in the area.

Appendix B. Supplementary materials to Chapter 3

B.1 Model initialization

The modeled ice temperature depends on the inferred basal shear stress and ice viscosity because of their effect on strain heating within the ice and frictional heating at the bed, and the inferred velocity field depends on the temperature because the rheology of ice depends on its temperature. This coupling thus necessitates recursive updating of the estimates of these fields to reach a consistent solution that matches the observed velocity.

B.1.1 Diagnostic temperature model

Since vertical variations in temperature are generally larger than horizontal variations, for both shallow-shelf and full-Stokes models it is necessary to determine the temperature in three dimensions. Thus, to initialize both shallow-shelf and full-Stokes models, we used a full-Stokes diagnostic model to determine the temperature. The model solves the advection-diffusion equations for heat within the ice, accounting for heat production from internal deformation and from basal friction (Zwinger et al., 2007). The upper surface was fixed to the 1979-2013 mean temperature from RACMO 2.3 (Van Wessem et al., 2014), and the upstream boundaries used a simple ice-divide temperature profile (Cuffey & Paterson, 2010). Over grounded ice, we imposed an incoming flux equal to the geothermal heat on the lower surface (Maule et al., 2005), while over floating ice we assumed that the temperature was equal to the pressure melting point. After finding the temperature field, we extracted the depth-averaged temperature and flow coefficient (B) for use with the shallow-shelf model and used the inferred temperature field directly with the full-Stokes model.

B.1.2 Inversion procedure

We separately determined the basal shear stress beneath grounded ice and the depth-averaged enhancement factor over floating ice that minimized the misfit between modelled velocity and InSAR observations from 1996. Leaving a single free parameter in each area of the domain prevented overfitting. For both inversion procedures, adjoint methods were used to determine the parameter values that caused the best fit with observations (MacAyeal, 1993; Morlighem et al., 2010). We did not regularize the enhancement factor inversions, while for the basal shear stress we used an L-curve (Calvetti et al., 2000) to select the regularization coefficient. Though the methods were identical, this procedure was performed separately for shallow-shelf and full-Stokes models because the basal shear stress in particular is fundamentally different between the two models; because all motion is accommodated by sliding in the shallow-shelf model, basal resistance must generally be inferred to be lower in order to allow flow to be as fast as observations. The friction coefficient corresponding to the Schoof (2005) sliding law was computed from the basal shear stress and basal velocity fields, and then the friction coefficient and depth-averaged enhancement factor were used as inputs for the iterative determination of the temperature field and subsequently for initialization of the forward model.

B.1.3 Relaxation

In order to prevent spurious, transient effects caused by erroneous data from affecting our analysis, we allowed the model geometry to evolve for one year, using the full-Stokes model, then used the resulting geometry to re-determine the temperature and inferred parameters. In the context of ongoing changes, relaxation is necessarily a compromise between trying to capture real transient effects and removing artificial effects resulting from data or model errors. For example, because sub-shelf melt exceeded grounding-line flux which in turn exceeded basin-wide accumulation, any

melt forcing will necessarily be out of balance with either grounded- or floating-ice loss. During the relaxation, the model was forced using an estimate of the melt in 1996 (Lilien, Joughin, et al., 2018), leading to slight mass loss during the relaxation process. Once the new geometry was obtained, we again iterated between temperature modelling and inverse modelling (with both the full-Stokes and shallow-Shelf models) to best match the velocities in 1996. These final inferred values, as described above, were then used as the initial conditions for the longer prognostic simulations.

B.2 Model limitations

Here we show that the central modeling results are not limited by the mesh resolution or the sliding law.

B.2.1 Model resolution

We ran simulations using both the full-Stokes and shallow-shelf models at three resolutions to determine whether the meshes used were sufficiently fine to accurately capture grounding-line dynamics. We used 300 m, 500 m, and 1000 m horizontal grounding-line resolution, with resolution away from the grounding line ten times coarser in all cases. These meshes had 3, 7, and 9 vertical layers, respectively, for the full-Stokes runs. The evolution of the grounding line for each of these resolutions is shown in Figure B-1. We find that the mesh resolution affects the timing of retreat, the change is only ~10 years for the shallow shelf model and ~5 years for the full-Stokes model. However, whether retreat occurs, and the rate at which it occurs once initiated, is similar regardless of mesh resolution. In light of this similarity, and past studies that have indicated that 300 m is sufficient resolution near the grounding line (Pattyn et al., 2013; Hélène Seroussi & Morlighem, 2018; Sun et al., 2016), we consider the 300 m runs sufficiently resolved for meaningful interpretation.

B.2.2 Sliding law

All the simulations discussed in the main text were conducted using a Coulomb-type sliding law (O. Gagliardini et al., 2007; C. Schoof, 2005). For comparison, we ran set of four simulations using the shallow-shelf model, each with different melt forcing at 1Obs intensity, using a Weertman sliding law with $m = 3$. The rate of grounding line retreat is relatively insensitive to using this other sliding law, though some differences in timing are observed (Figure B-2). We do not further interpret the differences between these runs, but simply note that our primary conclusions about what forcings result in grounding-line retreat are not sensitive to the choice between these commonly used sliding laws. However, we consider the coulomb-type sliding law to be the best choice for such simulations given present knowledge about the sliding process; multiple studies have found nearly plastic behavior underneath fast-moving ice and Weertman sliding with smaller exponents in slower moving regions (Gillet-Chaulet et al., 2016; I. R. Joughin et al., 2009).

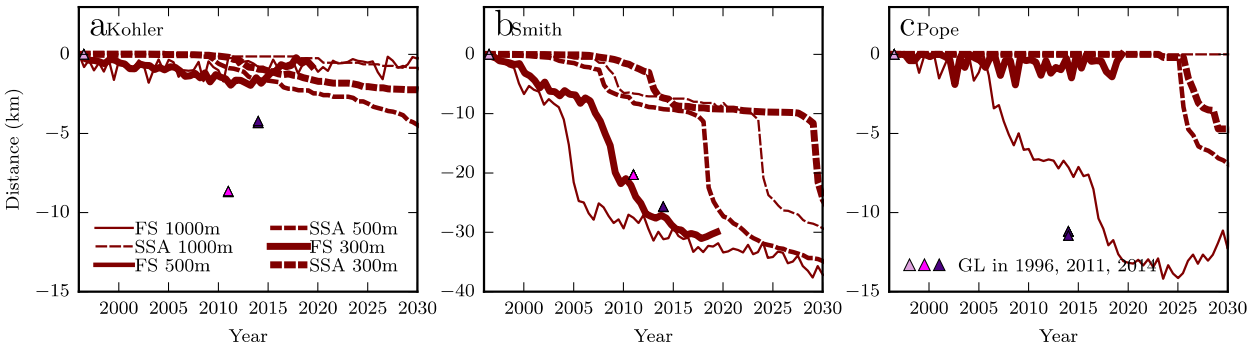

Figure B-1. Sensitivity of grounding line position to mesh resolution.

a-c. Position of grounding line through time along transects of Kohler, Smith, and Pope centerlines, respectively, from Figure 3-1. Line style indicates model physics: solid for full Stokes and dashed for shallow shelf. Line thickness indicates mesh resolution near the grounding line, with thicker lines indicating higher resolution. Purple triangles indicate observed grounding-line positions through time.

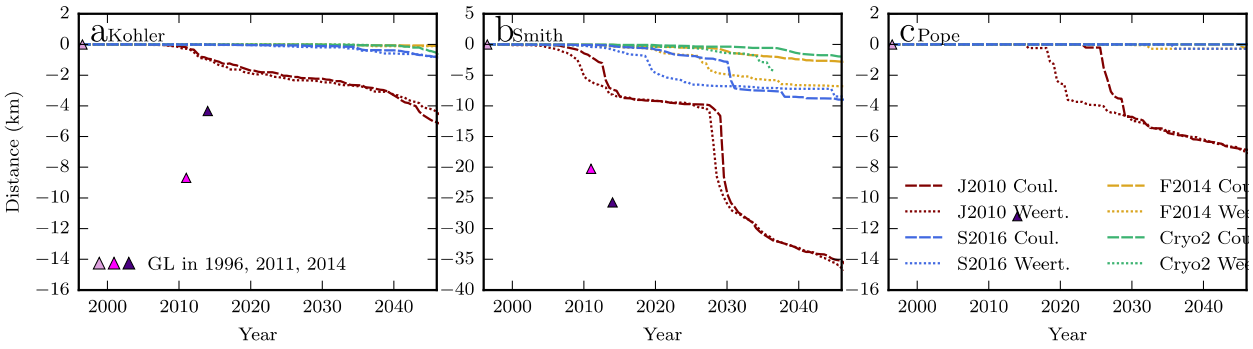

Figure B-2. Sensitivity of grounding-line position to sliding law.

a-c. Position of grounding line through time along transects of Kohler, Smith, and Pope centerlines, respectively, from Figure 3-1. Line style indicates sliding law, with the Schoof (2005) sliding law that was used in the main text as the dashed lines and a Weertman sliding law with exponent $m = 3$ as the dotted line. Color indicates melt forcing used. Purple triangles indicate observed grounding-line positions through time.

Appendix C. Supplementary material to Chapter 4

C.1 Flowline determination.

The ice-flow velocity field was determined using GPS methods because satellite measurements are not accurate near South Pole. We conducted a GPS survey in the region upstream of South Pole over the course of three field seasons. The survey extended along lines of longitude at 10° intervals from 110° to 180°E with stakes placed at 0.112° (~12.5 km) latitudinal intervals; the network consisted of 56 stakes (Figure 4-1). Stakes were placed and surveyed, then resurveyed 1-2 years later. Horizontal velocities were calculated from the offsets between occupations. Velocities range from 3 to 10 m/yr, with errors of ±2 to 25 cm/yr in each horizontal direction (generally ~1% of the velocity).

The measured velocity field was used to determine the modern flowline. Starting at the SPICEcore drill site, we recursively stepped upstream by one-year intervals in the direction opposite the velocity vectors to obtain yearly positions along the flowline. To find the velocity at each step, we used a piecewise-linear interpolation of the GPS point-stake measurements on a Delaunay triangularization of the data. Uncertainty in the flowline was determined using a Monte-Carlo method with 10,000 realizations of the horizontal components of each velocity measurement varied independently and randomly within their uncertainty distributions. This propagation of uncertainty ignores errors in the interpolation method, though a piecewise-cubic interpolation does not change the flowline outside the 95% confidence interval of the linear interpolation.

C.2 Radar Processing

Radar data were collected using a GSSI SIR-4000 controller and a 200 MHz antenna. The antenna was on a sled ~5 m behind a snow machine, and the location of the radar was determined using a Garmin 18x GPS receiver attached to the hood of the snow machine. A full profile approximately following the GPS-determined flowline for 100 km upstream of South Pole was concatenated from 10-15km segments. The radar profile started 1 km upstream of the SPICEcore drill site and differed from the GPS-determined flowline by more than 1 km at points during the first ~12.5 km where the South Pole Station and associated restricted-use zones limited travel. Several profiles perpendicular to the flowline were also acquired; 10 km profiles were acquired at 12.5, 25 and 100 km and a 30 km profile was acquired at 50 km. Individual radar waveforms were stacked, using 50 traces horizontally, and then filtered horizontally using a Butterworth bandpass filter that passed wavelengths of 10-100 traces; the horizontal bandpass was necessary to remove spurious low-frequency changes in depth-integrated power return. A Butterworth bandpass filter with cutoff wavelengths of approximately 0.13 and 0.31 m was applied in the vertical direction. Layers were traced semi-automatically using the GSSI Radan software; points along layers were picked manually every ~20 traces, and the software uses a maximum-amplitude algorithm to interpolate between picks. Finally, the measured two-way travel time through the firn was converted to depth using the density-dependent relative dielectric permittivity (Wilhelms, 2005).

We use a closed loop traced in the radar data to assess how accurately we are able to continue tracing the same layer over long distances. The loop is comprised of two transects at 12.5 and 25 km from South Pole, connected by a profile at their eastern margin. Tracing of the cross profiles comprising the loop began at the intersection 25 km from South Pole, and layer depths were matched at that location. At the point 12.5 km from South Pole, the loop had become biased

by 25 cm compared to the flowline transect, or 1% over the 35 km comprising the loop. We thus estimate the total potential bias in the inferred accumulation rate caused by erroneously switching the layers we traced to be 2% over the 60 km analyzed in our work.

C.3 Determining the layer most representative of modern accumulation

Inferring the average modern accumulation rate from shallow radar layers requires finding a layer that is sufficiently shallow so it has not been influenced significantly by flow, but sufficiently deep so that real variations in layer depth can be separated from the noise. The absolute error in picking the depth of a layer is approximately constant (±3 to 5 pixels or cm) and thus the relative picking error is highest for the shallowest layers. However, deeper layers have been advected a greater distance and thus record cumulative strain as well as a spatially integrated measure of accumulation. Following Waddington et al. (2007), we examine the influence of horizontal advection on radar layers using a dimensionless criterion, D:

$$\mathrm{D} = \bar{\mathrm{u}} \times \mathcal{A} \times \left(\left| \frac{1}{\dot{\mathrm{b}}} \frac{\mathrm{d}\dot{\mathrm{b}}}{\mathrm{dx}} \right| + \left| \frac{1}{\mathrm{H}} \frac{\mathrm{dH}}{\mathrm{dx}} \right| \right) \quad (1)$$

where $\bar{\mathrm{u}}$ is the average horizontal velocity along the flowline in the x-direction, $\mathcal{A}$ is the age of a layer, $\dot{\mathrm{b}}$ is the accumulation rate and H the ice-sheet thickness.

When $\mathrm{D} \ll 1$, layers have not been significantly affected by flow. Near South Pole, $\bar{\mathrm{u}} \approx 6 - 10\ \mathrm{m}\ a^{-1}$. For all layers we traced, the largest variations are 20-25% over scales of 3 km, so $\left| \frac{1}{\dot{\mathrm{b}}} \frac{\mathrm{d}\dot{\mathrm{b}}}{\mathrm{dx}} \right| \approx 0.25 \frac{1}{(3000\ \mathrm{m})} = 8.0 \times 10^{-5} \mathrm{m}^{-1}$. Using ice thickness and bed topography variations

detected from our 7 MHz radar, $\left|\frac{1}{H}\frac{dH}{dx}\right| \approx \frac{100\text{ m}}{(1000\text{ m})\times(2700\text{ m})} \approx 3.7\times10^{-5}\text{ m}^{-1}$. Figure C-4 shows D vs. age for different flow speeds. Near South Pole, $D \ll 1$ (taken to mean <0.25) for layers shallower than 31 m (~200 years old) while layers deeper than 80 m (~750 years old) have been significantly affected by flow. Here we focus on a layer at 23 m depth (150 years old).

C.4 Spatial variations in firn density

Determination of the spatial variability in accumulation requires an assumption about spatial variations in density. We assume a horizontally constant density profile, matching that measured in the USP50 firn core; however, this assumption is likely imperfect due to the variations in accumulation we infer along the flowline. Variations in density affect both the conversion to ice-equivalent thickness and the propagation speed of the radar wave (Wilhelms, 2005). These errors have opposite sign. For example, radar waves travel faster through a layer of low density snow, so the inferred thickness is greater. On the other hand, the ice-equivalent thickness of a low-density layer is smaller. These two effects do not entirely cancel because the effect on ice-equivalent thickness dominates. The relatively small changes in accumulation, uncertain variability in surface density, and importance of advection, limit the usefulness of firn models to address this problem. Instead, we treat the variable firn density as a source of error, and we estimate this error using variations in density measured in cores extracted near South Pole (pers. comm. from Murat Aydin and Christo Buizert; Severinghaus & Battle, 2006). The spread in accumulation caused by this range of firn densities has a standard deviation of 2.3%, and the USP50 depth-density profile is in the middle of this range. Variations within the range of densities captured by the available measurements thus would cause variations in the inferred accumulation that are small (~10%)

compared to the actual variation observed. Even if the regional variability of density may be slightly larger, the relatively small influence of the observed variability suggests that density variations are not a significant source of error in the inferred accumulation pattern.

C.5 Autocorrelation length scales

Both the radar layer used to infer accumulation and the SPICEcore-derived accumulation history have significant autocorrelation due to persistence in the spatial (and, in the case of SPICEcore, temporal) processes controlling the accumulation. This autocorrelation causes nearby measurements not to be truly independent. For example, the accumulation along one radar trace is well-predicted by a neighboring trace. Thus, the number of effective degrees of freedom in each dataset, N^*, is smaller than the number of measurements (i.e. radar traces or dated intervals in SPICEcore). In order to determine the decorrelation length scale and what correlations with the SPICEcore-derived accumulation record are significant, an estimate of N^* is required.

We use the estimate that $N^* = \frac{L_T}{2L_D}$ where L_T is the total length of the dataset and L_D is the decorrelation length at 1-σ confidence, i.e. the distance at which the autocorrelation becomes less than $\frac{1}{\sqrt{N^*}}$. L_D is doubled in this formula because it represents a radius of correlation while the number of degrees of freedom are effectively determined by a diameter of correlation (e.g. Leith, 1973). Most methods for direct estimation of L_D require assumptions about underlying distributions that are inapplicable here, so instead we take a boot-strapping approach. Because of the circular dependence between N^* and the autocorrelation, we recursively calculated the 1-σ decorrelation length, and updated L_D to re-estimate N^* until this process converged on a consistent value of N^*.

After calculating N^* for the radar along the flowline and along the 30 km transect at 50 km, we calculated the lag distance at which the autocorrelation becomes insignificant at 95% confidence (i.e. becomes less than $\frac{1.96}{\sqrt{N^*}}$). This process yields a 0.9 km across-flow radius and a 1.8 km along-flow radius. Thus, accumulation anomalies at points spaced by more than these radii are uncorrelated.

The significance of a correlation between the accumulation histories (at 95% confidence) was determined using a student's t-test to find whether the correlation was significantly different than zero. The test used the effective number of degrees of freedom in the SPICEcore record, N*≈11, rather than the number of intervals being correlated. Since $r^2 \geq 0$, we used a one-sided t-test with nine degrees of freedom to determine the t-value corresponding to 95% confidence; the reduced degrees of freedom accounts for the slope and offset determined by the correlation. We converted the resulting t-value to an r^2 value using $r^2 = \frac{t^2}{N^*-2+t^2}$, (e.g. Rahman et al., 1968) to determine that the correlation is significantly different from zero when $r^2 > 0.32$. Combining this result with the correlation between accumulation histories at different amounts of speedup, we find that speedups of 3—33% result in correlations that are significantly different from zero at 95% confidence.

C.6 Correlation calculation methods

In the main text, we present the correlation values assuming that each interval between age matches is given equal weight, although the same analysis could be performed with intervals weighted by their duration. Short intervals, particularly those less than 10 years long, may be dominated by processes (such as annual variations in accumulation or small-scale surface topography like

sastrugi) which cannot be captured in this type of analysis. We recognize that a number of other ways of weighting the intervals in the correlation may be justified, so we test the sensitivity to four different methods of computing the correlation:

1. Equal: All intervals are included and weighted equally regardless of duration.
2. Annual interpolation: We resample the interval accumulation rates at annual timesteps, effectively weighting the intervals by their durations.
3. Exclude intervals shorter than 100 years: We exclude intervals shorter than 100 years from the correlation for two reasons. First, the radar-derived accumulation-rate history is determined with an approximately 100-year old layer, so higher frequency variability is inherently excluded from that record. Second, we expect accumulation to vary on multi-decadal timescales, potentially dominating variability on timescales less than 100 years.
4. Remove age matches: We remove some age matches so that all intervals used in the correlation are longer than 100 years. This is similar to the second method, but rather than exclude the short intervals we append them to the next oldest interval and recalculate the accumulation rate over this new (>100 year) interval. This method provides the benefits of method 3 while ensuring that information from the entire 1.3 ka to 10.1 ka is included.

Figure C-3 shows the variance explained by each method for the different linear trends in Holocene speed. All four methods show similar trends with speedup and result in similar maximum correlation between the radar- and SPICEcore-derived accumulation-rate histories. The two methods using only intervals longer than 100 years both explain a greater amount of variance. This is not surprising as a few of the short duration intervals (Figure 4-4) can be seen to vary significantly from the surrounding intervals. This occurs because accumulation can vary greatly on annual and decadal timescales and this variability cannot be captured from the spatial pattern. The annual method explains less variance (3% less) at the 15% speedup. The differences among the methods highlight that the precise correlation is sensitive to the weighting method, but the overall pattern is not. Thus, our conclusions are unaffected by the choice of weighting method.

While the method of weighting the sampled intervals is one potential source of bias in the correlation between accumulation-rate histories, the discrete sampling of the SPICEcore-derived

accumulation-rate is another. We performed a variety of tests to determine the impact of this discrete sampling on the ability of our methods to recover the true correlation between the two histories of accumulation rate. For these tests, we took the radar-derived accumulation-rate history (because unlike the SPICEcore history it is continuous) and added either red noise or a sinusoidal function to it. We then generated the 44 randomly-timed age matches to match the number of age matches in the analyzed portion of SPICEcore. The accumulation rates between the age matches were found for both accumulation histories. The correlations were then compared to the correlations of the original (continuous) histories. In total, we generated 1000 red noise and 1000 sinusoid time series (the pairs of histories had correlations ranging from 0.65 and 0.9) and then sampled each with 1000 variations of age matches. We found that discrete sampling has little overall impact, causing only a slight under-prediction of the true correlation (<0.01) with a standard deviation of 0.03.

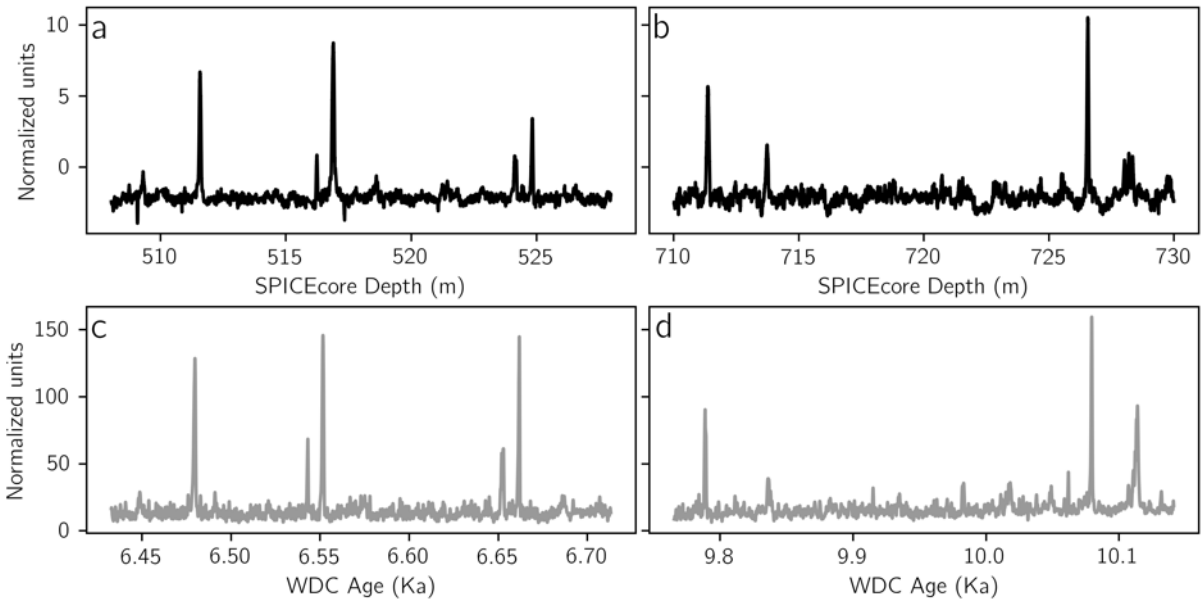

Figure C-1. Example electrical conductivity measurement (ECM) matches.

Matches are between SPICEcore (a and b) and the WAIS Divide core (WDC; c and d). The known age scale for WDC was used to date the conductivity peaks found in SPICEcore, as between panels a and c or between b and d.

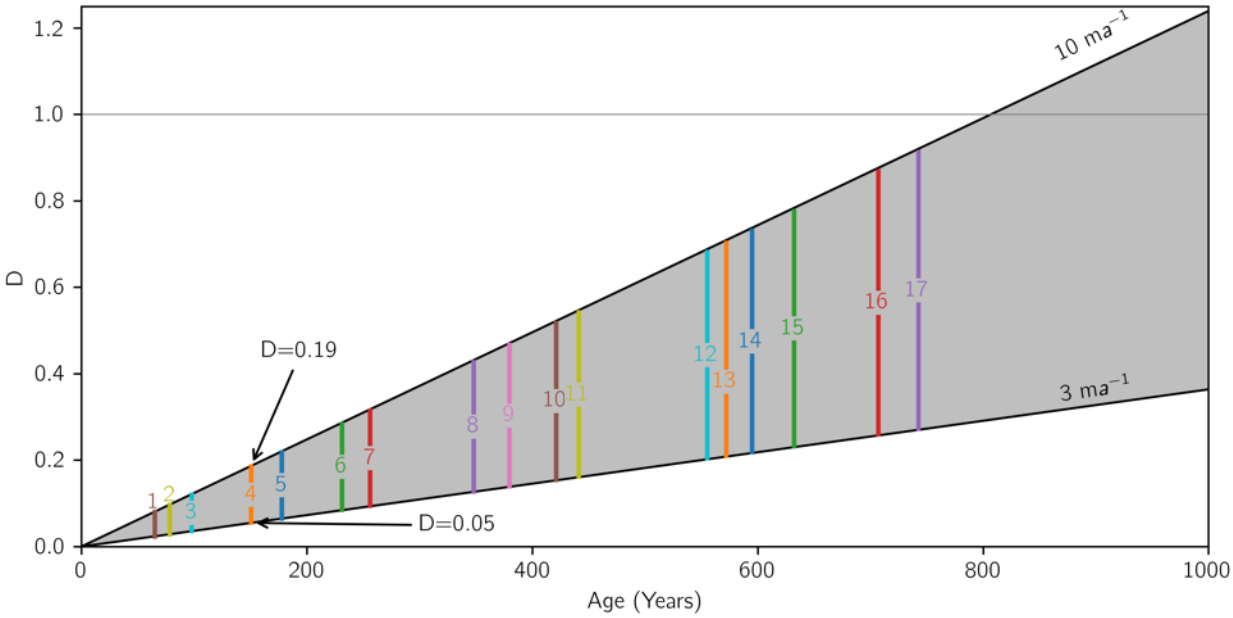

Figure C-2. D vs Age for shallow radar layers.

Gray region shows possible values of D given flow speeds upstream of South Pole. Colored lines indicate the ranges of D for different layers we traced, with colors and numbers matching Figure 4-2. Each layer was traced across ice with a range of speeds, thus yielding the range of values for D. The ~150-year-old layer (layer 4) used in our analysis has not been affected significantly by flow (at maximum observed velocity, D=0.19), but the deepest layer traced (layer 17, ~740 years old, D up to 0.91) has probably been affected by horizontal advection.

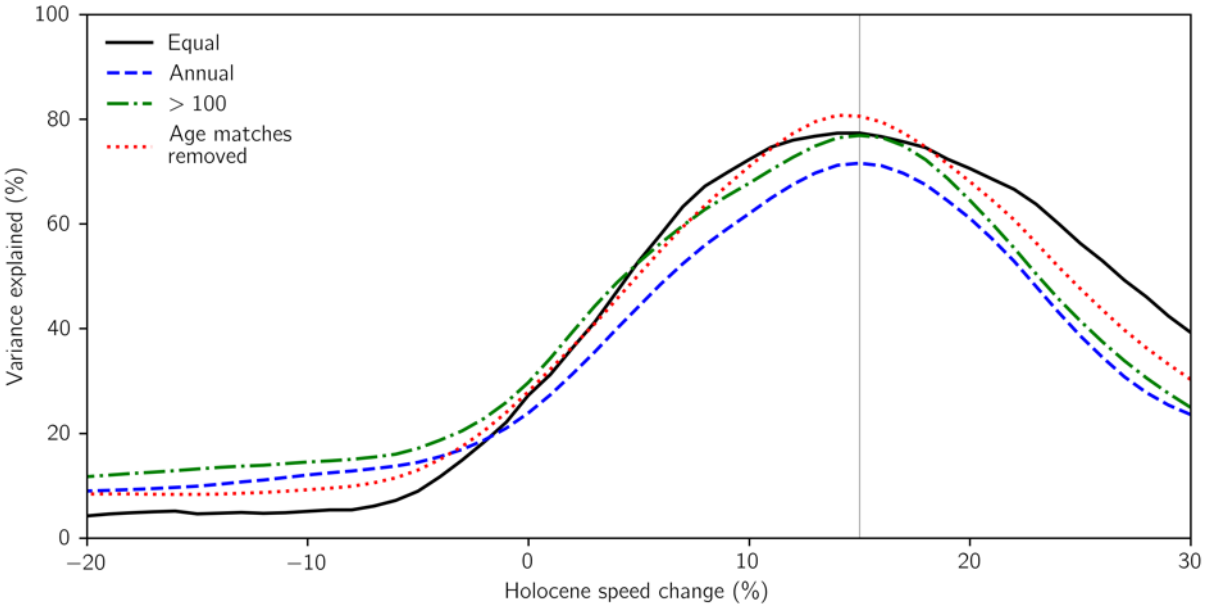

Figure C-3. Variance explained vs. speed change for different interval weightings.

The solid, black line represents equal weighting of each interval regardless of duration, as used in the main text and Figure 4-4d. The blue dashed line uses intervals weighted by their duration. The green dash-dot line indicates variation explained with intervals shorter than 100 years excluded. The red dotted line indicates variation explained with some age matches removed so that all intervals shorter than 100 years appended to other intervals, making all intervals at least 100 years long and not excluding any data. The vertical, gray line indicates the speed change resulting in maximum correlation with intervals weighted equally.

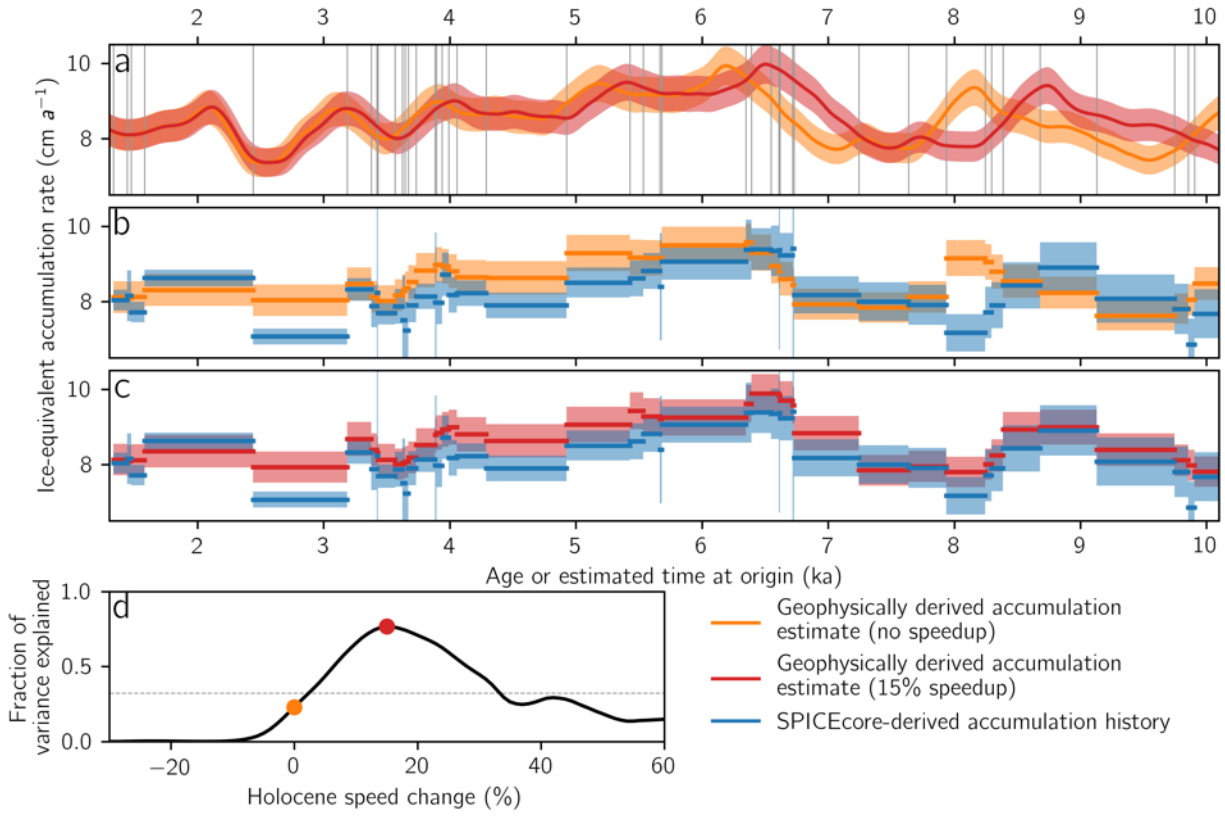

Figure C-4. Correlation 95% confidence envelopes.

Correlation between accumulation records, as in Figure 4-4. **a.** Geophysically derived accumulation rate as a function of travel time using modern velocities (orange) and applying the linear 15% increase in speed through the Holocene (i.e. with speeds 15% slower than modern at 10.1 ka) that maximizes correlation (red). Uncertainty envelopes include uncertainty in firn density (~2%), layer age (~2 years), and radar wavespeed (estimated to be 1% on top of the uncertainty in speed caused by variable density). Vertical lines show ages when SPICEcore is dated. **b.** Geophysically derived accumulation estimate without speedup (orange) and SPICEcore-derived accumulation history (blue). Thick lines show intervals between two dated layers in the core (the effective resolution); thin lines linearly connect these intervals for visual continuity). The uncertainty envelope for the SPICEcore derived history incorporates uncertainty in ECM peak location (1 year), uncertainty in the WAIS divide timescale to which the ECM measurements are matched (1 year/century), and uncertainty in the thinning function (0-~1% growing with depth). For the thinning function, uncertainty largely stems from the effects of poorly constrained kink height in the Dansgaard-Johnsen (1969) model; we use similar models with kink heights of 0% or 40% of the ice-sheet thickness in order to bound the reasonable range of thinning profiles. **c.** Same

as (b), but the geophysically derived estimate incorporates a 15% speedup (red). **d.** Correlation coefficient between the accumulation estimates for different linear trends in Holocene speed. Positive speed change indicates speedup since 10.1 ka and negative change indicates slowdown since 10.1 ka. Dashed gray line indicates 95% confidence that the records are correlated. Dots show the correlations between the pairs of curves in b and c, respectively.

USP50 Depth (m)	Age (years before 1950 on WD2014)	Depth of volcanic event in SPICEcore (m)
22.15	65	23.410
25.06	86	
30.75	133	33.175
31.56	140	33.949
49.89	307	53.685
68.18	490	72.526
79.04	604	83.560
84.44	663	89.293
85.22	673	90.226
85.92	680	90.861
86.83	691	91.862
89.48	719	94.595
94.40	778	99.708
99.66		105.13
105.47		110.98
106.30		111.81

Table C-1. ECM Matches.

Matches are between ECM depths in USP50 and depth in SPICEcore or age in WAIS Divide ice core.